Title	Long-term evolution of a subduction zone volcano : Geology, petrology, and geochemistry of Rishiri Volcano, southern Kuril Arc
Author(s)	,
Citation	. ( ) 14364
Issue Date	2021-03-25
DOI	10.14943/doctoral.k14364
Doc URL	http://hdl.handle.net/2115/82852
Type	theses (doctoral)
File Information	Hajime_Taniuchi.pdf

Instructions for use

Ph.D. thesis

博士学位論文

Long-term evolution of a subduction zone volcano:

Geology, petrology, and geochemistry of Rishiri Volcano,

southern Kuril Arc

沈み込み帯火山の長期進化過程：

千島弧南部，利尻火山の地質学・岩石学・地球化学

Hajime Taniuchi

谷内　元

Department of Natural History Science,

Graduate School of Science, Hokkaido University

北海道大学大学院　理学院　自然史科学専攻

March, 2021

Abstract

Subduction zone is one of the most active areas of magmatism on the Earth, and many geophysical and petrological studies have been carried out. However, the debates on the long-term evolutionary processes and their controlling factors of subduction zone volcanoes have not been put to rest. In this study, I carried out geological, geochronological, petrological, and geochemical studies at the Rishiri Volcano, southern Kuril Arc, to understand the long-term evolution of a subduction zone volcano. In Chapter 2, I obtained new K-Ar, Ar/Ar, and ^{14}C ages to create the time–cumulative volume step diagram and show that the eruption rate was high in the Early-1 and Middle stages, intermediate in the Early-2 and Late-1 stages, and low in the Late-2 stage. Besides, it was indicated that there was a clear relationship between the eruption rate and the chemical composition of volcanic products. In Chapter 3, I showed that the calc-alkaline andesites that erupted during the Middle stage were essentially formed through the magma mixing between the mantle-derived magma and crust-derived magma. The water content of the primitive end-member magma of the calc-alkaline andesite was obtained to be ~5 wt.%, which is predominantly higher than other primitive magmas that produced basalts and tholeiitic andesites to dacites. It was suggested that the water content of primary magma control the differentiation process in the crust. In Chapter 4, I carried out a geochemical study of the adakitic dacites in the Middle stage to clarify the nature and behavior of slab-derived fluids. The results showed that the adakitic dacites were not produced by partial melting of crustal rocks and fractional differentiation from mantle-derived magma, but rather by the involvement of slab-derived materials. It was indicated that the slab-derived supercritical liquid separated into aqueous fluid and hydrous melt and the former erupted as dacitic magma. In Chapter 5, it was clarified that the elemental partitioning induced by the separation of slab-derived supercritical liquid into aqueous fluid and hydrous melt would play an important role in causing the Na/K variation of primary basaltic magma. In Chapter 6, I summarized the results in Chapters 2 to 5 and discuss the controlling factors in the long-term evolution of the Rishiri Volcano. This study finally proposed that whether or not the slab-derived supercritical liquid separated into aqueous fluid and hydrous melt would determine the chemical composition of primary magma, differentiation processes in the crust, and the eruption rate at the surface and play an important role in the long-term evolution of subduction zone volcanoes.

Contents

Chapter 1. Introduction

1-1. General introduction

Subduction zone is one of the most active areas of magmatism (e.g., Miyashiro, 1974; Gill, 1981) and numerous geological, petrological, geochemical, and geophysical studies have been carried out. It has been well known that subduction zone magmatism is occurred by partial melting of mantle peridotite with an influx of slab-derived water-rich materials such as aqueous fluid, hydrous melt, and supercritical liquid (e.g., Ringwood, 1974; Kay, 1978; Gill, 1981; Sakuyama and Nesbitt, 1986; Tatsumi, 1986; Tatsumi, 1989; Elliott, 2003; Kessel et al., 2005; Portnyagin et al., 2007; Kuritani et al., 2008). The chemical composition of primary magma is changed by fractional differentiation (e.g., Bowen, 1928), assimilation (e.g., DePaolo, 1986; Kuritani et al., 2005), and/or mixing with felsic magma (e.g., Eichelberger, 1975; Sakuyama, 1979) during ascending in the crust, and finally erupted to the surface and form a volcano. In contrast, some questions about the long-term evolutionary processes of the subduction zone volcano are remaining because of paucity of case studies.

A mantle diapir model that is based on distribution, size, compositional variation, and lifetimes of the volcanoes, has been proposed as a controlling factor for subduction zone volcanism. However, since there were some problems with the heat content and the velocity of ascending (e.g., Ida, 1983), the fluid transfer model (e.g., McKenzie, 1984) has also been proposed from the numerical studies. These two hypotheses have been debated for years, but they have yet to be settled, which is one of the major impediments to our understanding of the material cycles of the Earth's interior, especially subduction zones. This is because there have been few case studies to verify the fluid transfer model using natural samples as opposed to the mantle diapir model that proposed from observations in nature. Although the relationship between medium-term (~10^4 years) volcanic activity and slab-derived fluid was examined in recent years (e.g., Yokoyama et al., 2003), the controversy has yet to be resolved because the timescale of the study is too short compared to the lifespan of volcanic activity. Therefore, we are not even given the answers to some fundamental questions about the subduction zone volcanism. For example, how to start, evolve, and end the subduction zone volcanism? What is the factor to control the lifespan (e.g., 10^4 to 10^5 years; Moriya, 1981; Tomiya, 1991; Yamamoto et al., 2018) of the subduction zone volcano? These questions are left unanswered because (1) there are few volcanoes that we can continuously collect samples from the beginning to the end of volcanic activity, (2) it is difficult to dating the volcanic products, (3) it is difficult to extract the information of the processes in the deep part corresponding to from the subducting slab to the mantle because andesitic magmas are predominant in the subduction zone.
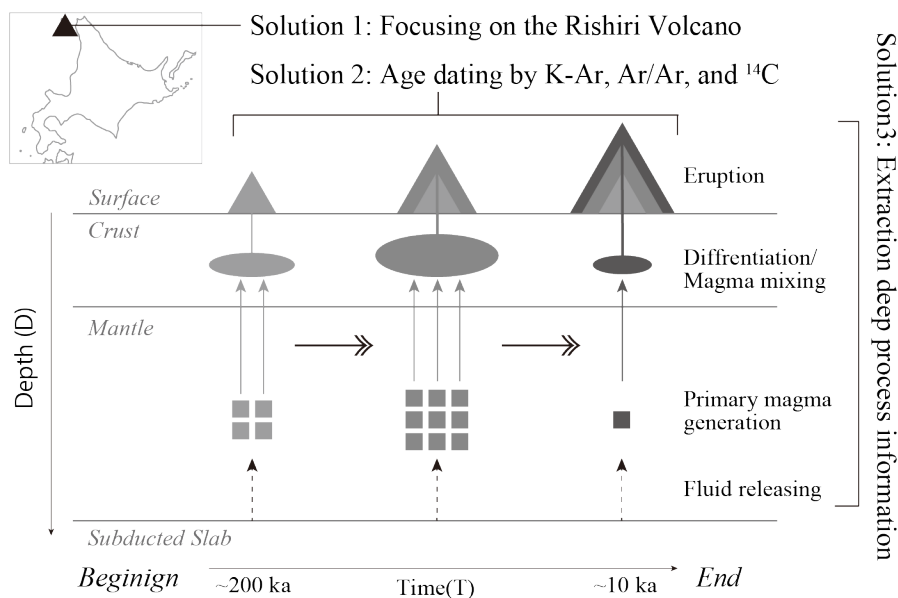
Figure 1-1 A schematic illustration of this study. See text for detail.

In this situation as described above, this study aims to elucidate the long-term evolutionary processes by focusing on Rishiri volcano, southern Kuril Arc (e.g., Ishizuka, 1999; Ishizuka and Nakagawa, 1999). At the Rishiri Volcano, it is possible to collect continuously the volcanic products of the beginning to the end of the activity (solution to problem 1). In addition, recent advances in dating methods (e.g., K-Ar and Ar/Ar methods) can date the volcanic products which erupted from 100 ka to 10 ka (solution to problem 2). Therefore, if we can extract the petrological and geochemical information of deeper part process from the andesitic to dacitic magmas in addition to basaltic magmas (solution to problem 3), we can elucidate the long-term evolution of subduction zone volcano on a spatial and temporal scale from the subducting slab to the surface and from the beginning to the end of the volcanic activity (Fig. 1-1). In this study, I collected the volcanic products and conducted the following detailed studies on them.

I first determine the eruption ages by the K-Ar, Ar/Ar, and ^{14}C methods using lavas and radiogenic carbon and re-examined the evolution history of the volcano (see Chapter 2). The next step was a petrological study of the calc-alkaline andesite to elucidate the effects of differentiation, assimilation, and mixing in the crust and the factors that control the crustal process (see Chapter 3). In the next two chapters, I clarified the nature and behavior of slab-derived supercritical liquid using the adakitic dacite (see Chapter 4), and the magma generation processes and conditions of the primary magmas that show compositional variation (see Chapter 5). Finally, I summarized the results of chapter 2 to 5 and discussed the factors that determine the long-term evolution of the Rishiri volcano (see Chapter 6).

1-2. Geological setting and background of the Rishiri Volcano

Rishiri Volcano is located ~550 km behind the trench of the junction between the Kuril Arc and Northeastern (NE) Japan Arc and is 300 km above the Wadati-Benioff Zone (Fig. 1-2). The volcano forms an island (Rishiri island) ~20 km west of the north-western tip of Hokkaido, Japan (Fig. 1-1). Behind the Kuril Arc and NE Japan Arc systems, back-arc spreading associated with the opening of the Sea of Japan had been active until ~12 Ma (Otofuji et al., 1985).

The geology of Rishiri Volcano was described by Abe (1934), Matsui et al. (1964), Kobayashi (1987), and Ishizuka (1999). According to Ishizuka (1999), vol-
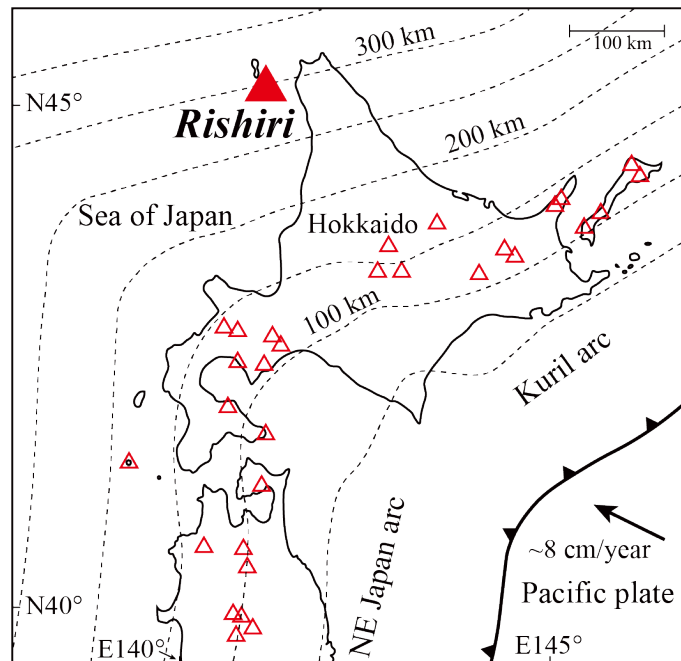
Figure 1-2 Index map showing the location of the Rishiri Volcano. The thin gray dashed lines denote slab surface contours, and the solid red triangles indicate the locations of active volcanoes. The slab surface contours and the subduction direction are from Kita et al. (2010).

canic activity can be divided into three stages: the Early, Middle, and Late stages, and the Early and Late stages can each be further subdivided: the Early-1, Early-2, Middle, Late-1, and Late-2 stages (Fig. 1-3 and 1-4). The eruption rates of each stage were estimated to be >0.1 km^3/ky, >0.4 km^3/ky, >0.4 km^3/ky, >0.35 km^3/ky, and >0.09 km^3/ky, respectively (Ishizuka, 1999).

Volcanic products of the Early-1 and Early-2 stages consist mainly of andesitic lavas and pyroclastic flow deposits that formed the lower part of the stratovolcano, and dacitic to rhyolitic lava domes on the northwestern and southeastern flank of the volcano. The main edifice of the stratovolcano was produced during the Middle stage and is characterized by calc-alkaline andesitic lavas and pyroclastics, and dacitic lavas. The Late-1 stage produced high-Na/K alkali basalts and intermediate tholeiite series lavas that were erupted on the western flank of the volcano, and during Late-2 Stage low-Na/K alkali basalts erupted on the southern and northern flanks of the volcano (Ishizuka, 1999; Ishizuka and Nakagawa, 1999). The genesis and differentiation processes of alkali basalts and tholeiitic-series andesites to dacites that erupted during the Late-1 and Late-2 stages have been examined by Kuritani, (1998, 1999a, 1999b, 1999c, 2001), Kuritani and Nakagawa (2016), and Kuritani et al. (2005, 2007, 2008).
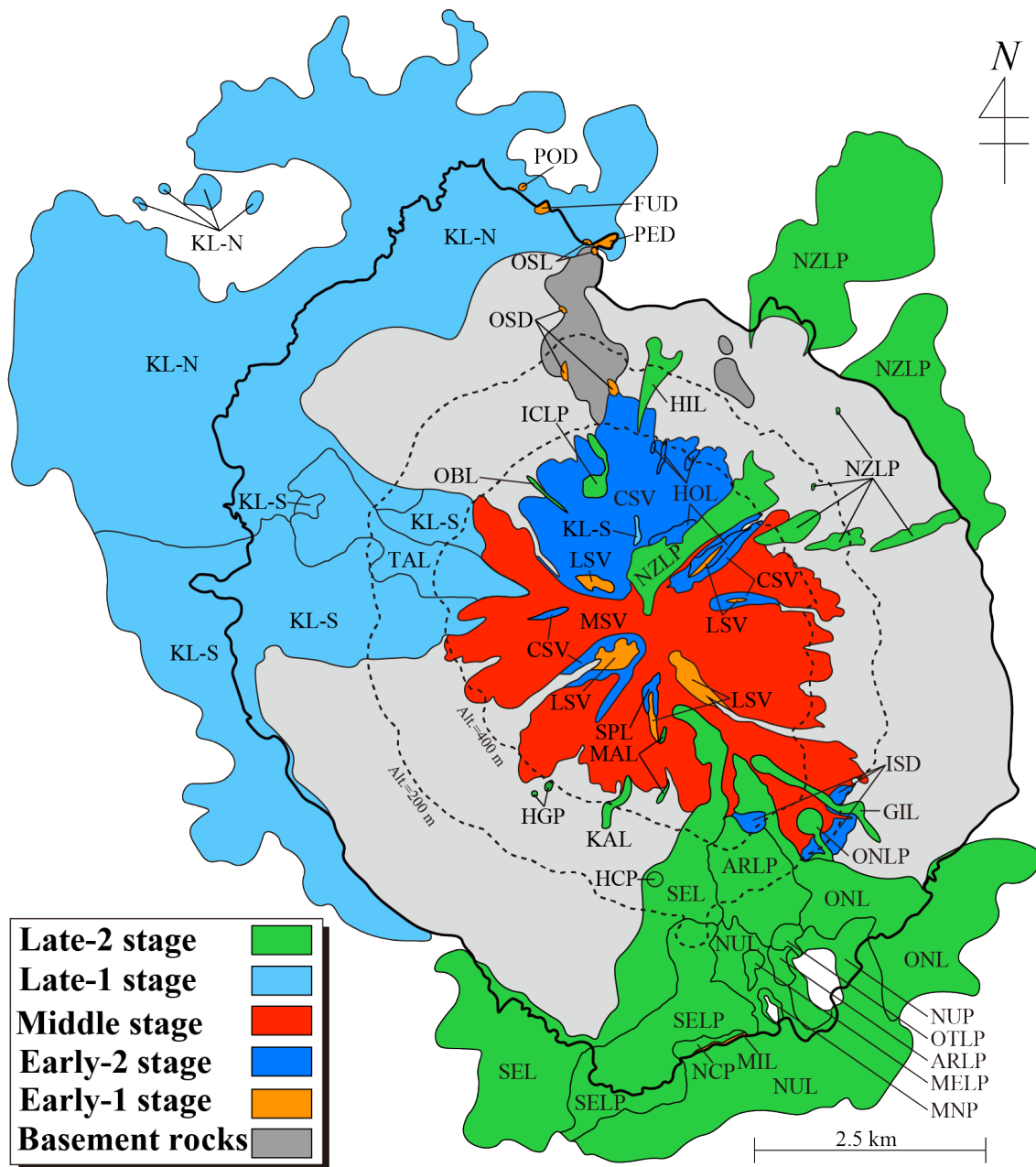
Figure 1-3 Geological map of the Rishiri Volcano after Ishizuka (1999). In this figure, abbreviations are L: lava, D: lava dome, P: pyroclastics, LP: lava and pyroclastics, OSL: Oshidomari L, PED: Peshimisaki D, OSD: Oshidomari Ponyama D, POD: Ponmoshirito D, FUD: Fujino D, MIL: Minamihama L, LSV: Lower part of stratovolcano, SPL: Sepaushikawa L, HOL: Horyosawa L, CSV: Chokanyama stratovolcano, ISD: Ishiyama D, MSV: Main part of stratovolcano, KL-N: Kutsugata north L, KN-S: Kutsugata south L, TL: Tanetomi L, NCP: Nochu P, MAL: Maoyanisawa L, KAL: Kamiisokawa L, HGP: Hagoromokawa P, HIL: Himenuma L, ICLP: Ichinosawa LP, OBL: Obiyatan'naisawa L, ARLP: Araragiyama LP, SEL: Senhoshi L, NZLP: Nozuka LP, NUL: Numaura L, ONLP: Oniwaki Ponyama LP, NUP: Numaura P, ONL: Oniwaki L, HCO: Hachibuseyama P, SELP: Senhoshi Ponyama LP, GIL: Giboshinuma L, MNP: Minamihama P, MELP: Menuushoro Ponyama LP, and OTLP: Otatomari Ponyama LP.

9
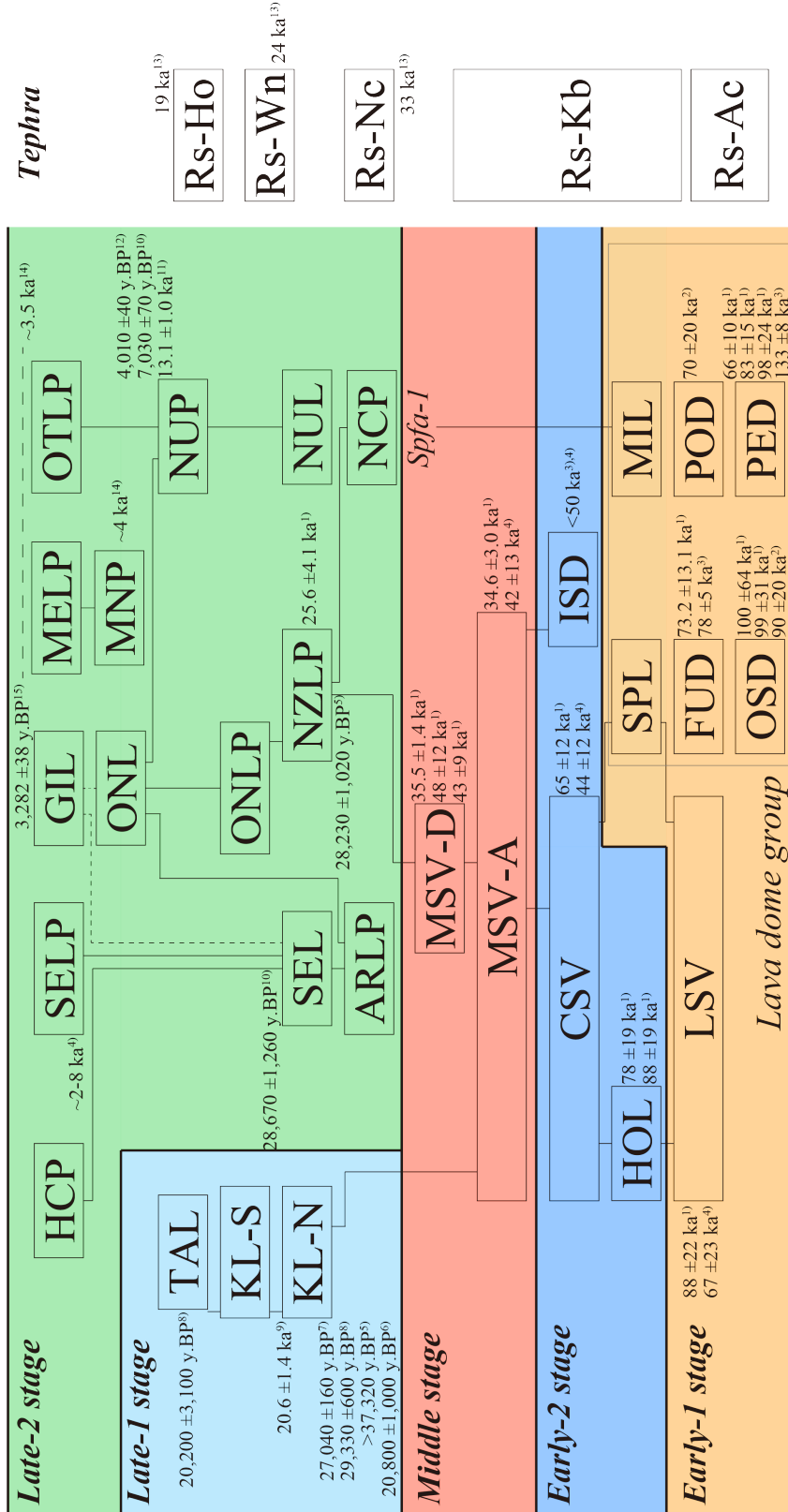
Figure 1-4 Summary of volcanic activity of the Rishiri Volcano after Ishizuka (1999) and Ueki and Kondo (2010). In this figure, abbreviations are Rs-Ho: Rishiri-Hotoku tephra, Rs-Wn: Rishiri-Wankonosawa tephra, Rs-Nc: Rishiri-Nochu tephra, Re-Kb: Rishiri-Kabutonuma tephra, and Rs-Ac: Rishiri-Acharu tephra. In this figure, the ages are taken from the following studies: 1: this study, 2: Ueki and Kondo (2010), 3: Ishizuka and Nakagawa (1994), 4: Ishizuka (1999), 5: Miura and Takaoka (1993), 6: Matsui et al. (1967), 7: Ueki and Kondo (2008), 8: Kuritani et al. (2007), 9: Kondo and Tsukamoto (2009), 10: Miura (1993), 11: Kondo (2015), 12: Igarashi (2006), 13: Kondo et al. (2007), 14: Sato et al. (2013), and 15: Kondo et al. (2015).

Chapter 2. Long-term activity of the Rishiri Volcano: Constrains from geology and geochronology

Abstract

      The eruption rate, which is the cumulative eruption volume divided by the activity time, is one of the useful indicators of the long-term evolution of volcanic activity. It is well known that the activity of the subduction zone volcano typically continues for 10^4-10^5 years and the eruption rate changes during the activity. Why does the eruption rate change during a volcanic activity? What is the dominant factor in changing eruption rates? To clarify this issue, I focus on the activity of the Rishiri Volcano, where almost all the ejecta can be observed from the beginning to the end of the volcanic activity. The activity is characterized by the coexistence of alkali basalt, tholeiitic andesite to dacite, and calc-alkaline andesite to dacite. The activity is divided into five stages: the Eearly-1, Early-2, Middle, Late-1, and Late-2 stages. In this study, 13 samples, 3 samples, and 1 sample were analyzed by K-Ar, Ar/Ar, and ^{14}C method, respectively, to estimate the long-term change of the eruption rate. The volcanic activity began with a high eruption rate in the Early-1 stage and then declined once in the Early-2 stage. The eruption rate of the Middle stage, which is after the Early-1 stage, was the highest during the volcanic activity and decreased in the Late-1 stage and further decreased at the Late-2 stage. The whole-rock chemical composition of each stages is characterized by calc-alkaline andesites to dacites during the Early-1 and Middle stages, tholeiite-series andesites to dacites with high-Na/K basalts during the Early-2 and Late-1 stages, and low-Na/K basalts during the Late-2 stage. It is also suggested that the differences of magmatic processes in the mantle or crust would control the eruption rate.

2-1. Introduction

      The time-to-cumulative volume step diagram proposed by Nakamura (1964) and the eruption rate which is the cumulative eruption volume divided by the time are effective methods to quantify the long-term evolution of the volcanic activity. The lifespan of the subduction zone volcano thought to be about 10^4 to 10^5 years, but how their activities change during such a long-term period is still under debate as described in the general introduction. One of the problems was the difficulty of dating. In many cases, the relatively young volcanoes are escaped from the erosion and are suitable to reconstruct the history of long-term volcanic activity. However, it had been difficult to determine the eruption age for the young ejecta (e.g., < 0.1 Ma). After the 1990's, the sensitivity of the mass spectrometer used in the K-Ar method has been improved and the Ar/Ar method, which is an advanced version of the K-Ar method, is developed. As a result, it has been possible to date the eruption ages to the lava samples of < 0.1 Ma (e.g., Itaya, 1984). In recent years, volcanic products that younger than one million years have been dated, and eruption

history have been reconstructed on long-term scales corresponding to the volcanic lifespan of 10^4 to 10^5 years (e.g., Hildreth and Lanphere, 1994; Hildreth et al., 2003; Frey et al., 2004; Nishiki et al., 2011; Conway et al., 2016). In this study, I determine the age of 17 samples by K-Ar, Ar/Ar, and ^{14}C method using the lavas and charcoal. In addition, I draw the time-to-cumulative volume step diagram using the compiled chronological data and clarified the long-term evolution of the eruption rate.

2-2. Analytical methods

For the K-Ar dating, the mineral separation was carried out in the Graduate School of Science, Hokkaido University. Additional mineral separation, quantitative analysis of Potassium, and isotopic analysis of Argon were carried out in the Pheasant Memorial Laboratory, Institute for Planetary Materials, Okayama University. Rock specimens were sliced into slabs about 5 to 10 mm in thickness using a rock cutter. Then, weathered and altered parts were removed. The flesh slabs were rinsed with deionized water until the water was no longer cloudy and dried in an electric furnace at 100 °C for > 1 night. The washed slabs were crushed using an iron mortar and arranged to a size of 60-80 mesh (aperture is ~187 to 250 μm). The arranged samples were washed and dried again, and then magnetic minerals were removed using a hand-magnet and an isodynamic separator. Finally, the remaining phenocrysts (e.g., plagioclase) in the samples were removed using a microscope and tweezers. For the quantitative analysis of Potassium, the separated groundmass samples were dissolved by acid digestion following Yokoyama et al. (1999) and determined using an atomic absorption/flame spectrophotometer, Hitachi Type 180-30. The isotopic ratios of Argon were determined using a mass spectrometer for noble gases (VG5400), followed the methods given in Nagao et al. (1996). The results of the analysis were rejected for samples with an atmospheric argon contamination rate of > 99.5 %. For samples that were analyzed more than once in the same sample, the average age was adopted and the error of the average ages was calculated by the method given in Tsukui et al. (1985).

For reliable ^{40}Ar/^{39}Ar dating, I collected samples with holocrystalline groundmass. The ^{40}Ar/^{39}Ar age for groundmass of dacite and preceding andesite are obtained at the Argon Geochronology Laboratory, Oregon State University via incremental heating of hand-picked holocrystalline groundmass samples with laser irradiation. The ^{40}Ar/^{39}Ar isotopes are analysed by a multi-collector mass spectrometer (Thermo Scientific Model ARGUS-VI) and decay constants in this study from Min et al. (2000) with 2σ internal errors.

Radiocarbon ages were determined at the Institute of Accelerator Analysis Ltd. by accelerator mass spectrometry (AMS). A charcoal sample was analyzed after removing impurities by AAA (Acid-Alkali-Acid) method. The half decay period of the K nuclides used for calculations in this study is 5,568 years (Stuiver and Polach, 1977).

2-3. Results

12 samples, OC-10 (MSV-D, the Middle stage), OC-8 (MSV-D, the Middle stage), AF-202 (CSV, the Early-2 stage), HOL-2 (HOL, the Early-2 stage), HOL-3 (HOL, the Early-2 stage), OK-4 (LSV, the Early-1 stage), FUD-1 (FUD, the Early-1 stage), PED-1 (PED, the Early-1 stage), PED-2 (PED, the Early-1 stage), PED-3 (PED, the Early-1 stage), OSD-1 (OSD, the Early-1 stage), and OSD-2 (OSD, the Early-1 stage), are analyzed by K-Ar method and the age data are presented in Table 2-1.

3 samples, YM-12 (MSV-A, the Middle stage), OS-2 (MSV-D, the Middle stage), and KT-200 (NZLP, the Late-1 stage) are dated by the $^{40}Ar/^{39}Ar$ method. The age spectra and isochron plots derived from the $^{40}Ar/^{39}Ar$ incremental heating experiments are presented in Fig. 2-1.

A charcoal sample, which was collected from just below the Nozuka lava flow, was dated by the ^{14}C method. The data and calibration age that calculated by the OxCalc4.3 program (Bronk Ramsey, 2009) using the IntCal13 database of Reimer et al. (2013) are presented in Table 2-2 and 2-3, respectively.
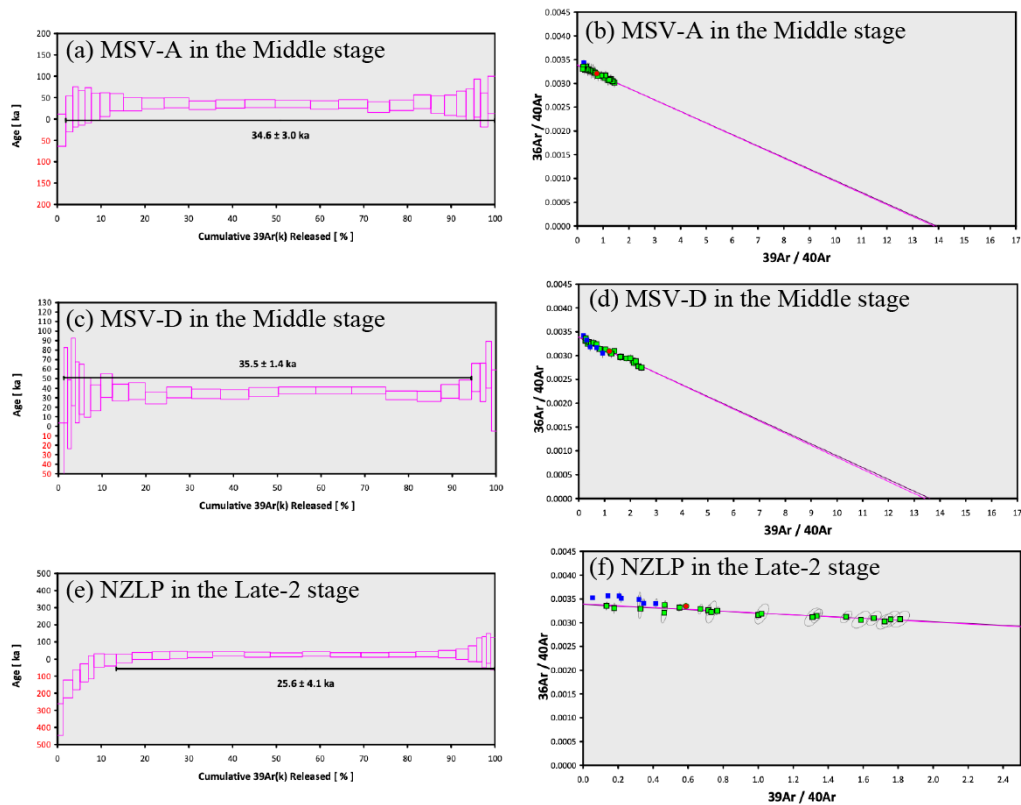
Figure 2-1 The age spectra (plateaus; a, c, e) and isochron plots (b, d, f) derived from the $^{40}Ar/^{39}Ar$ incremental heating experiments on (a, b) the lowest part of the calc-alkaline andesite lava (MSV-A) of the main stratovolcano in the Middle stage, (c, d) the top part of the calc-alkaline dacite (MSV-D) lava of the main stratovolcano in the Middle stage, and (e, f) the top part of the Nozuka lava (NZLP) in the Late-1 stage from Rishiri Volcano. Plateau age (±1σ) is calculated from the weighted mean of the individual steps whose width is the proportion of total sample ^{39}Ar released and whose height is 2σ error.

Table 2-1 Results of K-Ar dating.

Stage Unit name		K (wt.%)	^{36}Ar (10^{-9}cm^{3}STP/g)	^{40}Ar/^{36}Ar	^{40}Ar rad (10^{-9}cm^{3}STP/g)	Air fract.	Age (Ma)	1 se (Mys)
Middle stage								
MSV-D	OC-10	1.29	0.613±0.010	300.2±1.4	2.6±0.9	98.6	0.0517	0.0175
	OC-10		0.594±0.010	299.7±1.4	2.2±0.8	98.8	0.0443	0.0159
	OC-10 Av.						**0.0480**	**0.0124**
MSV-D	OC-8	1.37	0.562±0.009	300.3±1.2	2.4±0.7	98.6	0.0457	0.0129
	OC-8		0.533±0.009	299.9±1.2	2.1±0.6	98.7	0.0392	0.0117
	OC-8 Av.						**0.0425**	**0.0093**
Early-2 stage								
CSV	AF-202	1.37	0.733±0.012	301.0±1.2	3.7±0.8	98.3	0.0694	0.0157
	AF-202		0.722±0.012	300.4±1.1	3.2±0.8	98.5	0.0603	0.0151
	AF-202 Av.						**0.0649**	**0.0118**
HOL	HOL-2	0.93	1.027±0.016	298.6±0.9	2.7±0.9	99.1	0.0743	0.0259
	HOL-2		1.020±0.016	298.9±0.9	2.9±0.9	99.0	0.0810	0.0262
	HOL-2 Av.						**0.0777**	**0.0187**
HOL	HOL-3	0.94	0.976±0.015	299.3±1.0	3.2±1.0	98.9	0.0883	0.0275
	HOL-3 Av.						**0.0883**	**0.0275**
Early-1 stage								
LSV	OK-4	0.85	1.020±0.017	305.2±5.0	3.2±1.0	98.9	0.0979	0.0291
	OK-4		0.924±0.014	298.8±0.9	2.6±0.8	99.1	0.0771	0.0242
	OK-4 Av.						**0.0875**	**0.0216**
FUD	FUD-1	1.55	0.656±0.011	301.9±1.2	3.9±0.8	98.1	0.0641	0.0132
	FUD-1		0.689±0.011	303.2±1.2	4.9±0.8	97.6	0.0822	0.0136
	FUD-1 Av.						**0.0732**	**0.0131**
PED	PED-1	1.41	1.279±0.020	299.6±0.9	4.7±1.1	98.8	0.0856	0.0208
	PED-1		1.259±0.020	299.5±0.9	4.4±1.1	98.8	0.0803	0.0196
	PED-1 Av.						**0.0830**	**0.0145**
PED	PED-2	1.39	1.118±0.017	300.7±1.2	5.3±1.3	98.4	0.0977	0.0240
	PED-2 Av.						**0.0977**	**0.0240**
PED	PED-3	1.69	0.558±0.009	303.8±1.2	4.4±0.7	97.4	0.0667	0.0100
	PED-3 Av.						**0.0667**	**0.0100**
OSD	OSD-1	1.63	3.351±0.051	297.9±1.2	6.3±4.04	99.4	0.1000	0.0638
	OSD-1 Av.						**0.1000**	**0.0638**
OSD	OSD-2	1.61	1.925±0.029	300.03±0.9	7.7±1.7	98.7	0.1242	0.0273
			1.771±0.028	298.6±0.9	4.5±1.5	99.1	0.0742	0.0248
	OSD-2 Av.						**0.0992**	**0.0311**

Table 2-2 Result of the ^{14}C dating.

Analysis No.	Sample Name	δ^{13}C (‰)	Libby Age (yBP)	pMC (%)
IAAA-190494	20180808-1	-24.78 ± 0.18	22,370 ± 110	6.17 ± 0.08

Table 2-3 Result of the calibration of the ^{14}C dating.

for Cal. Age (yBP)	1σ (Cal. yBP)	2σ (Cal. yBP)
22,371 ± 110	26870–26449 (68.2 %)	27070–26287 (95.4 %)

2-4. Discussion

2-4-1. Evaluation of ages

To evaluate our new ages, the published age data were compiled. Fig. 2-2 shows the stratigraphy of volcanic products and their ages. Our new ages are basically consistent with the stratigraphy and the published ages within the error. Therefore, the results of this study can be judged to be valid.

2-4-2. Long-term changing of the eruption rate

For the estimation of the long-term changing of the eruption rate, I first estimate the dense rock equivalent (DRE value; volume (km^3) ×deposit density (g/cm^3)/dense rock density (g/cm^3)). The eruption volume of each lava and pyroclastics are based on the values determined by Ishizuka (1999). In this data, the volume of each tephra was calculated using the method of Hayakawa (1985) based on the isopach drawn by Miura (1995). The deposit density of lava, pyroclastics, scoria, and pumice are used 2.4, 1.5, 1.0, and 0.7 g/cm^3, respectively (Nakamura, 1964; Hayakawa, 1985). A dense rock density of 2.7 g/cm^3 is also used.
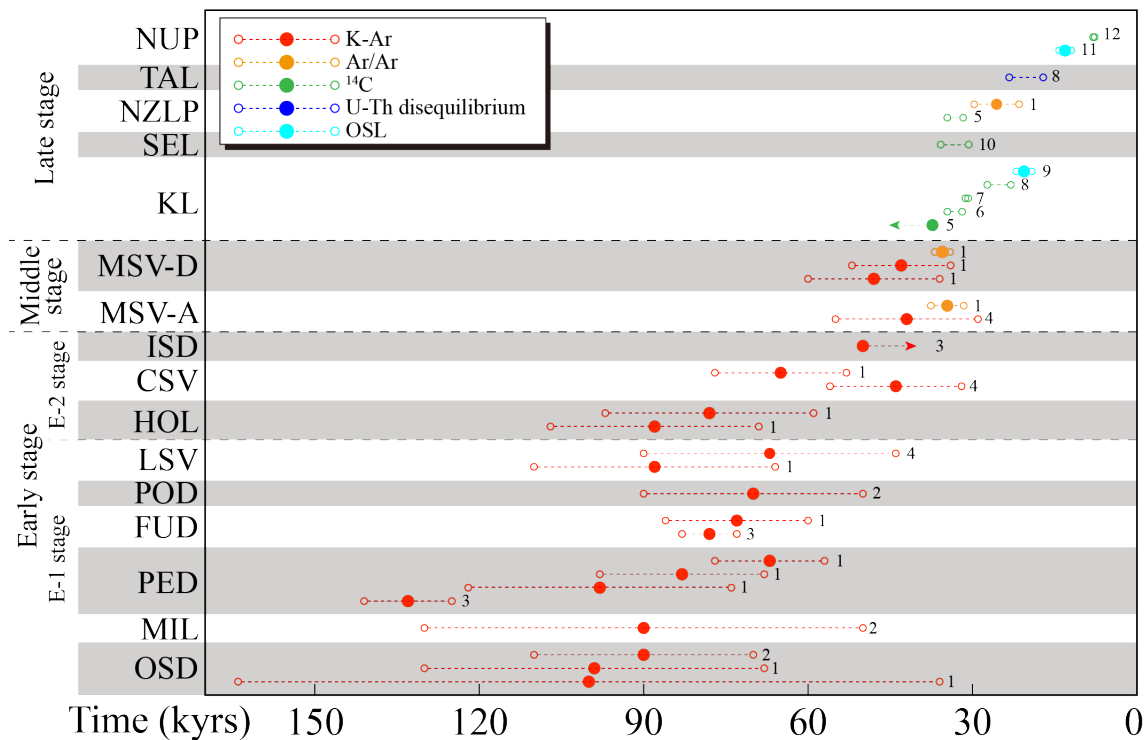
Figure 2-2 Age–stratigraphy diagram for evaluation of the ages. In this diagram, the vertical axis indicates the stratigraphy. The age data are taken from the following studies: 1: this study, 2: Ueki and Kondo (2010), 3: Ishizuka and Nakagawa (1994), 4: Ishizuka (1999), 5: Miura and Takaoka (1993), 6: Matsui et al. (1967), 7: Ueki and Kondo (2008), 8: Kuritani et al. (2007), 9: Kondo and Tsukamoto (2009), 10: Miura (1993), 11: Kondo (2015), and 12: Igarashi (2006).

In this study, I estimate the average eruption rate for each stage, because it is difficult to date the ages of all volcanic products. For the ages of the boundaries between the Early-1 and Early-2 stages, the Early-2 and Middle stages, and the Middle and Late-1 stages, I use the ages of the Horyosawa lava (HOL; earliest activity in the Early-1 stage), the lowest part of the main stratovolcano andesite (MSV-A; the Middle stage), and the top part of the main stratovolcano dacite (MAV-D; the Middle stage), respectively. On the other hand, since there was a gradual change in activity from the Late-1 to Late-2 stages, I define the Late-1 stage activity as the period of the top part of the main stratovolcano dacite (MSV-D) to the Tanetomi lava (TAL) and the Late-2 stage activity as the period of the Senhoshi lava (SEL) to the Giboshinuma lava (GIL) activity. The new time-cumulative volume step diagram drawn in this study is shown in Fig. 2-3.

It was pointed out that the activity of the Rishiri Volcano started with a low eruption rate in the Early-1 stage, increased in the Early-2 stage, and reached the maximum in the Middle stage, and then decreased from the Late-1 stage to the Late-2 stage (Ishizuka, 1999). However, the new step diagram drawn this study suggests different long-term changes from the results in the previous study. I suggest that the activity of the Rishiri Volcano started with a high eruption rate in the Early-1 stage, decreased in the Early-2 stage, reached its highest rate in the Middle
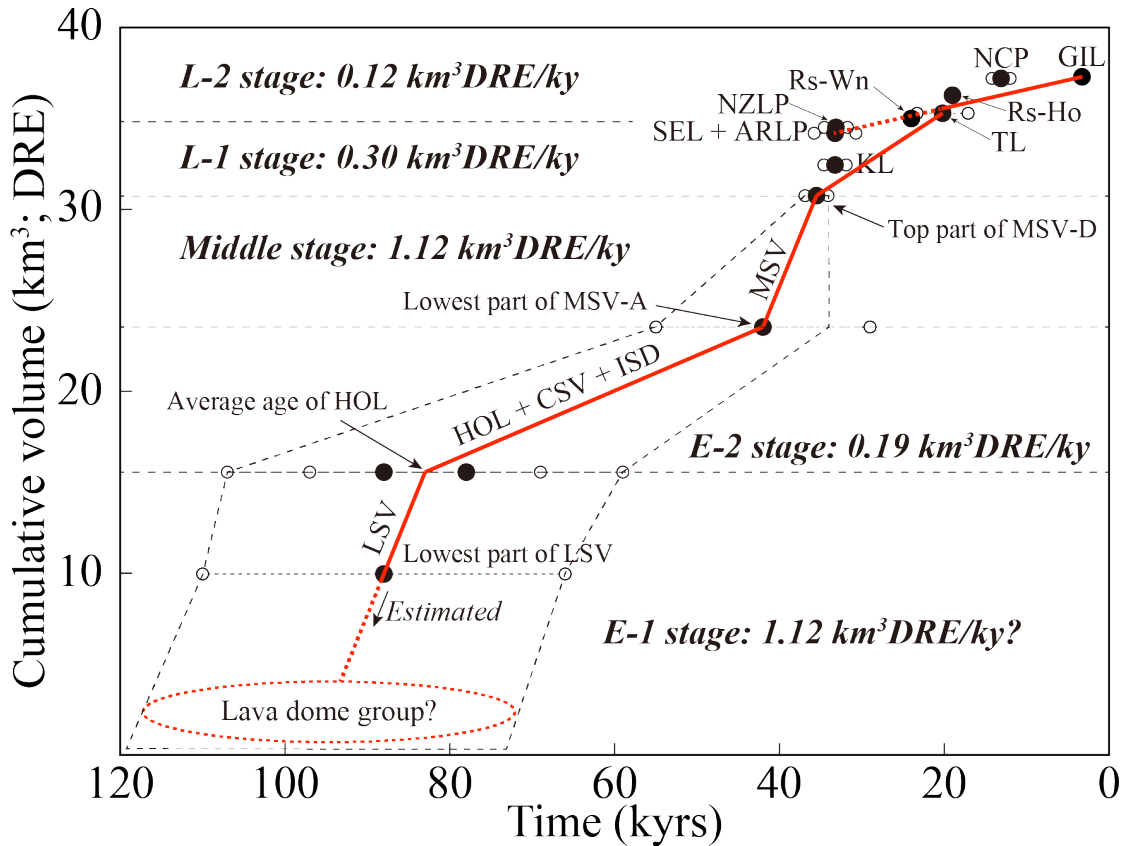
Figure 2-3 Cumulative volume–time diagram of the Rishiri Volcano. Estimated eruption rates of each stage are also shown in the figure.

stage, and decreased from the Late-1 stage to the Late-2 stage. In other words, the eruption rate in the Early-1 and Early-2 stages was higher and lower, respectively, than the estimation in the previous study (Ishizuka, 1999). The average eruption rate of the Early-1, Early-2, Middle, Late-1, and Late-2 stages are obtained to be 1.12, 0.19, 1.12, 0.3, and 0.12 km^3DRE/kyrs, respectively. Therefore, the Early-1 and Middle stages can be defined as the high-eruption rate stage, the Early-2 and Late-1 stages as the intermediate-eruption rate stage, and the Late-2 stage as the low-eruption rate stage.

2-4-3. Comparison with whole-rock composition

A comparison between the eruption rates and whole-rock composition of volcanic products shows that the calc-alkaline andesites to dacites erupted during the high-eruption rate stages, the high-Na/K type basalts and tholeiitic andesites to dacites erupted during the intermediate eruption rate stages, and the low-Na/K type basalts erupted during the low-eruption rate stage (Fig. 2-4). It is suggested that the eruption rate related to the whole-rock composition of the volcanic products, and that would be controlled by the differences in magma differentiation processes and magma generation conditions in the crust and mantle. These details will discuss in Chapter 6.

Figure 2-4 Whole-rock major element compositions of volcanic products from Rishiri Volcano shown in (a) FeO*/MgO–SiO$_2$ and (b) Na$_2$O+K$_2$O–SiO$_2$ diagrams. In (a), discrimination line between the calc-alkaline and tholeiite series is taken from Miyashiro (1974). Whole-rock compositions are taken from Ishizuka (2000), Kuritani and Nakagawa (2016), and Taniuchi et al. (2020a, 2020b).

2-5. Conclusion

1. To draw the time-to-cumulative volume step diagram and estimate the long-term changing of the eruption rate, I performed K-Ar, Ar/Ar, and ^{14}C dating and obtained valid ages.
2. I found that the evolution of the eruption rate of the Rishiri Volcano was more complicated than previously thought, with the high rate in the Early-1 stage, the low rate in the Early-2

stage, the highest rate during in Middle stage, and the gradual decrease from the Late-1 to Late-2 stage.

3. Based on the estimation of the eruption rate, the Rishiri activity could be divided in three stages: the high-eruption rate stage (the Early-1 and Middle stages), intermediate-eruption rate stage (the Early-2 and Late-1 stages), and low-eruption rate stage (the Late-2 stage).

Chapter 3. Magmatic processes in the crust: Constrains from the calc-alkaline andesites

Abstract

      Calc-alkaline andesite is a typical rock series in many island and continental arcs, and it commonly coexists with tholeiitic series rocks in individual volcanoes. In this chapter, the main controlling factors on the occurrence of calc-alkaline magmatism are examined for andesitic lavas in the Middle stage. The whole-rock SiO_2 contents of the lavas range from 57.9 wt.% to 61.9 wt.%, and they are classified as calc-alkaline series. The lavas have petrographical and mineralogical features that show evidence of magma mixing. The whole-rock compositional variations of the lavas indicate that three end-member magmas were involved in their generation, a primitive mafic end-member magma, an evolved mafic end-member magma, and a felsic end-member magma. I suggest that the primitive mafic end-member magma represents a near primary magma generated in the upper mantle, the evolved mafic end-member magma was derived from the primitive magma by olivine fractionation, and the felsic end-member magma was produced primarily by partial melting of the crust. The primitive end-member magma is estimated to contain ~5 wt.% water, which is much higher than those of the primary basaltic magmas of other volcanic stages of Rishiri that do not include calc-alkaline magmas. Based on this observation, I suggest that the water content of the primary magma was the main factor controlling the genesis of calc-alkaline magmatism at Rishiri. The more hydrous the primary magma and its derivative magma, the more extensive the melting of the crust due to the higher water flux from the solidifying magma chamber.

3-1. Introduction

      Calc-alkaline andesite is a typical rock series in many island and continental arcs (e.g., Miyashiro, 1974), and its chemical composition is similar to the average composition of the continental crust (e.g., Rudnick and Gao, 2003). Therefore, the petrogenesis of calc-alkaline andesites has long been one of the most debated topics in petrology. Numerous hypotheses for the genesis of calc-alkaline andesite have been proposed, and they can roughly be divided into the following origins: (1) crystal differentiation from mantle-derived primary basaltic magma (e.g., Yoder and Tilley, 1962; Gill, 1981; Sisson and Grove, 1993); (2) magma generation in the upper mantle under some specific conditions, such as partial melting of mantle peridotite under low-pressure or high-water concentration (e.g., Kushiro, 1969; Tatsumi, 1982; Hirose, 1997; Tamura et al., 2016); (3) reaction of slab-derived fluid (e.g., adakitic melt and supercritical liquid) with mantle peridotite (e.g., Kay, 1978; Kepezhinskas et al., 1996; Kelemen et al., 1998; Kawamoto et al., 2012); (4) partial melting of mafic rocks in the lower to middle crust (e.g., Takahashi, 1986; Petford and Atherton, 1996); and (5) magma mixing between mafic and felsic magmas (e.g.,

Sakuyama, 1981). Among these processes, magma mixing may be one of the main processes responsible for the generation of calc-alkaline andesite magmas, since calc-alkaline rocks often show petrological and geochemical evidence of magma mixing (e.g., Sakuyama, 1981; Kay et al., 1982; Kay and Kay, 1985; Streck et al., 2007).

Since calc-alkaline rocks occur preferentially in mature continental and island arcs with a relatively thick crust, tectonic setting and crustal thickness have been considered to be important factors controlling the occurrence of calc-alkaline magmas (Baker, 1973; Miyashiro, 1974; Gill, 1981). However, in volcanic systems where calc-alkaline rocks and tholeiitic rocks coexist (Sakuyama, 1981; Bau and Knittel, 1993; Baker et al., 1994), calc-alkaline magmatism does not always occur throughout the evolution of the volcanic system. Calc-alkaline rocks dominate some stages of the volcanic activity, while tholeiitic rocks dominate others. This observation clearly suggests that there must be additional factors controlling the occurrence of calc-alkaline magmatism. Since factors may vary between volcanic systems, many petrological studies have been carried out to understand the factors that control the differences regarding the origin of calc-alkaline and tholeiitic compositional trends at individual volcanoes (e.g., Sakuyama, 1981; Fujinawa, 1988; 1990; Bau and Knittel, 1993; Baker et al., 1994; Hunter and Blake, 1995; Hunter, 1998). However, this is not an easy task. The generation of calc-alkaline andesitic magma commonly involves a parental mafic magma as described above, and, therefore, it is important to compare the characteristics of the parental magmas of calc-alkaline magma with those of the parental tholeiitic magma. However, it is challenging to restore the parental mafic magma composition from well-mixed products (i.e., calc-alkaline andesites), except where melt inclusions in mafic minerals that were derived from the parental mafic magma are available (e.g., Schiano et al., 2001; Le Voyer et al., 2010; Schiavi et al., 2012; Narvaez et al., 2018).

In this study, I carried out petrological and geochemical investigations on calc-alkaline andesitic lavas from Rishiri Volcano, southern Kuril Arc, to elucidate the factors that control the genesis of calc-alkaline magmatism. The volcano is characterized by the coexistence of alkali basaltic lavas and intermediate lavas of the tholeiite and calc-alkaline series (Katsui, 1953; Kobayashi, 1989; Ishizuka and Nakagawa, 1999). It has been suggested that calc-alkaline andesites occurred in the volcanic stage with the highest eruption rates during the evolution of the volcano (Ishizuka and Nakagawa, 1999). Based on petrological analyses of calc-alkaline andesitic lavas, I show that magmas were produced by mixing of three end-member magmas: a primitive mafic magma, an evolved mafic magma, and a felsic magma. I estimate the petrological characteristics of the primitive end-member magma in detail, using the whole-rock compositional variation of the lavas and how the petrographical features systematically vary with the whole-rock compositions, due to the absence of good melt inclusions in the phenocrysts. Finally, I compare the petrological characteristics of the primitive end-member magma with those of primitive alkali basalts

from other eruption stages at Rishiri to determine the factors responsible for the generation of calc-alkaline andesitic magmas.

3-2. Geological and petrological background of the calc-alkaline andesite

The calc-alkaline andesitic lavas and pyroclastics, investigated in this study, belong to the Middle stage of the volcanic activity (Fig. 3) and have been dated at 42 ±13 ka and 34.6 ±3.0 using the K-Ar method by Ishizuka (1999) and Ar/Ar method by this study (See detail in the Chapter 2). They are partly covered by dacitic lavas erupted during the same stage. Field observations suggest that the andesitic lavas and pyroclastics consist of at least 10 layers with overlain by dacitic lava. In this study, 58 samples were collected from the main edifice of the stratovolcano. Whole-rock major element analyses were performed for all samples. Trace elements and Sr–Nd–Pb isotopic analyses were performed for selected samples.

3-3. Analytical methods

Whole-rock major and trace element analyses, and Sr, Nd, and Pb isotopic analyses were carried out at the Graduate School of Science, Hokkaido University. Rock specimens were crushed to coarse chips 3–5 mm in diameter. All xenoliths and xenocrysts optically observed in the andesites were removed for whole-rock analysis. The fresh chips were rinsed with deionized water in an ultrasonic bath for >5 h and then dried at 100 °C for >12 h. The washed chips were powdered with an alumina rod in a polycarbonate tube using a Yasui-Kikai Multi-beads shocker at Hokkaido University. The powdered samples were ignited at 900 °C for >12 h in a muffle furnace, and loss on ignition (LOI) was determined gravimetrically. Concentrations of major and some trace elements (Sc, V, Cr, Co, and Ni) were determined by X-ray fluorescence (XRF) using a Spectoris MagiX PRO. Glass beads were prepared by fusion with an alkali flux (2:1 sample dilution), consisting of a 4:1 mixture of lithium tetraborate and lithium metaborate. Additional trace elements were analyzed by a single quadrupole inductively coupled plasma mass spectrometry (ICP–MS), using a Thermo Fisher Scientific X-series instrument, following Yokoyama et al. (2016).

For isotopic analyses, the analytical procedures for chemical separation followed the methods used in Pin et al. (1994) and Noguchi et al. (2011) for Sr, Pin et al. (1994) and Pin and Zalduegui (1997) for Nd, and Kuritani and Nakamura (2002) for Pb. Isotopic ratios were determined using a multicollector (MC)–ICP–MS (Neptune plus, Thermo Fisher Scientific). Mass fractionation factors for Sr and Nd were internally corrected using $^{86}Sr/^{88}Sr = 0.1194$ and $^{146}Nd/^{144}Nd = 0.7219$, respectively, and those for Pb were corrected using Tl as an external standard. Additional corrections were performed by applying a standard bracketing method using NIST987, JNdi-1, and NIST981 for Sr, Nd, and Pb isotopic analyses, respectively, and

normalizing to $^{87}Sr/^{86}Sr$ = 0.710214 for NIST 987, $^{143}Nd/^{144}Nd$ = 0.512117 for JNdi-1, and $^{206}Pb/^{204}Pb$ = 16.9424, $^{207}Pb/^{204}Pb$ = 15.5003, and $^{208}Pb/^{204}Pb$ = 36.7266 for NIST981 (Kuritani and Nakamura, 2003). The isotopic ratios of the Geological Survey of Japan (GSJ) standard material JB-3, measured during the course of this study, were $^{87}Sr/^{86}Sr$ = 0.703384 ± 24 (n = 32, 2σ), $^{143}Nd/^{144}Nd$ = 0.513065 ± 11 (n = 23, σ), and $^{206}Pb/^{204}Pb$ = 18.2966 ± 13, $^{207}Pb/^{204}Pb$ = 15.5393 ± 16, and $^{208}Pb/^{204}Pb$ = 38.2551 ± 45 (n = 21, 2σ).

Mineral compositions were determined using a JEOL JXA-8800 electron microprobe at Hokkaido University. For mafic minerals, an accelerating voltage of 15 kV, a beam current of 20 nA, a counting time of 20 s, and a beam diameter of 10 μ m were adopted. Operating conditions for plagioclase were an accelerating voltage of 15 kV, a beam current of 10 nA, a counting time of 10 s, and a beam diameter of 10 μ m. Both oxide and natural mineral standards were used, and data were obtained using the ZAF correction method.

3-4. Petrography and mineral chemistry

All the samples are fresh with LOI <~1 wt.%, and are free from alteration. The phenocryst assemblage of the calc-alkaline andesites is olivine, clinopyroxene, orthopyroxene, and plagioclase (Fig. 3-1a). Phenocryst volumes of the andesites range from 23–50 vol.%, being typically 30–40 vol.%. The phenocrysts occasionally form crystal aggregates (Fig. 3-1a). The olivine phenocrysts frequently contain chromium spinel inclusions (Fig. 3-1b) and have suhedral to anhedral outlines (Figs. 3-1c and 3-1d). All olivine phenocrysts have a reaction rim of orthopyroxene with or without clinopyroxene. Symplectites including opaque minerals develop around the boundary between the olivine phenocrysts and the reaction rim of orthopyroxene (Figs. 3-1c and 3-1d). The clinopyroxene and orthopyroxene phenocrysts have euhedral to anhedral shapes. The plagioclase phenocrysts are euhedral to subhedral, and they usually have sieve texture (Fig. 3-1e). Gabbroic, noritic, and pyroxenite xenoliths, as well as amphibole xenocrysts, are also found in the andesites.

The chemical compositions of clinopyroxene, orthopyroxene, and plagioclase phenocrysts are shown in Fig. 3-2. Almost all phenocrysts are chemically zoned with variable core compositions. The forsterite (Fo = 100 ×Mg/(Mg+Fe)) and Ni contents of the cores of the olivine phenocrysts range from 71–89 and 0.08–0.38 wt.%, respectively. The Mg# [100 ×Mg/(Mg+Fe)] of the cores of the clinopyroxene and orthopyroxene phenocrysts range from 69–86 and 68–84, respectively. Some phenocrysts show reverse zoning, and others show normal zoning. The An# [100 ×Ca/(Ca+Na)] of the cores of the plagioclase phenocrysts (Figs. 3-2f–2-2h) range from 43–88. The distribution of the An# is highly variable with a peak at around An# =50–60 in each sample. The phenocrysts can be largely divided into those with a high-An# core (An# >~80; Fig. 3-1f), those with a relatively low-An# core (An# <~60; Fig. 3-1g), and those with cores that have intermediate An# values (Fig. 3-1h).
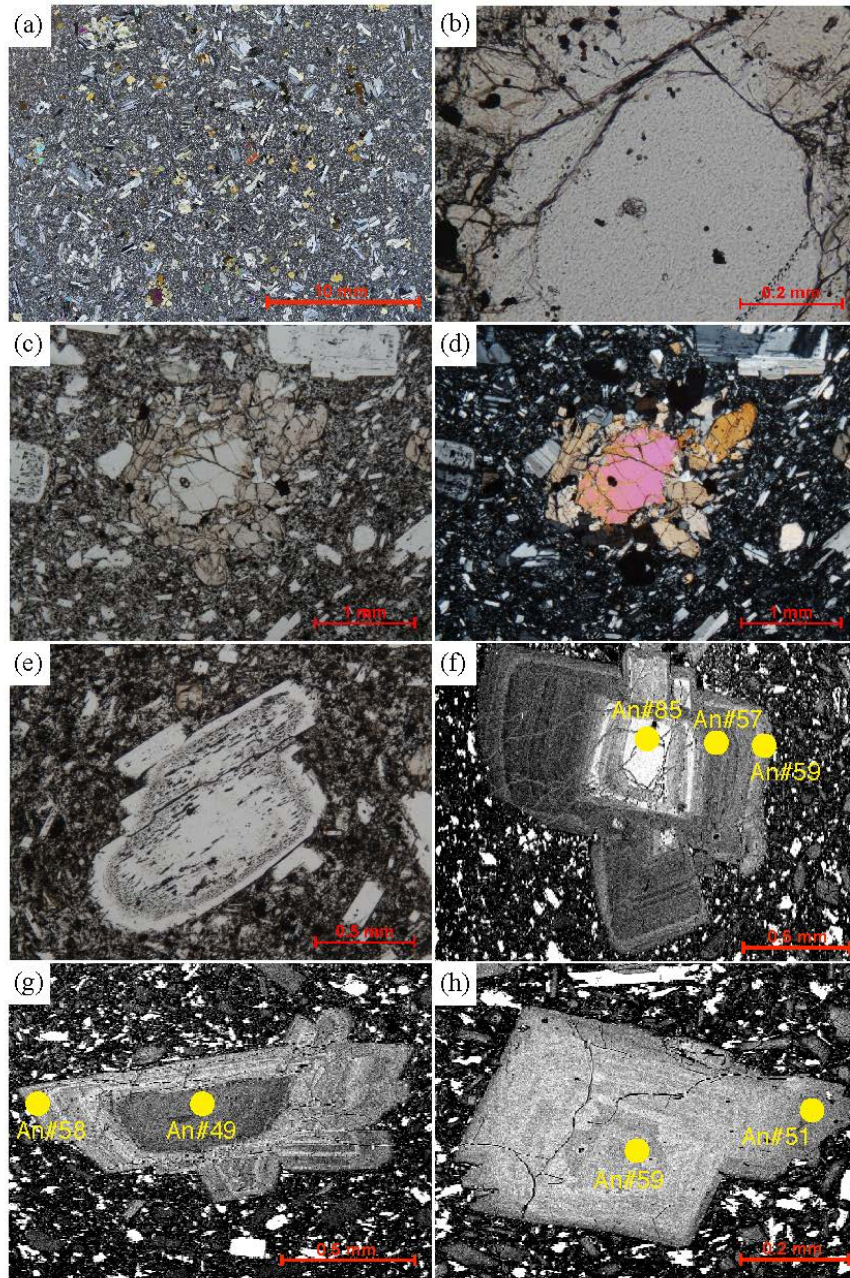
Figure 3-1 Photomicrographs of (a) representative calc-alkaline andesite sample (YM-11; cross-polarized light), (b) olivine phenocrysts with chromium spinel inclusions (YM-11, Ol-1; parallel-polarized light), (c, d) high-Fo olivine phenocryst that has a reaction rim of pyroxenes (YM-11, Ol-3; parallel- and cross-polarized light, respectively), (e) a sieve textured plagioclase phenocryst (YM-11, Pl-105; parallel-polarized light), and back-scattered electron images of (f) a plagioclase phenocryst with a high-An# core (YM-11, Pl-100), (g) a plagioclase phenocryst with a low-An# core (YM-11, Pl-103), and (h) a plagioclase phenocryst with an intermediate An# core (YM-11, Pl-43).
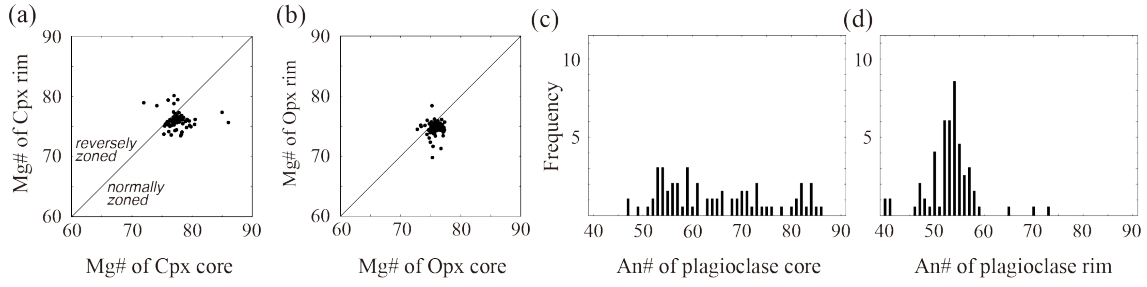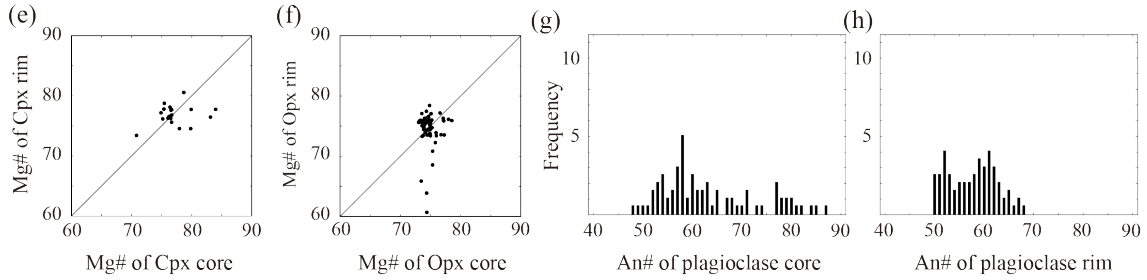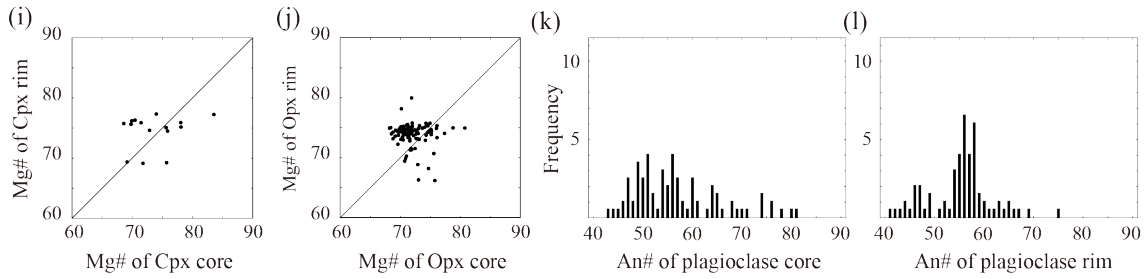
Figure 3-2 Core compositions of clinopyroxene (a, e, i) and orthopyroxene (b, f, j) phenocrysts and histograms for An# contents of cores (c, g, k) and rims (d, h, l) of plagioclase phenocrysts in selected andesitic samples.

3-5. Whole-rock compositions

The whole-rock major and trace elements and Sr–Nd–Pb isotope data of the andesitic samples are presented in Table 3-1, and selected variation diagrams are shown in Figs. 3-3–3-5.

3-5-1. Major elements

SiO$_2$ variation diagrams for Na$_2$O+K$_2$O, FeO*/MgO, K$_2$O, CaO, and MgO are shown in Fig. 3-3. The SiO$_2$, Na$_2$O+K$_2$O, and K$_2$O contents of the andesites exhibit ranges of 57.9–61.9 wt.%, 5.4–5.7 wt.%, and 1.1–1.3 wt.%, respectively. The products are classified as a subalkaline on the classification scheme of Miyashiro (1978; Fig. 3-3a), a medium-K on the scheme of Peccerillo and Taylor (1976; Fig. 3-3c), and calc-alkaline on Miyashiro's diagram (Miyashiro, 1974; Fig. 3-3b). The calc-alkaline andesitic products can be distinguished from other volcanic products of Rishiri by major element compositions (Figs. 3-3a–3-3c and 3-3e). Although most of the

24

elements show relatively linear trends on Harker diagrams, e.g., CaO (Fig. 3-3d), the MgO contents show a variable range (MgO = 3.4–4.4 wt.%) at around SiO_2 = 59 wt.% (Fig. 3-3f).

3-5-2. Trace elements

Figs. 3-4a–3-4c show SiO_2 variation diagrams for Ni, Sr, and Zr. Except for Ni (Fig. 3-4a) and Cr, trace element concentrations show linear trends on Harker diagrams (e.g., Zr, Sr; Figs. 3-4b and 3-4c). The concentrations of Ni (Fig. 3-4a) and Cr are highly variable at relatively lower SiO_2 contents. Although some dacitic products that erupted after the andesitic magmas show adakitic signatures (e.g., high-Sr/Y; Defant and Drummond, 1990), calc-alkaline andesitic magmas plot around the boundary of the adakite field (Fig. 3-4d). Some incompatible trace element ratios (e.g., Zr/Yb; Fig. 3-4e) change systematically with SiO_2 content. Primitive mantle-normalized trace element and rare-earth element concentrations are shown in Figs. 3-5a and 3-5b, respectively. The trace element concentrations have a subduction zone signature, with negative anomalies of Nb and Ta and positive spikes of Sr (Fig. 3-5a). The calc-alkaline andesites have relatively high light rare earth element concentrations and low middle to heavy rare earth element concentrations compared with those of basaltic magmas from Rishiri. Weak negative Eu anomalies are observed in the andesitic samples (Fig. 3-5b).

3-5-3. Radiogenic isotopes

The variations of $^{87}Sr/^{86}Sr$ and $^{206}Pb/^{204}Pb$ ratios with SiO_2 content are shown in Figs. 3-6a and 3-6b, respectively. With increasing SiO_2 content, $^{87}Sr/^{86}Sr$ ratios do not change significantly (Fig. 3-6a), whereas $^{206}Pb/^{204}Pb$ ratios tend to increase (Fig. 3-6b). The $^{87}Sr/^{86}Sr$ and $^{143}Nd/^{144}Nd$ ratios of the calc-alkaline andesites are more enriched than those of basalts from the volcano (Figs. 3-6c and 3-6d). The $^{206}Pb/^{204}Pb$ and $^{208}Pb/^{204}Pb$ ratios of the calc-alkaline andesites are significantly higher than those of basalts from Rishiri (Figs. 3-6e and 3-6f).

Table 3-1 Results of elemental and isotopic analyses for the calc-alkaline andesite lavas from the Rishiri Volcano.

No.	1	2	3	4	5	6	7	8	9	10
Sample	AF-7	AF-8	AF-9	AF-10	AF-21	AF-22	AF-23	AF-206	AF-207u	AF-207l
Latitude (°N)	45°10'54"	45°10'54"	45°10'52"	45°10'44"	Boulder	Boulder	Boulder	45°10'56"	45°10'56"	45°10'56"
Longitude (°E)	141°16'21"	141°16'27"	141°16'45"	141°16'53"	Boulder	Boulder	Boulder	141°16'14"	141°16'14"	141°16'14"
Major elements (wt. %)										
SiO_2	58.63	57.75	57.38	59.69	59.41	59.27	58.45	58.51	60.12	59.35
TiO_2	0.85	0.84	0.85	0.81	0.82	0.82	0.86	0.87	0.79	0.82
Al_2O_3	17.95	17.80	17.61	18.20	17.82	17.78	17.78	18.15	17.36	17.89
Fe_2O_3*	6.62	6.57	6.69	5.87	6.36	6.37	6.76	6.79	6.20	6.52
MnO	0.13	0.13	0.13	0.11	0.12	0.12	0.13	0.13	0.12	0.12
MgO	3.75	3.61	3.73	3.34	3.50	3.44	3.79	3.72	3.83	3.42
CaO	6.73	6.84	6.82	6.63	6.53	6.51	6.76	6.88	6.26	6.60
Na_2O	4.36	4.40	4.36	4.30	4.38	4.39	4.35	4.46	4.28	4.45
K_2O	1.15	1.18	1.17	1.23	1.19	1.19	1.15	1.18	1.25	1.21
P_2O_5	0.30	0.31	0.31	0.28	0.30	0.30	0.31	0.31	0.28	0.30
total	100.46	99.43	99.05	100.47	101.34	101.10	101.24	101.00	100.48	100.70
LOI	0.30	-1.39	0.17	0.15	0.10	0.14	0.34	2.50	0.58	0.29
Trace elements (ppm)										
Sc (XRF)	17.88	15.67	16.29	16.91	15.99	14.72	15.54	18.71	15.19	17.97
V (XRF)	128.48	127.50	130.83	120.42	123.20	121.48	130.20	129.73	119.47	120.31
Cr (XRF)	47.95	41.12	49.59	47.56	42.20	39.59	49.98	46.73	81.79	41.61
Co (XRF)	22.85	22.42	23.21	21.54	21.04	21.46	22.41	23.60	22.09	21.71
Ni (XRF)	30.00	28.06	32.25	35.83	29.14	28.27	30.80	28.98	48.74	27.33
Rb	25.75	24.78	25.75							
Sr	585.5	577.9	586.8							
Y	19.40	18.20	19.77							
Zr	162.8	161.6	160.3							
Nb	6.59	6.57	6.55							
Cs	0.46	0.91	0.59							
Ba	310.9	292.7	293.0							
La	18.19	18.20	18.82							
Ce	45.05	45.19	43.38							
Pr	4.62	4.72	4.75							
Nd	18.86	19.32	19.39							
Sm	3.98	4.02	4.07							
Eu	1.27	1.25	1.30							
Gd	4.04	4.03	4.15							
Tb	0.60	0.61	0.62							
Dy	3.71	3.75	3.78							
Ho	0.76	0.76	0.77							
Er	2.24	2.26	2.29							
Tm	0.33	0.33	0.34							
Yb	2.23	2.24	2.28							
Lu	0.34	0.34	0.35							
Hf	3.57	3.64	3.62							
Ta	0.46	0.46	0.46							
Pb	3.13	4.38	4.02							
Th	2.93	2.42	2.97							
U	0.82	0.83	0.83							
Isotopes										
$^{87}Sr/^{86}Sr$	0.703279	0.703252	0.703303							
2SE	0.000021	0.000016	0.000013							
$^{143}Nd/^{144}Nd$	0.512940		0.512942							
2SE	0.000015		0.000012							
$^{206}Pb/^{204}Pb$	18.4654	18.4674	18.4680	18.4912						
2SE	0.0005	0.0007	0.0006	0.0006						
$^{207}Pb/^{204}Pb$	15.5459	15.5478	15.5483	15.5500						
2SE	0.0005	0.0006	0.0005	0.0005						
$^{208}Pb/^{204}Pb$	38.3537	38.3595	38.3618	38.3791						
2SE	0.0015	0.0018	0.0016	0.0013						

*total Fe given as Fe_2O_3. Errors on isotope ratios are within-run 2 SE.

Table 3-1 Continued.

No.	11	12	13	14	15	16	17	18	19	20
Sample	YM-3-b	YM-9	YM-10	YM-11	YM-12	YM-14	YM-15	YM-17	YM-101	YM-206
Latitude (°N)	Boulder	45°09'55"	45°09'50"	45°09'47"	45°09'46"	45°09'45"	45°09'45"	45°09'43"	Boulder	45°10'49"
Longitude (°E)	Boulder	141°15'29"	141°15'36"	141°15'46"	141°15'48"	141°15'60"	141°16'06"	141°15'52"	Boulder	141°15'41"

Major elements (wt. %)

SiO_2	58.49	58.86	59.26	59.25	59.76	59.38	58.88	59.81	60.11	60.12
TiO_2	0.84	0.82	0.81	0.79	0.77	0.79	0.79	0.76	0.81	0.79
Al_2O_3	18.06	17.77	17.36	17.37	17.48	17.59	17.59	17.46	17.38	17.65
Fe_2O_3*	6.42	6.28	6.15	6.14	5.90	5.94	5.98	5.86	6.16	6.12
MnO	0.12	0.12	0.12	0.12	0.11	0.11	0.11	0.11	0.12	0.12
MgO	3.42	3.44	3.60	3.68	3.46	3.48	3.49	3.46	3.71	3.33
CaO	6.84	6.54	6.43	6.53	6.35	6.44	6.50	6.47	6.36	6.44
Na_2O	4.39	4.38	4.31	4.27	4.32	4.30	4.33	4.25	4.31	4.37
K_2O	1.21	1.22	1.25	1.21	1.22	1.21	1.24	1.25	1.25	1.21
P_2O_5	0.31	0.31	0.29	0.28	0.28	0.28	0.28	0.27	0.29	0.29
total	100.11	99.74	100.46	99.63	99.65	99.52	99.20	99.71	101.39	100.42
LOI	0.97	0.73	0.16	0.26	0.36	0.28	0.32	0.34	0.19	1.27

Trace elements (ppm)

Sc (XRF)	14.43	15.63	17.93	15.83	14.89	14.63	14.95	15.28	17.61	15.35
V (XRF)	122.91	114.48	122.06	120.73	112.92	114.26	119.67	115.91	122.87	116.65
Cr (XRF)	40.43	39.43	66.00	65.28	57.68	58.59	60.68	53.55	63.55	49.05
Co (XRF)	21.27	21.52	21.10	21.58	20.60	20.51	21.65	21.70	22.06	20.27
Ni (XRF)	25.97	28.57	43.24	42.44	39.48	38.63	43.63	39.31	41.93	31.88
Rb		27.25		27.36			24.02	27.93		
Sr		573.6		539.2			563.5	535.9		
Y		18.78		18.30			17.09	16.58		
Zr		168.3		165.6			168.3	166.5		
Nb		6.79		6.72			6.79	6.68		
Cs		1.30		0.64			0.64	1.40		
Ba		300.3		302.9			308.9	311.7		
La		19.34		19.40			18.90	19.11		
Ce		43.96		42.28			43.78	42.68		
Pr		4.73		4.59			4.54	4.51		
Nd		19.06		18.35			18.20	17.84		
Sm		3.93		3.79			3.78	3.69		
Eu		1.24		1.20			1.19	1.15		
Gd		3.95		3.85			3.83	3.71		
Tb		0.59		0.57			0.56	0.55		
Dy		3.60		3.52			3.47	3.37		
Ho		0.74		0.71			0.71	0.69		
Er		2.18		2.13			2.12	2.05		
Tm		0.32		0.32			0.31	0.30		
Yb		2.19		2.14			2.10	2.03		
Lu		0.34		0.33			0.32	0.31		
Hf		3.72		3.69			3.73	3.72		
Ta		0.49		0.50			0.50	0.51		
Pb		4.52		4.53			4.26	4.75		
Th		3.18		3.34			2.82	3.06		
U		0.88		0.94			0.95	0.99		

Isotopes

$^{87}Sr/^{86}Sr$		0.703259		0.703305			0.703278			
2SE		0.000021		0.000021			0.000019			
$^{143}Nd/^{144}Nd$		0.512930		0.512935			0.512941			
2SE		0.000010		0.000009			0.000012			
$^{206}Pb/^{204}Pb$		18.4734		18.4935		18.4917	18.4909			
2SE		0.0004		0.0006		0.0006	0.0008			
$^{207}Pb/^{204}Pb$		15.5490		15.5522		15.5507	15.5504			
2SE		0.0004		0.0005		0.0006	0.0007			
$^{208}Pb/^{204}Pb$		38.3677		38.3857		38.3814	38.3800			
2SE		0.0013		0.0013		0.0015	0.0018			

*total Fe given as Fe_2O_3. Errors on isotope ratios are within-run 2 SE.

Table 3-1 Continued.

No.	21	22	23	24	25	26	27	28	29	30
Sample	KT-1	KT-2	KT-3	KT-4	KT-5	KT-6	KT-7	KT-8	KT-9	KT-10
Latitude (°N)	45°10'51"	45°10'50"	45°10'49"	45°10'49"	45°10'48"	45°10'48"	45°10'50"	45°10'52"	45°10'53"	45°10'54"
Longitude (°E)	141°14'10"	141°14'06"	141°14'02"	141°14'02"	141°14'00"	141°13'59"	141°13'55"	141°13'51"	141°13'46"	141°13'42"
Major elements (wt. %)										
SiO_2	59.36	59.78	59.80	59.34	59.40	59.06	59.48	58.95	59.93	59.62
TiO_2	0.82	0.80	0.80	0.80	0.79	0.81	0.80	0.80	0.80	0.80
Al_2O_3	17.38	17.54	17.73	17.62	17.61	17.37	17.62	17.43	17.67	17.63
Fe_2O_3*	6.19	6.20	6.13	6.11	6.03	6.22	6.14	6.07	6.10	6.17
MnO	0.12	0.12	0.12	0.12	0.11	0.12	0.12	0.12	0.12	0.12
MgO	3.56	3.68	3.55	3.42	3.45	3.58	3.51	3.46	3.50	3.57
CaO	6.40	6.40	6.49	6.44	6.52	6.46	6.29	6.48	6.27	6.41
Na_2O	4.32	4.30	4.33	4.35	4.32	4.28	4.31	4.28	4.31	4.28
K_2O	1.19	1.15	1.16	1.16	1.17	1.19	1.19	1.19	1.17	1.18
P_2O_5	0.28	0.25	0.28	0.27	0.27	0.28	0.13	0.28	0.26	0.28
total	99.61	100.22	101.27	99.62	99.67	99.37	99.58	99.07	100.13	100.06
LOI	0.15	0.26	0.36	0.36	0.36	0.85	0.98	0.72	0.38	0.86
Trace elements (ppm)										
Sc (XRF)	16.36	15.36	16.41	14.47	16.26	15.44	16.51	14.08	14.59	14.10
V (XRF)	114.98	114.67	117.16	118.87	113.46	113.56	116.81	111.16	116.06	116.45
Cr (XRF)	53.19	55.83	51.90	44.38	50.87	49.83	48.77	54.14	46.14	53.16
Co (XRF)	20.63	21.00	21.66	21.73	22.20	21.77	22.32	19.48	21.09	22.56
Ni (XRF)	34.22	35.59	35.30	32.61	32.97	35.50	35.62	34.07	34.26	35.39
Rb	25.63			24.27					27.00	
Sr	550.4			536.8					556.8	
Y	17.84			16.79					18.24	
Zr	170.1			162.5					169.4	
Nb	6.83			6.59					6.87	
Cs	0.52			0.53					1.11	
Ba	300.6			288.2					294.3	
La	18.21			17.80					18.65	
Ce	45.06			42.67					40.74	
Pr	4.49			4.30					4.48	
Nd	18.05			17.29					18.00	
Sm	3.76			3.59					3.71	
Eu	1.19			1.16					1.19	
Gd	3.81			3.63					3.81	
Tb	0.57			0.54					0.56	
Dy	3.50			3.36					3.46	
Ho	0.72			0.69					0.71	
Er	2.14			2.04					2.11	
Tm	0.31			0.30					0.31	
Yb	2.15			2.06					2.13	
Lu	0.33			0.32					0.33	
Hf	3.79			3.62					3.73	
Ta	0.50			0.49					0.50	
Pb	4.48			3.92					4.60	
Th	2.99			2.76					3.16	
U	0.90			0.85					0.88	
Isotopes										
$^{87}Sr/^{86}Sr$	0.703300			0.703269					0.703316	
2SE	0.000014			0.000018					0.000030	
$^{143}Nd/^{144}Nd$	0.512935			0.512942					0.512935	
2SE	0.000009			0.000008					0.000009	
$^{206}Pb/^{204}Pb$	18.4838	18.4822					18.4848		18.4852	
2SE	0.0007	0.0005					0.0004		0.0005	
$^{207}Pb/^{204}Pb$	15.5519	15.5511					15.5517		15.5523	
2SE	0.0006	0.0005					0.0005		0.0005	
$^{208}Pb/^{204}Pb$	38.3787	38.3755					38.3785		38.3809	
2SE	0.0016	0.0013					0.0012		0.0012	

*total Fe given as Fe_2O_3. Errors on isotope ratios are within-run 2 SE.

Table 3-1 Continued.

No.	31	32	33	34	35	36	37	38	39	40
Sample	KT-11	KT-12	KT-13	KT-14	KT-15	KT-16	KT-17	KT-22	KT-23	KT-24
Latitude (°N)	45°10'57"	45°10'58"	45°10'60"	45°11'02"	45°11'02"	45°11'59"	45°11'03"	45°11'02"	45°11'02"	45°11'02"
Longitude (°E)	141°13'38"	141°13'35"	141°13'30"	141°13'23"	141°13'11"	141°13'02"	141°12'48"	141°13'22"	141°13'20"	141°13'18"

Major elements (wt. %)

SiO_2	59.63	59.71	58.99	58.99	61.65	60.17	60.17	59.47	60.26	60.95
TiO_2	0.79	0.80	0.80	0.80	0.73	0.77	0.76	0.86	0.79	0.77
Al_2O_3	17.56	17.91	17.61	17.23	17.46	17.61	17.73	17.64	17.45	17.67
Fe_2O_3*	6.18	6.01	6.21	6.23	5.50	5.92	5.79	6.29	5.98	5.90
MnO	0.12	0.12	0.12	0.12	0.10	0.11	0.11	0.12	0.12	0.11
MgO	3.68	3.48	3.63	3.64	3.03	3.50	3.35	3.66	3.52	3.23
CaO	6.54	6.51	6.57	6.52	5.91	6.26	6.49	6.42	6.20	6.05
Na_2O	4.26	4.26	4.32	4.22	4.28	4.27	4.25	4.25	4.21	4.35
K_2O	1.14	1.16	1.14	1.19	1.28	1.25	1.23	1.29	1.27	1.21
P_2O_5	0.28	0.22	0.28	0.28	0.26	0.24	0.27	0.30	0.28	0.23
total	100.19	100.18	100.56	99.22	100.20	100.98	101.04	101.20	100.95	101.34
LOI	0.36	0.87	0.26	0.80	1.09	0.64	0.80	1.00	1.01	0.35

Trace elements (ppm)

Sc (XRF)	16.18	14.19	14.84	15.88	15.85	14.31	16.05	18.25	16.29	14.79
V (XRF)	117.20	116.91	117.93	117.06	103.28	129.34	111.04	129.80	118.44	108.33
Cr (XRF)	57.29	52.11	59.77	58.52	40.01	53.64	58.10	56.08	55.41	44.16
Co (XRF)	22.11	21.97	22.43	22.08	19.51	20.95	19.29	21.05	20.88	19.08
Ni (XRF)	36.65	34.44	37.43	36.98	30.82	38.58	36.92	39.20	39.98	30.65
Rb									28.19	
Sr									512.8	
Y									17.79	
Zr									172.1	
Nb									6.90	
Cs									1.40	
Ba									313.0	
La									19.78	
Ce									45.75	
Pr									4.65	
Nd									18.51	
Sm									3.81	
Eu									1.19	
Gd									3.82	
Tb									0.57	
Dy									3.50	
Ho									0.71	
Er									2.12	
Tm									0.31	
Yb									2.13	
Lu									0.33	
Hf									3.84	
Ta									0.52	
Pb									4.91	
Th									3.54	
U									1.03	

Isotopes

$^{87}Sr/^{86}Sr$			0.703263				0.703287		0.703276	
2SE			0.000022				0.000016		0.000014	
$^{143}Nd/^{144}Nd$			0.512949				0.512958		0.512939	
2SE			0.000013				0.000007		0.000008	
$^{206}Pb/^{204}Pb$	18.4843		18.4831		18.5009		18.4975			
2SE	0.0006		0.0005		0.0011		0.0009			
$^{207}Pb/^{204}Pb$	15.5519		15.5513		15.5517		15.5515			
2SE	0.0006		0.0004		0.0009		0.0009			
$^{208}Pb/^{204}Pb$	38.3787		38.3768		38.3807		38.3843			
2SE	0.0013		0.0012		0.0024		0.0023			

*total Fe given as Fe_2O_3. Errors on isotope ratios are within-run 2 SE.

Table 3-1 Continued.

No.	41	42	43	44	45	46	47	48	49	50
Sample	KT-26	KT-27	KT-28	KT-31	KT-32	KT-33	TAK-1	TAK-2	TAK-3	TAK-4
Latitude (°N)	45°11'02"	45°11'02"	45°11'02"	45°11'59"	45°11'02"	45°11'03"	45°09'20"	45°09'21"	45°09'15"	45°09'13"
Longitude (°E)	141°13'13"	141°13'11"	141°13'07"	141°13'03"	141°12'52"	141°12'48"	141°17'11"	141°17'16"	141°17'33"	141°17'35"
Major elements (wt. %)										
SiO_2	60.52	61.71	61.25	60.61	60.63	60.42	58.28	58.87	59.24	59.80
TiO_2	0.71	0.71	0.75	0.78	0.79	0.78	0.82	0.82	0.81	0.83
Al_2O_3	17.23	17.74	17.22	17.64	17.64	17.65	17.37	17.18	17.36	17.32
Fe_2O_3*	5.57	5.37	5.89	5.78	5.78	5.75	6.69	6.72	6.59	6.66
MnO	0.11	0.10	0.11	0.11	0.11	0.11	0.13	0.13	0.13	0.13
MgO	3.06	2.84	3.52	3.17	3.11	3.16	4.32	4.14	4.06	4.37
CaO	6.09	5.99	6.11	6.16	6.12	6.21	6.68	6.52	6.52	6.57
Na_2O	4.34	4.35	4.26	4.35	4.37	4.27	4.24	4.26	4.32	4.23
K_2O	1.26	1.26	1.24	1.30	1.31	1.29	1.23	1.26	1.26	1.23
P_2O_5	0.26	0.25	0.24	0.28	0.28	0.28	0.30	0.30	0.30	0.30
total	100.03	101.20	101.49	101.05	101.03	100.80	100.05	100.20	100.59	101.43
LOI	0.61	0.87	0.73	0.33	0.44	0.87	0.99	1.17	0.36	0.94
Trace elements (ppm)										
Sc (XRF)	15.16	13.64	17.72	16.59	13.58	14.26	16.92	15.93	16.61	16.85
V (XRF)	106.04	106.14	112.94	117.02	112.97	112.45	122.60	122.54	119.60	125.25
Cr (XRF)	41.52	35.80	54.80	46.03	43.37	45.04	100.56	81.43	73.46	87.78
Co (XRF)	19.32	19.52	19.82	19.37	19.46	19.46	24.37	23.50	22.80	23.50
Ni (XRF)	31.02	29.50	39.49	34.79	34.19	34.53	56.34	49.01	49.43	52.46
Rb	27.14					30.02				
Sr	521.4					528.5				
Y	16.98					18.01				
Zr	176.8					172.8				
Nb	7.03					6.93				
Cs	1.30					1.47				
Ba	320.5					323.1				
La	20.35					20.30				
Ce	45.99					43.41				
Pr	4.52					4.70				
Nd	17.66					18.64				
Sm	3.58					3.83				
Eu	1.12					1.20				
Gd	3.62					3.85				
Tb	0.53					0.56				
Dy	3.29					3.48				
Ho	0.68					0.71				
Er	2.01					2.11				
Tm	0.30					0.31				
Yb	2.01					2.09				
Lu	0.31					0.33				
Hf	3.94					3.87				
Ta	0.55					0.53				
Pb	5.08					4.94				
Th	3.72					3.76				
U	1.09					1.04				
Isotopes										
$^{87}Sr/^{86}Sr$	0.703316					0.703283				
2SE	0.000019					0.000019				
$^{143}Nd/^{144}Nd$	0.512935					0.512928				
2SE	0.000009					0.000008				
$^{206}Pb/^{204}Pb$	18.5010					18.4998				
2SE	0.0008					0.0006				
$^{207}Pb/^{204}Pb$	15.5527					15.5531				
2SE	0.0008					0.0006				
$^{208}Pb/^{204}Pb$	38.3870					38.3938				
2SE	0.0021					0.0017				

*total Fe given as Fe_2O_3. Errors on isotope ratios are within-run 2 SE.

30

Table 3-1 Continued.

| No.	51	52	53	54	55	56	57	58
Sample	TAK-5	TAK-6	Xe-11-M	Xe-16-M	Xe-21-M	Xe-36-M	Xe-37-M	Xe-36-X
Latitude (°N)	45°09'09"	45°09'07"	Boulder	Boulder	Boulder	Boulder	Boulder	Boulder
Longitude (°E)	141°17'40"	141°17'41"	Boulder	Boulder	Boulder	Boulder	Boulder	Boulder
Major elements (wt. %)								
SiO_2	59.13	58.35	59.38	57.87	59.22	57.66	58.71	58.39
TiO_2	0.85	0.84	0.81	0.87	0.81	0.90	0.85	0.87
Al_2O_3	17.22	17.36	17.94	17.84	17.57	18.02	17.73	17.56
Fe_2O_3*	6.80	6.69	6.35	6.73	6.45	6.83	6.37	6.46
MnO	0.13	0.13	0.12	0.13	0.12	0.13	0.12	0.12
MgO	4.29	4.15	3.42	3.74	3.58	3.78	3.72	3.80
CaO	6.71	6.76	6.62	7.01	6.43	7.06	6.75	6.66
Na_2O	4.26	4.24	4.34	4.41	4.30	4.36	4.32	4.28
K_2O	1.25	1.24	1.15	1.17	1.26	1.18	1.19	1.18
P_2O_5	0.30	0.30	0.30	0.32	0.31	0.34	0.30	0.31
total	100.93	100.08	101.33	100.98	100.96	101.16	100.96	100.53
LOI	0.39	0.83	0.53	0.04	0.52	0.40	0.77	0.75
Trace elements (ppm)								
Sc (XRF)	18.36	19.34	14.39	13.81	14.99	17.90	16.62	15.53
V (XRF)	129.43	124.74	117.69	132.04	118.93	130.99	124.38	121.85
Cr (XRF)	84.31	75.29	41.91	47.01	49.81	50.51	63.26	59.81
Co (XRF)	24.63	23.56	20.89	20.92	21.69	22.60	20.59	22.47
Ni (XRF)	48.98	47.75	26.56	28.70	34.15	28.18	37.36	39.67
Rb								
Sr								
Y								
Zr								
Nb								
Cs								
Ba								
La								
Ce								
Pr								
Nd								
Sm								
Eu								
Gd								
Tb								
Dy								
Ho								
Er								
Tm								
Yb								
Lu								
Hf								
Ta								
Pb								
Th								
U								
Isotopes								
$^{87}Sr/^{86}Sr$								
2SE								
$^{143}Nd/^{144}Nd$								
2SE								
$^{206}Pb/^{204}Pb$								
2SE								
$^{207}Pb/^{204}Pb$								
2SE								
$^{208}Pb/^{204}Pb$								
2SE								

*total Fe given as Fe_2O_3. Errors on isotope ratios are within-run 2 SE.
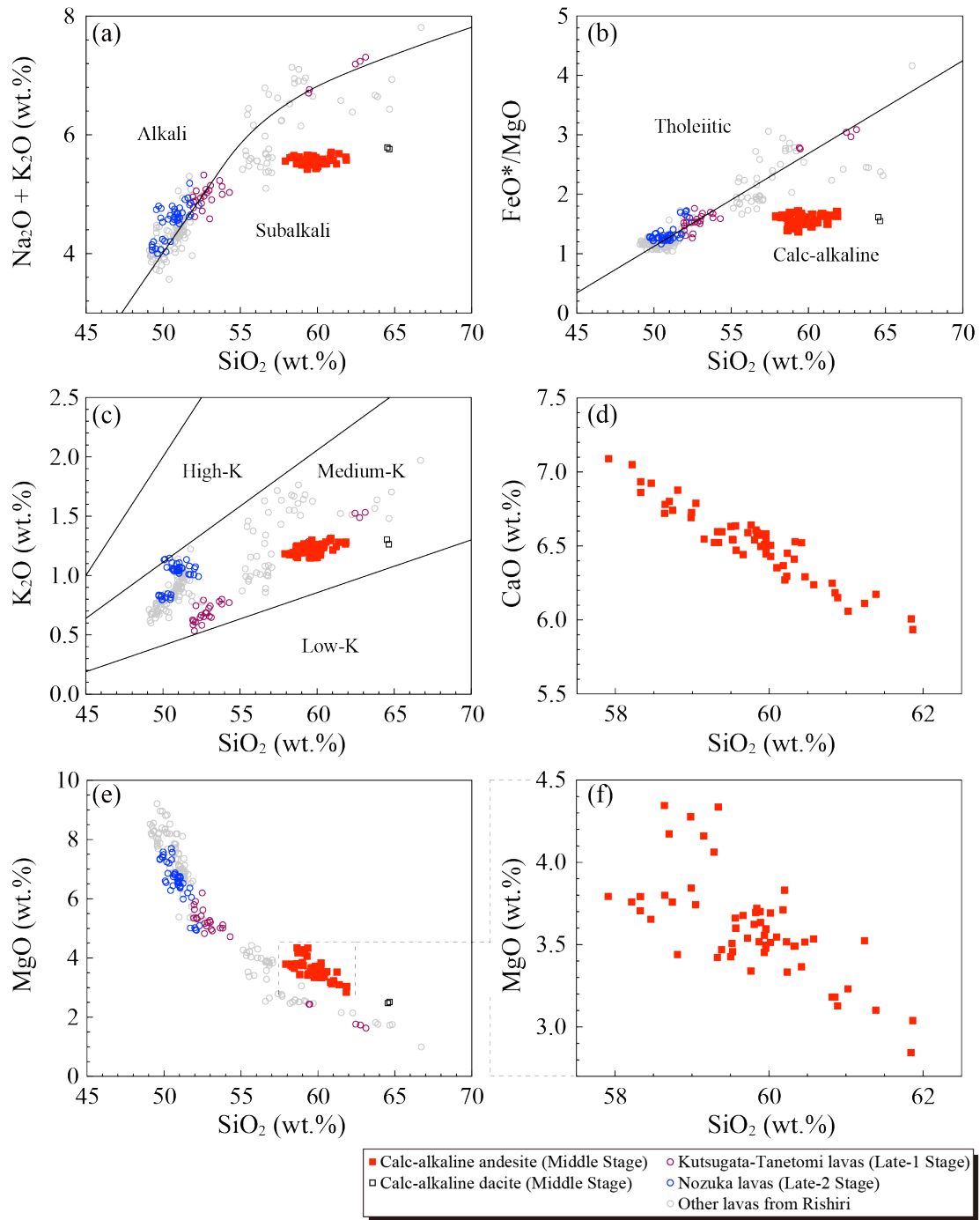
Figure 3-3 Whole-rock major element compositions of calc-alkaline andesitic products from the Rishiri Volcano shown in (a) Na_2O+K_2O–SiO_2, (b) FeO^*/MgO–SiO_2, (c) K_2O–SiO_2, (d) CaO–SiO_2, and (e, f) MgO–SiO_2 diagrams. In (a), (b), and (c), discrimination line between the alkali and sub-alkali series, the calc-alkaline and tholeiite series, and the high-K, medium-K, and low-K series, are taken from Miyashiro (1978), Miyashiro (1974), and Peccerillo and Taylor (1976), respectively. In (a)–(c), and (e), whole-rock compositions of the Middle stage calc-alkaline dacites and those of other lavas from the Rishiri of Ishizuka (2000), the Kutsugata-Tanetomi lavas from Ishizuka (2000), and the Nozuka lavas from Kuritani and Nakagawa (2016), are also shown.
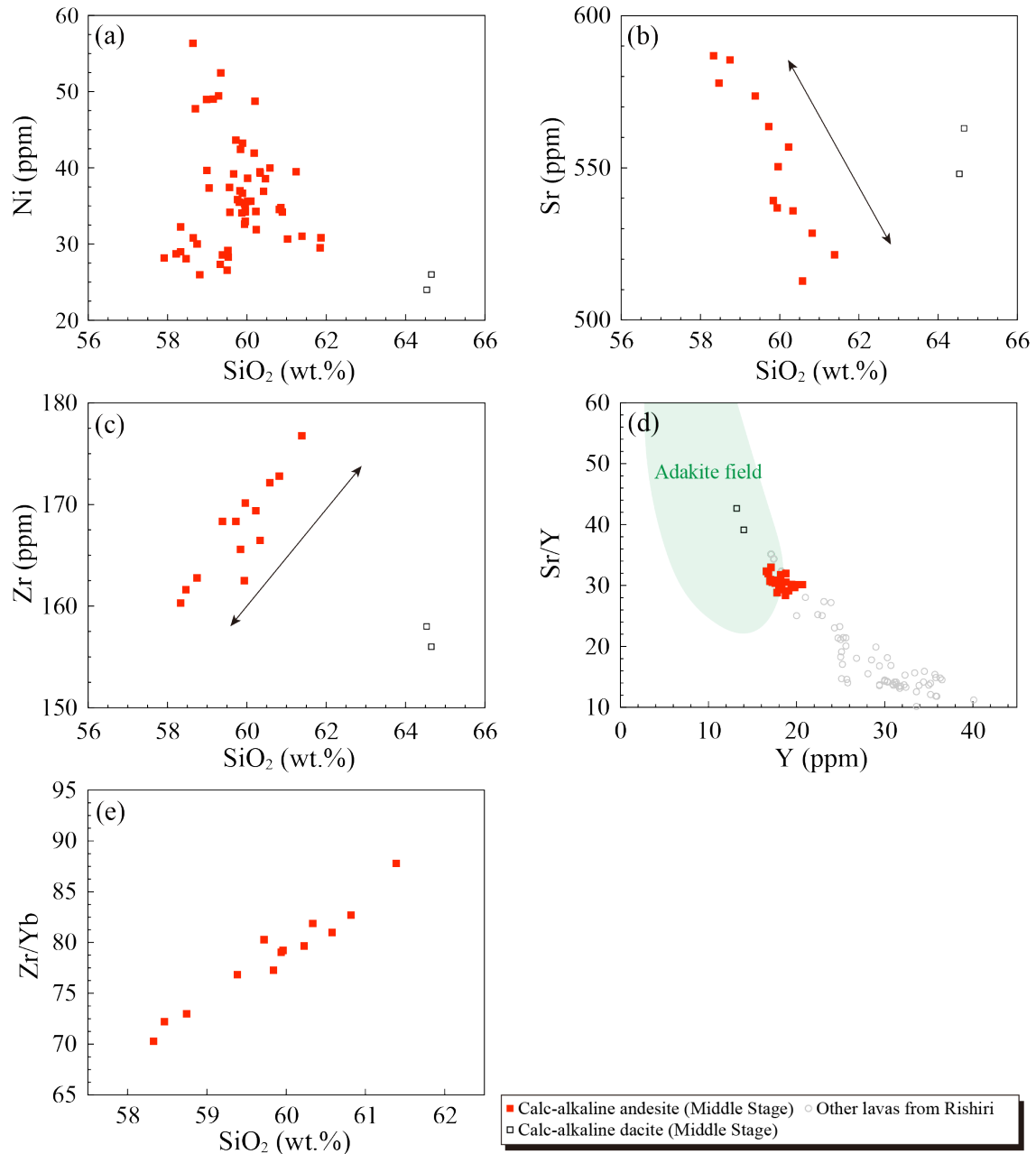
32

Figure 3-4 Trace element compositions of calc-alkaline andesitic products from the Rishiri Volcano shown in (a) Ni–SiO₂, (b) Sr–SiO₂, (c) Zr–SiO₂, (d) Sr/Y–Y, (e) Zr/Yb–SiO₂. In (a)–(d), data of Ishizuka (2000) are also shown.

3-6. Discussion

3-6-1. Magmatic processes and end-member magmas for the calc-alkaline andesite

Calc-alkaline andesitic products show the following petrological and mineralogical characteristics: (1) reaction rims composed of orthopyroxene and clinopyroxene surrounding olivine phenocrysts (Figs. 3-1c and 3-1d), (2) some plagioclase phenocrysts with remarkably high-An# cores and others with relatively low-An# cores (Figs. 3-1f and 3-1g), (3) some pyroxene
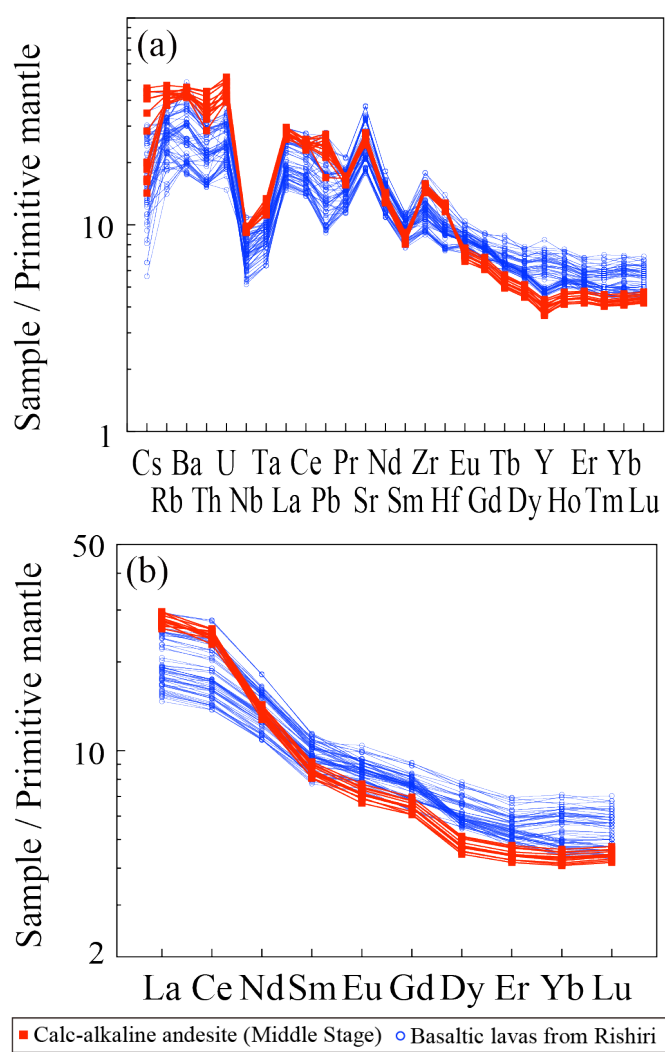
Figure 3-5 Trace element compositions of calc-alkaline andesitic products from the Rishiri Volcano shown in primitive mantle-normalized multi-element diagrams. In (a) and (b), trace element concentrations of the primitive mantle are taken from Sun and McDonough (1989). Data of Kuritani and Nakagawa (2016) and Kuritani et al. (2005, 2007, 2008) are also shown.

phenocrysts with reverse zoning, and others with normal zoning (Fig. 3-2), and (4) some olivine phenocrysts with Fo# core compositions up to 89. These observations suggest that calc-alkaline magmas were primarily generated by mixing processes between mafic and evolved magmas. The Zr/Yb ratios (Fig. 3-4e) and $^{206}Pb/^{204}Pb$ ratios (Fig. 3-6b) of the calc-alkaline andesites change significantly with SiO_2 content, suggesting that the mafic and evolved magmas did not have a parent–daughter relationship.

Most major and trace elements show linear trends in Harker diagrams, such as those observed for CaO (Fig. 3-3d), Sr (Fig. 3-4b), and Zr (Fig. 3-4c), which would be explained by binary mixing between a homogeneous mafic magma and a homogeneous felsic magmas. However, MgO (Fig. 3-3f), Ni (Fig. 3-4a) and Cr are scattered in the SiO_2 variation diagrams; this observation c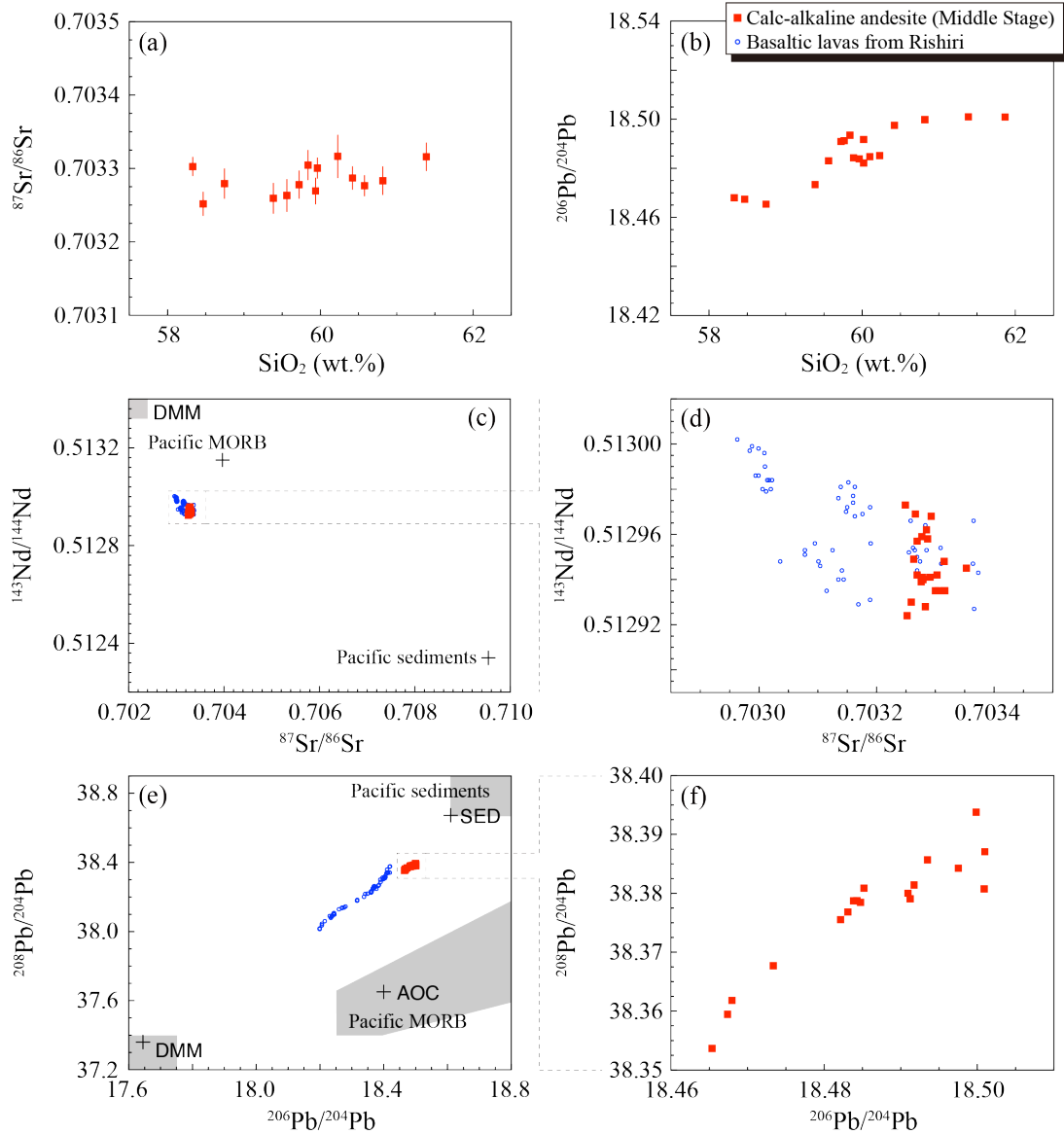annot be explained by the mixing of the two homogeneous magmas. Considering that the range of variation of MgO and Ni decreases with increasing SiO_2 in the calc-alkaline andesitic magmas (Figs. 3-3f and 3-4a), at least three end-member magmas are required: a felsic end-member magma with relatively homogeneous composition and two mafic end-member magmas, a higher-MgO primitive mafic magma and a lower-MgO evolved mafic magma (Fig. 3-7). Among the less differentiated samples (<~59 wt.% SiO_2; Fig. 3-3f), the modal abundance of olivine phenocrysts is significantly greater in the higher-MgO samples (~0.5 vol.%) than in the lower-MgO samples (~0.1 vol.%). This observation also supports the idea that the mafic magmas consist of olivine-rich primitive end-member magma and olivine-poor evolved end-member magma.

Figure 3-6 Composition of calc-alkaline andesitic products from Rishiri Volcano shown in (a) $^{87}Sr/^{86}Sr$–SiO_2, (b) $^{206}Pb/^{204}Pb$–SiO_2, (c, d) $^{143}Nd/^{144}Nd$–$^{87}Sr/^{86}Sr$, and (e, f) $^{208}Pb/^{204}Pb$–$^{206}Pb/^{204}Pb$ diagrams. In (c) and (e), compositional fields of the depleted MORB mantle (DMM) are taken from Zindler and Hart (1986), while those of Pacific MORB and sediments are from Kimura and Yoshida (2006). The representative compositions of the Pacific sediments (SED), Pacific MORB (AOC), and DMM are taken from Cousens and Allan (1992) and Hauff et al. (2006). In (c)–(e) data of Kuritani and Nakagawa (2016) and Kuritani et al. (2005, 2007, 2008) are also shown.

The compositions of the three end-member magmas are estimated using the whole-rock compositional variation and the petrographical and mineralogical features of the samples. First, the composition of the primitive end-member magma was estimated, given that the composition lies on the mixing trend between the highest- and the lowest-MgO samples in the andesites (TAK-4 and KT-27, respectively; Fig. 3-7). It is assumed that the olivine phenocryst with the highest

Fo# of 88.7 was in equilibrium with the primitive end-member magma. Then, the composition of the primitive end-member magma can be obtained (Fig. 3-7; Table 1) such that the composition of the melt on the TAk-4 –KT-27 mixing trend is in equilibrium with Fo#88.7 olivine, using the $K_D(Fe/Mg)^{olivine/melt}$ of 0.3 (Roeder and Emslie, 1970) and the $Fe^{3+}/\Sigma Fe$ of the melt of 0.25 (Kelley and Cottrell, 2009).

The composition of the felsic end-member magma was estimated using the constraint that the composition lies on the mixing trend between the highest- and the lowest-MgO samples (TAK-4 and KT-27). Because it can be considered that the felsic end-member magma was free from olivine phenocrysts, the SiO_2 content of the end-member magma can be estimated using the SiO_2 contents of TAK-4 and KT-27 (SiO_2 =59.3 and 61.8 wt.%, respectively), as well as the abundances of olivine phenocrysts in these two samples (0.51 and 0.13 vol.%, respectively), given that the abundance of the olivine phenocrysts tends to decrease linearly with SiO_2 content. Then, using the estimated SiO_2 content and the whole-rock compositional variation of the andesites, the composition of the felsic end-member magma can be obtained (Fig. 3-7; Table 3-2).
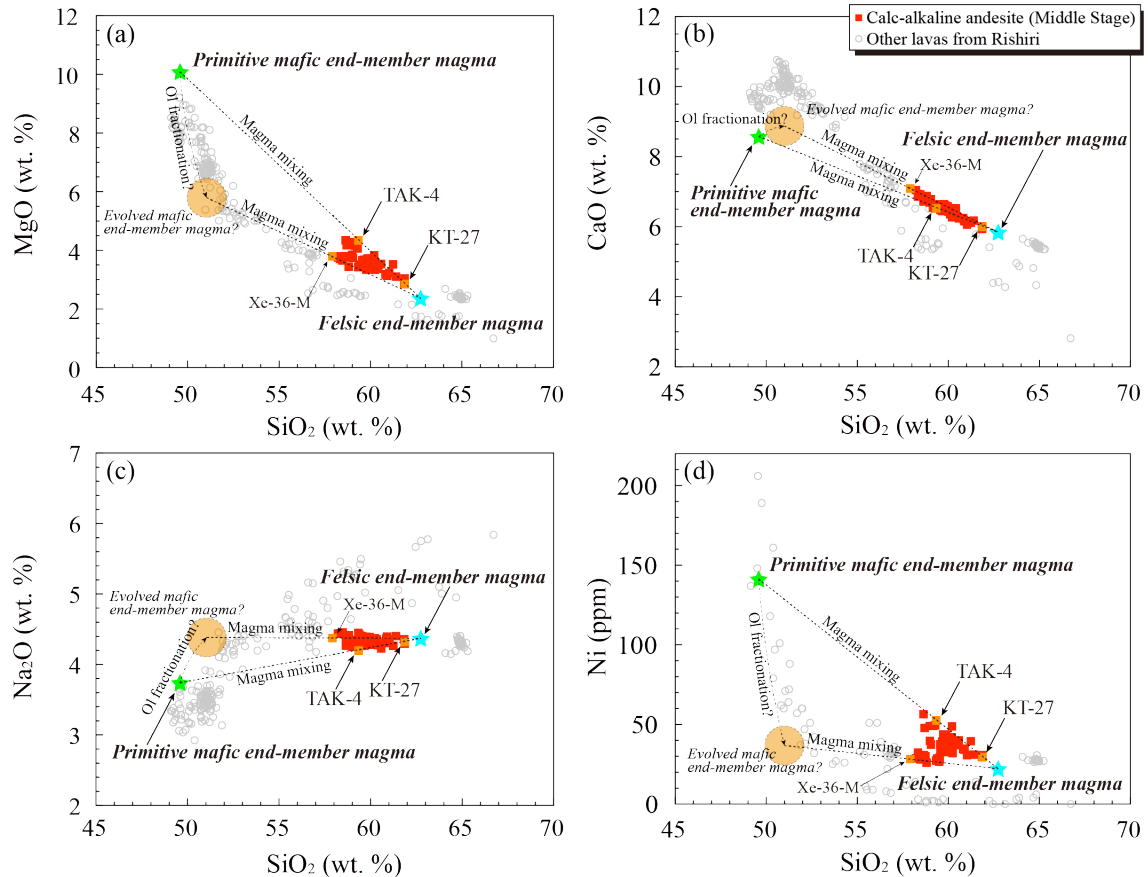

Figure 3-7 Whole-rock compositions of calc-alkaline andesite samples and those of the three possible end-member magmas for the andesitic magmas, along with possible mixing and differentiation trends, shown in (a) MgO–SiO_2, (b) CaO–SiO_2, (c) Na_2O–SiO_2, and (d) Ni–SiO_2 diagrams. Whole-rock compositions of other lavas from the Rishiri from Ishizuka (2000) and Kuritani and Nakagawa (2016) are also shown.

Table 3-2 Estimated composition of the primitive mafic, felsic, and evolved end-member magmas.

	Major elements (wt.%)											Ni ppm
	SiO_2	TiO_2	Al_2O_3	FeO*	MnO	MgO	CaO	Na_2O	K_2O	P_2O_5	total	
Primitive mafic end-member	49.59	1.25	14.96	10.15	0.24	10.06	8.55	3.73	1.01	0.47	100	140.8
Felsic end-member	62.74	0.67	17.96	4.49	0.09	2.34	5.82	4.36	1.29	0.23	100	21.7
Evolved mafic end-member*	51	1.25	18.28	8.59	0.19	5.87	8.91	4.4	1.03	0.48	100	37.5

*: assumed

The composition of the evolved mafic end-member magma is considered to lie on the mixing trend between the felsic end-member magma and the lowest SiO_2 samples with relatively low MgO contents (Xe-36-M) in the andesites. However, unlike the case of the primitive mafic end-member magma, it is difficult to specify the composition, because of the uncertainty of the Fo# of the olivine in equilibrium with the evolved end-member magma. The essentially linear trends of the andesites on the $^{87}Sr/^{86}Sr$–SiO_2 and $^{206}Pb/^{204}Pb$–SiO_2 diagrams (Figs. 3-6) suggest that the Sr and Pb isotopic compositions of the primitive and evolved mafic end-member magmas are similar. Therefore, the two mafic end-member magmas might have had a parent-daughter relationship. In addition, the expected lower MgO and NiO compositions of the evolved mafic end-member magma compared to those of the primitive end-member magma (Figs. 3-7a and 3-7d) suggest that the evolved mafic end-member magma might have been derived from the primitive end-member magma mainly by olivine fractionation. In this case, the olivine fractionation trend from the primitive end-member magma crosses the mixing trend between Xe-36-M and the felsic end-member magma at ~51 wt.% SiO_2 (Fig. 3-7a). If I assume that the SiO_2 content of the evolved mafic end-member magma was 51 wt.% (Table 3-2), this composition can roughly be explained by fractionation of ~10 wt.% olivine from the primitive mafic end-member magma (Fig. 3-7).

3-6-2. Water content and origin of the primitive mafic end-member magma

The cores of plagioclase phenocrysts with high An# up to 87.7 occur characteristically in lower-SiO_2 samples, and they have euhedral outlines. Therefore, the high-An# cores are considered to have crystallized *in situ* in the primitive end-member magma before the magma mixing. Given that the primitive end-member magma was in equilibrium with An#87.7 plagioclase, the water content of the magma was estimated using the plagioclase-melt hygrometer (Putirka, 2008). The mafic end-member magma might have been stored at the Moho depth, as suggested from the occurrence of both crustal and mantle xenoliths in the calc-alkaline andesites (e.g., Kobayashi, 1989). Given that the pressure condition of the plagioclase crystallization was 0.89 GPa (~25 km; Niu et al., 2016), a primitive melt water content of 5.2 ± 1.1 wt.% was obtained by simultaneously solving equation (25b) and (26) as given in Putirka (2008). The remarkably hydrous nature of the

primitive end-member magma indicates that the primary magma was formed by fluid-fluxed melting of the mantle peridotite or by dehydration melting of the mantle peridotite metasomatized by slab-derived fluids.

3-6-3. Origin of the felsic end-member magma

As discussed above, the felsic end-member magma is suggested to have been relatively uniform in composition with ~63 wt.% SiO_2. One possible origin of felsic magma in the island-arc setting is the partial melting of the subducting slab (e.g., Kay, 1978; Defant and Drummond, 1990). The dacitic lavas from Rishiri, that erupted in the Middle Stage, show adakitic signatures (Fig. 3-4d), and one possibility is that this dacitic magma could have been the felsic end-member magma. However, the dacite lavas have higher concentrations of Sr and Ba and lower concentrations of Zr and Nb than those expected from the magma mixing trend (e.g., Figs. 3-4b and 3-4c). This observation suggests that the adakitic dacite magma could not have been the felsic end-member magma for calc-alkaline andesitic magmas.

This leaves either crystal fractionation of a mantle-derived basaltic magma or crustal melting as a possible origin of the felsic end-member magma. It would be difficult to derive the felsic end-member magma solely by fractional crystallization of a mantle derived basaltic magma, considering that the $^{206}Pb/^{204}Pb$ ratio of the felsic end-member magma (>18.5) is significantly higher than those of any basaltic magmas from Rishiri (<~18.4; Fig. 3-6e). This observation suggests that the felsic end-member magma was produced by either partial melting of the crust (e.g., Huppert and Sparks, 1988) or fractional crystallization with simultaneous crustal assimilation, where the ratio of assimilated mass to crystallized mass is high (e.g., DePaolo, 1981). In any case, the partial melt of the crust is considered to have been the main source of the felsic end-member magma.

3-6-4. Petrogenesis of the calc-alkaline andesite

Some clinopyroxene and orthopyroxene phenocrysts have relatively high-Mg# or low-Mg# cores. Because these cores are considered to have been derived from the mafic and felsic end-member magmas, respectively, the rims surrounding the cores of the phenocrysts are considered to have grown after the magma mixing. Therefore, the pressure condition of a magma chamber where magma mixing occurred can be estimated using the compositions of the rims of the coexisting clinopyroxene and orthopyroxene phenocrysts. The two-pyroxene geobarometer of Putirka (2008) yields a pressure of 4.0 ± 3.7 kbar. Although the uncertainty of the pressure estimated is large, calc-alkaline andesitic magmas were produced, most plausibly, at the depth corresponding to lower to middle crust, because the pressure condition corresponding to the Moho depth beneath Rishiri is about ~9 kbar (Niu et al., 2016).

A schematic illustration of the petrogenesis of the calc-alkaline andesite is shown in Fig. 3-8. The primitive hydrous magma, which is considered to have been generated through the fluid-

fluxed melting or dehydration melting of the upper mantle, was injected across the Moho, where some portion of the magma was differentiated to form the evolved mafic end-member magma, mainly by olivine fractionation. Then, the primitive and evolved mafic end-member magmas were emplaced into the middle crust to form a magma chamber, causing extensive melting of the surrounding crust and generation of the felsic end-member magma. The calc-alkaline andesitic magmas were finally produced by mixing of these mafic end-member magmas and the felsic magmas.

3-6-5. Factors controlling the occurrence of calc-alkaline magmatism at Rishiri

At Rishiri Volcano, like at other volcanoes in subduction zone settings, calc-alkaline series rocks and tholeiitic-series rocks coexist (e.g., Fujinawa, 1988; Hunter, 1998; Hunter and Blake, 1995; Sakuyama, 1981). After the Middle Stage in which there was calc-alkaline andesite magmatism, high Na/K alkali basalt lavas (Kutsugata lava) and low Na/K alkali basalt lavas (Nozuka lavas) occurred during the Late-1 and Late-2 Stages, respectively (Fig. 1-3). In this section, the characteristics of the primitive mafic magma, responsible for the generation of the calc-alkaline magmas, are compared with those of parental high Na/K and low Na/K basaltic magmas that did not induce calc-alkaline magmatism.
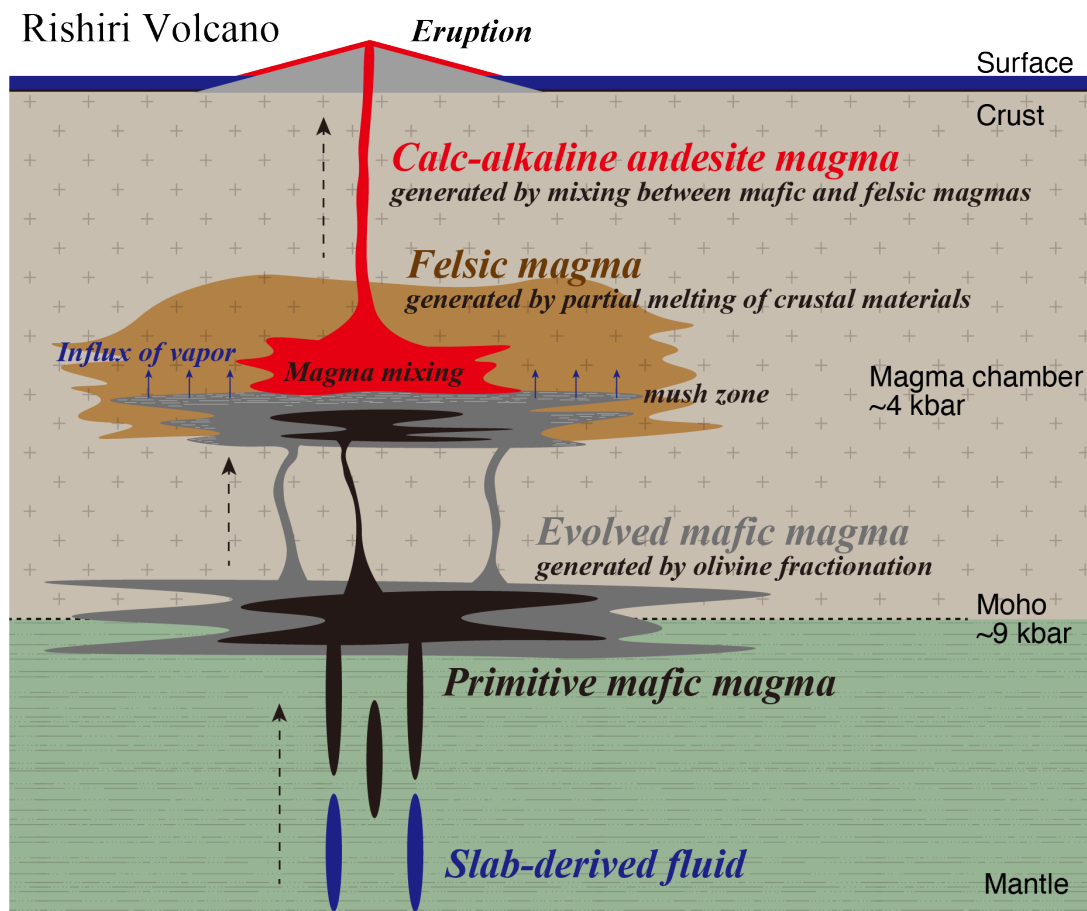

Figure 3-8 Schematic illustration of the generation of the calc-alkaline andesitic magma at the Rishiri Volcano. See text for details.

The high Na/K basaltic magma in the Late-1 Stage is suggested to have been derived from the tholeiitic-series intermediate magmas by assimilation and fractional crystallization in a crustal magma chamber with a low ratio of assimilated mass to fractionated mass, and the intermediate magmas were erupted as Tanetomi lavas (Kuritani, 1998, 1999, 2001; Kuritani et al., 2005, 2007). The water content of the primary high Na/K basaltic magma is estimated to be ~3 wt.% (Kuritani, 1999). On the other hand, the low Na/K basaltic lavas in the Late-2 Stage were associated with rhyolitic products without intermediate products (Ishizuka and Nakagawa, 1999; Kobayashi, 1989). The basaltic lavas consist of the low-K and high-K lavas, and the water contents of the primary magmas are estimated to be 2.2 ± 1.0 wt.% and 2.1 ± 1.0 wt.%, respectively (Kuritani and Nakagawa, 2016).

The primary magmas in the Middle, Late-1, and Late-2 Stages, are all alkali basaltic in composition. However, their water contents are significantly different, being ~5 wt.% for the Middle Stage, ~3 wt.% for the Late-1 Stage, and ~2 wt.% for the Late-2 Stage. Therefore, I infer that the water content of the primary magma might have been the main factor controlling the generation of calc-alkaline magmatism at Rishiri. In that sense, calc-alkaline magmatism occurred when the primary magma was water-rich (>~5 wt.%), such as the case in the Middle Stage, while this magmatism was not associated when the primary magma was less hydrous, such as the cases in the Late-1 and Late-2 Stages.
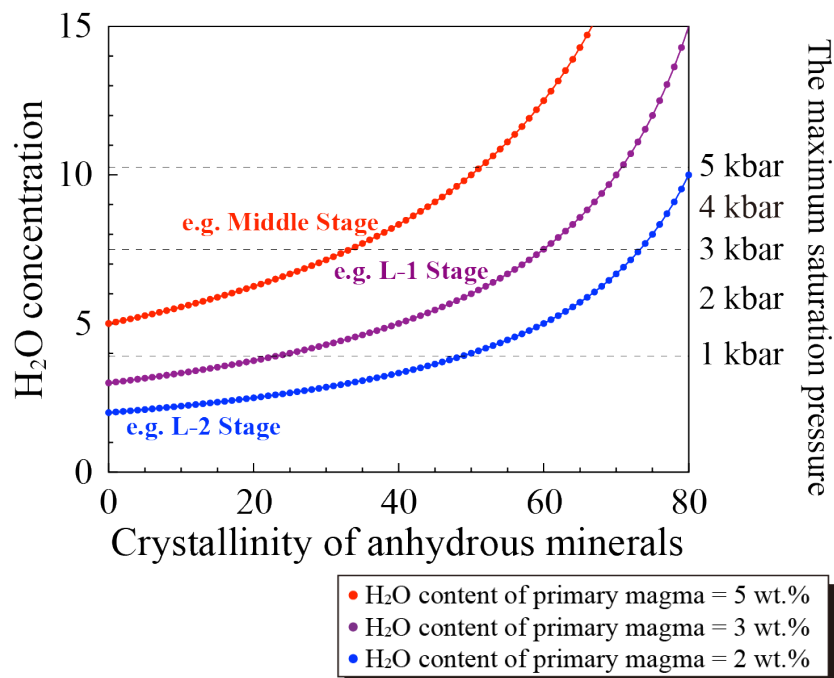

Figure 3-9 Relationship between H_2O concentration in the melt and the crystallinity of the magma for the three primitive magmas at Rishiri. The water saturation in the melt was calculated using the model of Papale et al. (2006). See text for details.

Theoretical studies have suggested that the crust overlying a magma chamber can melt extensively due to the large convective heat flux from the magma chamber (e.g., Huppert and Sparks, 1988). In addition, it has also been well recognized that the solidus temperatures of the crustal materials are greatly affected by the water content of the system, and that, at given temperature and pressure conditions, the melting degree is much higher in an hydrous system than that in an anhydrous system (e.g., Lambert and Wyllie, 1974). Upon the emplacement of mafic magma into the crust to form a magma chamber, the magma is cooled by its surroundings, and a mushy boundary layer develops along the chamber walls. Because the boundary layer spans the temperature range from the solidus to near liquidus of the magma (e.g., Tait and Jaupart, 1996), water saturation is attained in the interstitial melt of the mush zone even if the initial magma is not saturated with water at the depth of the magma chamber. Therefore, in the roof mush zone, vapors exsolved from the interstitial melt may move upward and enter the overlying crust (Fig. 3-8). Therefore, the flux of vapors from the magma chamber can further facilitate the melting of the overlying crust by reducing its solidus temperatures. Fig. 3-9 shows the relationship between the crystallinity and water content of the interstitial melt in the mush zones for the three primary magmas at Rishiri, calculated using the model of Papale et al. (2006). For the primary magma at the Middle Stage, water saturation would be attained when it crystallizes <45 wt.% at 4 kbar. On the other hand, water saturation is not attained for the primary melts of the Late-1 and Late-2 stages until they crystallize <65 wt. % and <80 wt.%, respectively, at 4 kbar. Therefore, a more hydrous magma, such as that of the primitive magma responsible for the generation of the calc-alkaline andesite magma, can supply a higher vapor flux from the solidifying magma chamber to the overlying crust, resulting in more extensive melting of the crust.

The calc-alkaline andesite magmas at Rishiri were generated essentially by magma mixing between mantle-derived mafic magma and crust-derived felsic magma; these petrogenetic processes are similar to those indicated by previous studies (e.g., Kay and Kay, 1985; Kay et al., 1982; Sakuyama, 1981; Streck et al., 2007). Factors such as the convective heat flux from a magma chamber, repetitive injections of mafic magma into a magma chamber, and the water content of the magma in a magma chamber, have been proposed as the cause of extensive melting of the crust (e.g., Annen et al., 2006; Huppert and Sparks, 1988; Kimura et al., 2015; Rooney and Deering, 2014). In this study, I compared the water contents of the primary magmas from three different eruption stages of Rishiri Volcano and demonstrated that the largest-scale crustal melting occurred actually when the most hydrous primary magma was active, resulting in the highest eruption rate in the history of the volcano. Our results suggest that the water content of a primary magma can control not only the productivity of crust-derived felsic magmas, but also the occurrence of calc-alkaline magmatism in individual volcanic systems.

3-7. Conclusion

To understand the petrogenesis of calc-alkaline andesites and what factor controls the occurrence of calc-alkaline magmatism at Rishiri, I carried out a detailed petrological and geochemical study on the products from the volcano. I reached the following conclusions:

1. The calc-alkaline andesitic lavas show petrological and geochemical evidence of magma mixing, and the magmas are considered to have been produced by mixing of three end-member magmas; a primitive mafic end-smember magma, an evolved mafic end-member magma, and a felsic end-member magma.

2. The primitive mafic end-member magma is suggested to represent a near primary magma generated by fluid-fluxed melting or dehydration melting of the upper mantle, and the evolved mafic end-member magma was derived from that primitive magma by olivine fractionation. The felsic end-member magma is considered to have been produced primarily by partial melting of the crust caused by the emplacement of the mafic magmas.

3. The water content of the primitive end-member magma was estimated to be 5.2 ± 1.1 wt.% by plagioclase–melt hygrometry. The pressure condition of the magma chamber, in which calc-andesite magmas were generated through magma mixing, was estimated to be 4.0 ± 3.7 kbar using a two pyroxene geobarometer.

4. The estimated water content of ~5 wt.% in the primitive end-member magma was much higher than those of primary high-Na/K and low-Na/K basaltic magmas from other volcanic stages with which calc-alkaline magmas were not associated. Because more hydrous magmas have a greater potential to cause extensive melting of the crust surrounding the magma chamber, I conclude that the water content in a primary magma is the main factor controlling the genesis of calc-alkaline magmatism at Rishiri.

Chapter 4. Nature and behavior of slab-derived fluids: Constrains from the adakitic dacites

Abstract

Felsic magmas produced at subduction zones have played an important role in the generation and evolution of the continental crust. For the origin of felsic magmas, processes such as fractional crystallization of mafic magmas, partial melting of crustal materials, partial melting of subducting slabs, and partial melting of pyroxenitic mantle wedge components have been proposed. Recent experimental studies have predicted that felsic melt can also be produced in the mantle wedge by the separation of slab-derived supercritical liquid beyond depths corresponding to the critical point. To date, however, the presence of felsic magma of this origin has not yet been reported. In this study, I investigated dacitic lavas and preceding calc-alkaline andesite lavas from the Rishiri Volcano, located at the rear of the Kuril arc. I show that hydrous felsic melt and aqueous fluid were separated from slab-derived supercritical liquid in the mantle wedge. The former erupted as dacitic magma whilst the aqueous fluid induced the generation of primary basaltic magma involved in creating calc-alkaline andesite magma. I infer that slab-derived supercritical liquid is an efficient transport medium for moving silicate-rich components from subducting slabs to the Earth's surface, and that this process may have contributed to the growth of the continental crust.

4-1. Introduction

Subduction-zone magmatism is considered to have played an important role in the generation and evolution of the continental crust, because the chemical composition of calc-alkaline andesites that are widespread in island arcs and active continental margins is similar to the average composition of the continental crust (Taylor and White, 1965; Rudnick and Gao, 2003). Primary mafic magmas are thought to be generated by melting of the mantle wedge with an influx of slab-derived water-rich materials (Gill, 1981; Elliott, 2003). Intermediate to felsic magmas (andesite to rhyolite) are also commonly produced in many subduction zones. Some felsic magmas have been emplaced as large granitic plutons, which contribute to the establishment of a buoyant continental crust (Petford et al., 2000; Arndt, 2013), and others have mixed with mafic magmas to produce calc-alkaline andesitic magmas and other intermediate magmas in crustal magma chambers (Eichelberger, 1975), producing geochemical variability in the crust (Rudnick and Gao, 2003).

It has been suggested that felsic magmas found at subduction-zone volcanoes are produced by mechanisms including fractional crystallization with or without crustal assimilation (DePaolo, 1981), partial melting of the crust (Huppert and Sparks, 1988; Annen et al., 2006), and

partial melting of metasomatised silica-excess pyroxenite mantle (Straub et al., 2011; Straub et al., 2008). In addition, adakitic magmas with high-Sr/Y ratios (Defant and Drummond, 1990) and high $[La/Yb]_N$ (primitive mantle-normalised La/Yb) ratios (Martin, 1986; Martin et al, 2005) can also be produced by partial melting of hot subducting slabs at young subduction zones (Martin, 1986; Defant and Drummond, 1990; Martin et al., 2005) and by partial melting of garnet-bearing lower part of the thick crust (Atherton and Petford, 1993; Ma et al., 2015).

Recently, experimental studies have suggested that intermediate to felsic magma may also be produced as hydrous melt through the separation of slab-derived supercritical liquids in the sub-arc mantle. At relatively shallow depths, the slab-derived materials are released as aqueous fluid or hydrous melt. However, with increasing depths of fluid release, the solubility of silicate materials in aqueous fluid tends to become close to those of water in silicate melt, and the slab-derived water-rich materials would eventually become supercritical liquids at the critical point. On the other hand, ascending slab-derived supercritical liquid would separate into aqueous fluid and hydrous melt at the critical point (Shen and Kepper, 1997; Bureau and Keppler, 1999). Because the pressure corresponding to the critical end-point for silicic supercritical liquid can be as low as <3 GPa, andesitic to dacitic magmas would be generated by the separation of slab-derived supercritical liquid in sub-arc mantle (Kawamoto et al., 2012). To date, however, the presence of magmas originating from this process has not yet been reported in nature.

Rishiri Volcano is a Quaternary stratovolcano at the rear of the southern Kuril arc, located 300 km above the Wadati-Benioff Zone (Fig. 1-3). Previous studies have suggested that slab-derived supercritical liquid has been released from the subducting slab (Kuritani et al., 2008; Kuritani and Nakagawa, 2016), and that some dacitic lavas have adakitic geochemical signatures. In this study, I conducted a detailed petrological, geochemical, and chronological study on the dacites. I suggest that the dacitic magmas represent hydrous melts generated through separation of slab-derived supercritical liquid.

4-2. Geological and petrological background of the adakitic dacite

The Rishiri Volcano is characterised by the coexistence of alkali basalt, tholeiitic andesite to dacite, and calc-alkaline andesite to dacite (Ishizuka and Nakagawa, 1999; Fig. 4-1a). The main target of this chapter are the calc-alkaline dacitic lavas, which constitute the main edifice of the volcano together with the calc-alkaline andesite lavas and pyroclastics (Ishizuka, 1999; Figs. 1-3, 4-1a, and 4-2). These dacites and andesites belong to the Middle Stage of volcanic activity, characterised by the highest eruption rate over the lifetime of the volcano (Ishizuka, 1999). The petrogenesis of the calc-alkaline andesites was investigated in detail by the Chapter 3. The magmas were suggested to have been produced via mixing between crust-derived felsic magmas and primitive basaltic magmas generated through fluid-fluxed melting of the mantle. The dacitic lavas

always overly the andesitic lavas in the area (Fig 4-2), indicating that the eruption of the andesitic magma predated that of the dacitic magma. $^{40}Ar/^{39}Ar$ dating shows that activity leading to production of the dacite and andesite took place at 35.5 ± 1.4 and 34.6 ± 3.0 ka, respectively (as described in the Chapter 2; Fig. 2-1).

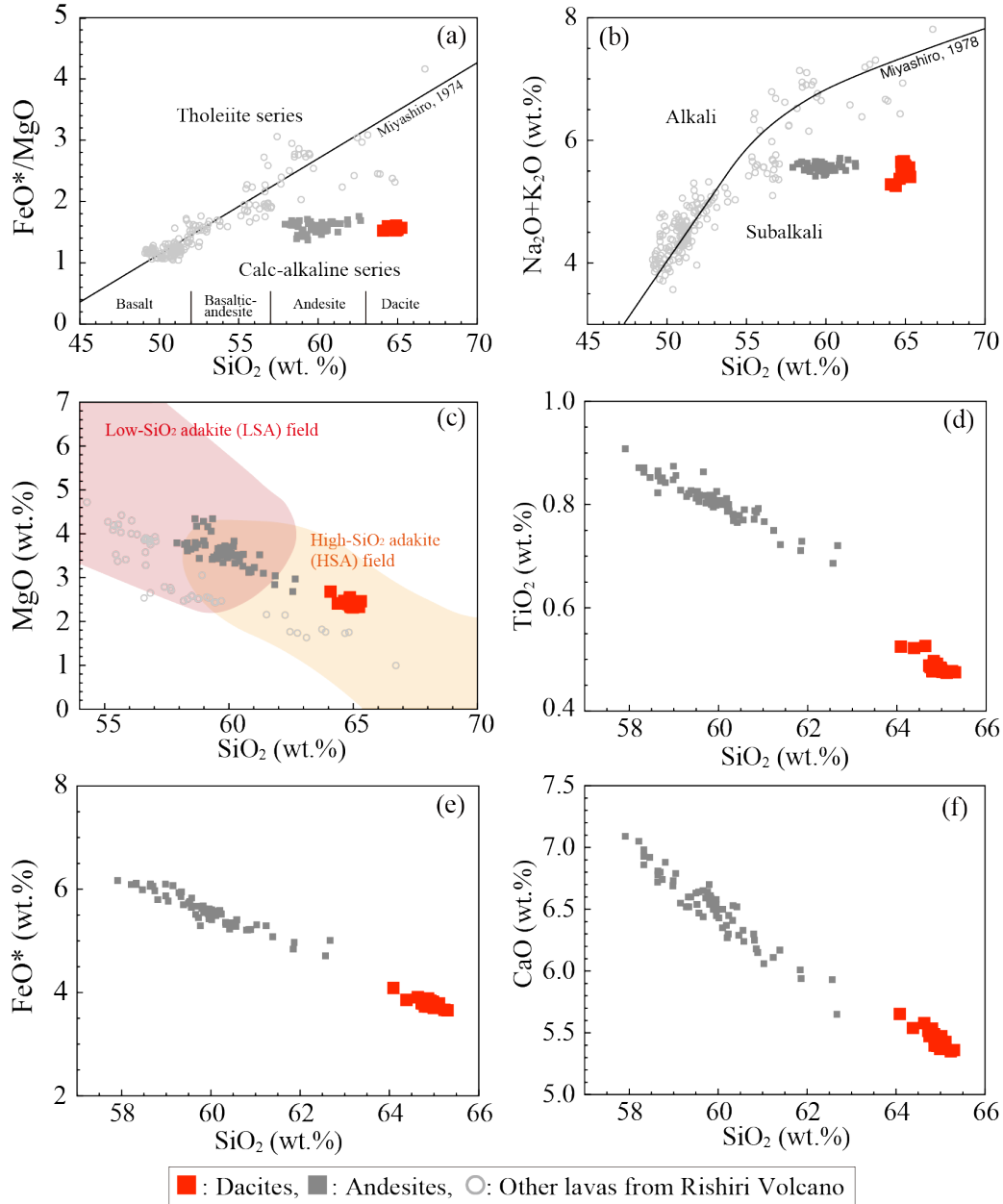Figure 4-1 The whole-rock compositions of the dacite and the andesite lavas from the Rishiri Volcano, shown in (a) FeO/MgO–SiO$_2$ diagram, (b) Na$_2$O+K$_2$O–SiO$_2$ diagram, (c) MgO–SiO$_2$ diagram, (d) TiO$_2$–SiO$_2$ diagram, (e) FeO*–SiO$_2$ diagram, and (f) CaO–SiO$_2$ diagram. In (a) and (b), discrimination line between calc-alkaline and tholeiite series, and alkali and sub-alkali series are taken from Miyashiro (1974) and Miyashiro (1978), respectively. In (c), the compositional fields of the Low-SiO$_2$ adakite (LSA) and High-SiO$_2$ adakite (HSA) are taken from Martin et al. (2005). In (a)–(c), the whole-rock composition of the other lavas from the Rishiri of Ishizuka (2000) are also shown.
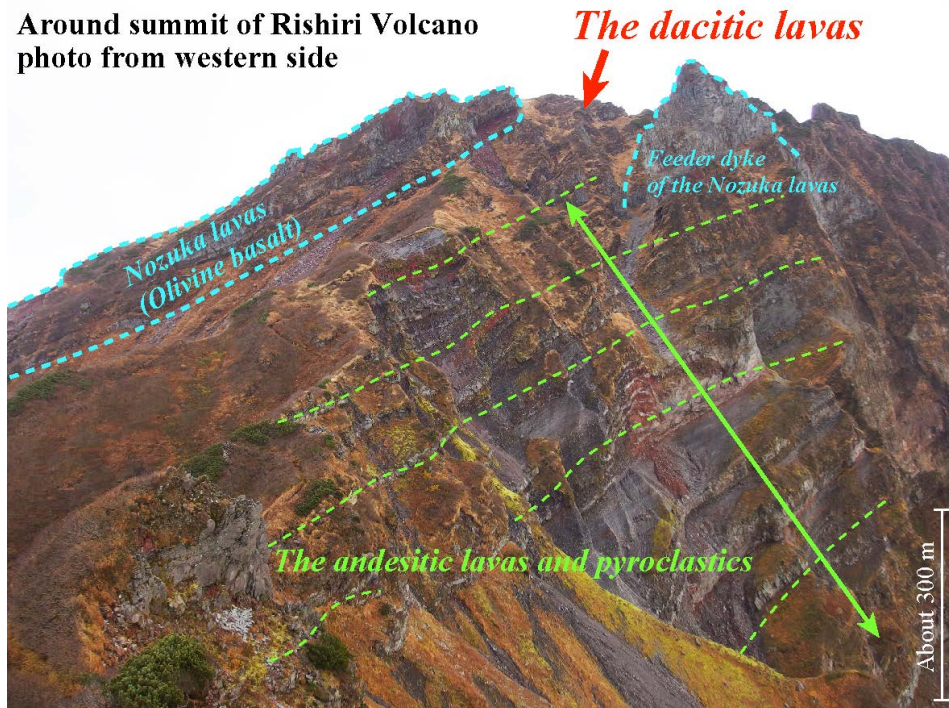
Figure 4-2 Photograph showing the calc-alkaline andesitic lavas and pyroclastics conformably overlain by the dacitic lavas. Nozuka lavas and a feeder dyke, erupted after the dacitic lavas (28,230 ± 1,020 y. BP; Miura and Takaoka, 1993), are also shown.

4-3. Analytical methods

The methods for sample preparation, whole-rock major, trace, and isotope (Sr-Nd-Pb) analysis, and mineral composition analysis are same as described in the Chapter 3.

Isotope analyses of U and Th are conducted by a TIMS (Finnigan MAT262 with RPQplus) at Okayama University. In this paper, isotopic ratios in parentheses represent activity ratios. Decay constants of the U and Th nuclides (Le Roux and Glendenin, 1963; Jaffey et al., 1971; Cheng et al., 2000) used for calculations in this study are $\lambda_{238U} = 1.55125 \times 10^{-10}$, $\lambda_{234U} = 2.8263 \times 10^{-6}$, $\lambda_{232Th} = 4.9475 \times 10^{-11}$, and $\lambda_{230Th} = 9.158 \times 10^{-6}$. The details of the analytical procedures at Okayama University, including those of the chemical separations and data correction, reflect those presented by Kuritani et al. (2008).

4-4. Petrography and mineral chemistry

The phenocryst assemblage of the dacite lavas is composed of clinopyroxene, orthopyroxene, and plagioclase, some of which form crystal aggregates (Fig. 4-3). All phenocrysts are clear under a polarised light microscope, and sieve-textured plagioclase is not found. The phenocrysts are homogeneous or normally zoned, with limited variation in their core composition (Fig. 4-4).
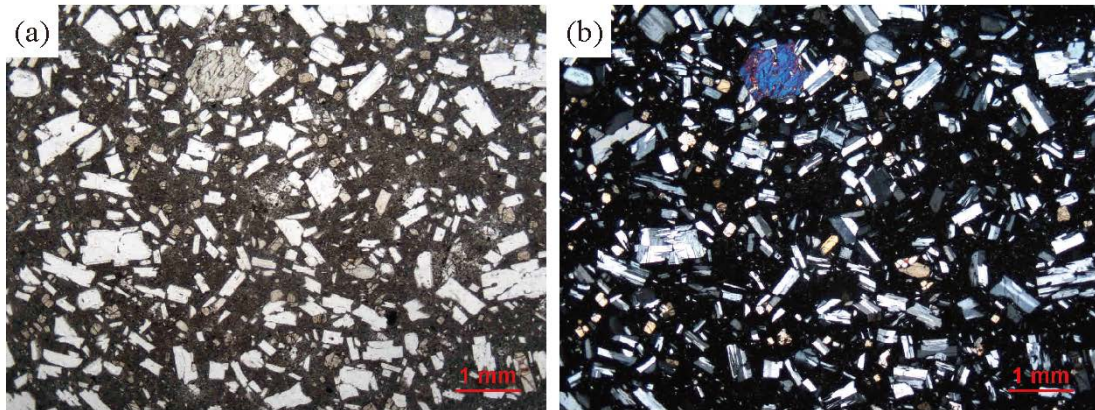
Figure 4-3 Photomicrographs of representative samples of (a, b) the dacite lava (parallel-and cross-polarized light, respectively).
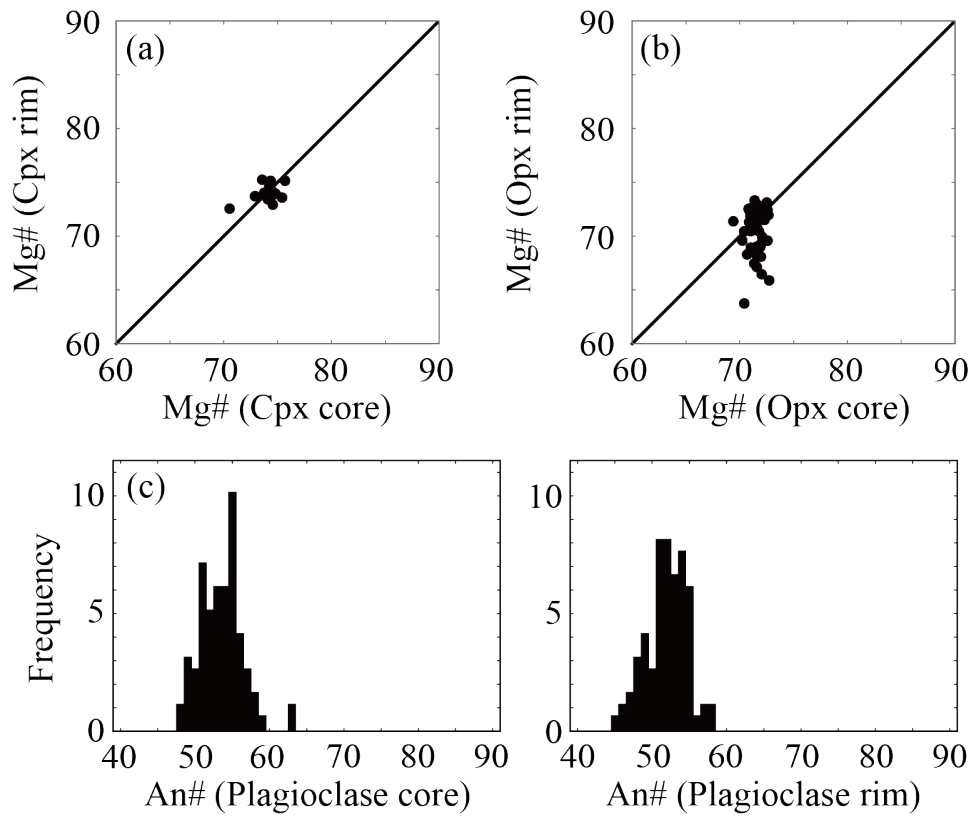

Figure 4-4 Compositions of (a) clinopyroxene and (b) orthopyroxene phenocrysts and (c) histograms of the An# contents of the cores and rims of plagioclase phenocrysts in the dacitic samples.

4-5. Whole-rock compositions

The whole-rock major and trace elements and Sr-Nd-Pb and U-Th isotope data of the dacite samples are presented in Tables 4-1 and 4-2, and selected variation diagrams are shown in Figs 4-1, 4-5, and 4-7.

4-5-1. Major elements

The whole-rock SiO_2 content of the dacites ranges from 64.1 to 65.3 wt.% (Table 4-1, Figs.4-1). The dacites and the preceding andesites belong to the calc-alkaline series in the Miyashiro diagram (Miyashiro, 1974; Fig. 4-1a). The dacitic lavas have a relatively high MgO (2.3–2.7 wt.%; Fig. 4-1c) content compared with other felsic lavas from the Rishiri Volcano. The Mg#'s [= $Mg/(Mg+Fe^{total}) \times 100$] of the dacites of 52–54 are similar to the average continental crust (~55; Rudnick and Gao, 2003), and are lower than those of mantle-derived primary melt (> 60).

4-5-2. Trace elements

The dacitic lavas have a relatively high Cr (25–42 ppm; Fig. 4-5a) and Ni (26–39 ppm) content compared with other felsic lavas from the Rishiri Volcano. The dacitic lavas are also characterised by high Sr/Y (48–55) and $[La/Yb]_N$ (9–11) ratios, and low Yb_N (2.5–3.0) (i.e., adakitic signature; Martin, 1986; Defant and Drummond, 1990) compared with the andesitic lavas (Figs. 4-5b–d), and have been classified as high-SiO_2 adakite (Martin et al, 2005; Figs. 4-1c and4-5b). No significant Eu anomaly is observed in the dacite lavas (Fig. 4-5d), with the exception of one outlier sample with extremely low P_2O_5, Y, and Yb content (Fig. 4-6).

4-5-3. Radiogenic isotopes

The dacitic lavas have higher $^{87}Sr/^{86}Sr$, $^{208}Pb/^{204}Pb$ and $^{206}Pb/^{204}Pb$ ratios and lower $^{143}Nd/^{144}Nd$ ratios than both the calc-alkaline andesitic and basaltic lavas from the volcano (Figs. 4-7a and 4-7b). The Pb isotopic compositions of the dacitic lavas are mostly on the binary mixing line between sediments (SED) and altered oceanic crust (AOC) (Fig. 4-7b). In a U–Th equiline diagram, age corrected compositions of the dacitic and andesitic lavas (Table 4-2) plot on the left-hand side of the equiline (Fig. 4-7c).

Table 4-1. Results of elemental and isotopic analyses for the dacitic lavas from the Rishiri Volcano.

No.	1	2	3	4	5	6	7	8	9	10
Sample	AF-3	AF-6	AF-101	AF-102	AF-103	AF-106	AF-107	OC-5	OC-8	OC-9
Type	Dacite	Dacite	Dacite	Dacite	Dacite	Dacite	Dacite	Dacite	Dacite	Dacite
Latitude (°N)	45°10'58"	45°10'56"	Boulder	Boulder	Boulder	Boulder	Boulder	45°11'55"	45°11'49"	45°11'53"
Longitude (°E)	141°16'14"	141°16'22"	Boulder	Boulder	Boulder	Boulder	Boulder	141°16'15"	141°16'7"	141°16'12"
Laboratory	Hokkaido	Hokkaido	Hokkaido	Hokkaido	Hokkaido	Hokkaido	Hokkaido	Hokkaido	Hokkaido	Hokkaido
Major elements (wt. %)										
SiO_2	64.5	64.96	64.66	64.67	64.01	64.48	64.88	64.54	64.98	64.8
TiO_2	0.47	0.48	0.49	0.48	0.49	0.49	0.48	0.48	0.48	0.48
Al_2O_3	17.13	17.15	16.95	17.17	16.81	17.03	17.14	17.08	17.15	17.18
Fe_2O_3*	4.13	4.14	4.31	4.2	4.19	4.13	4.17	4.12	4.14	4.1
MnO	0.08	0.08	0.09	0.09	0.09	0.09	0.09	0.09	0.08	0.08
MgO	2.39	2.42	2.54	2.45	2.41	2.31	2.41	2.35	2.42	2.36
CaO	5.47	5.42	5.38	5.47	5.42	5.42	5.39	5.42	5.4	5.35
Na_2O	4.35	4.33	4.28	4.35	4.31	4.37	4.34	4.38	4.33	4.31
K_2O	1.23	1.22	1.22	1.22	1.24	1.25	1.24	1.25	1.23	1.25
P_2O_5	0.2	0.2	0.2	0.2	0.2	0.2	0.2	0.2	0.2	0.2
total	99.95	100.41	100.96	101.14	100.02	100.62	101.19	100.75	100.42	100.11
LOI	0.16	0.22	0.44	0.51	0.15	0.2	0.32	0.23	0.37	0.38
Trace elements (ppm)										
Sc (XRF)	13.2	10.1	12.8	13.7	11.4	11.2	12.8	10.8	12.6	10.5
V (XRF)	74.9	74.8	79	76	80.2	74.7	76.3	79.1	72.4	79
Cr (XRF)	35.2	34.2	41.7	35.8	35.5	33.9	35.4	34	37.6	33.8
Co (XRF)	15.2	15	15.8	14.7	14.7	14.8	13.6	13.8	14.8	15.6
Ni (XRF)	28.4	26.8	30.7	27.9	27.2	26.8	27.9	27.3	27.4	26.8
Li										
B										
Be										
Rb	31.5			30.9				30.1		
Sr	597			580				580		
Y	11.8			11.6				11.3		
Zr	143			140				150		
Nb	6.68			6.6				6.65		
Cs	0.81			0.84				0.68		
Ba	374			376				376		
La	21.6			21				20.8		
Ce	38.5			37.9				41.2		
Pr	4.04			3.99				3.97		
Nd	14.6			14.5				14.6		
Sm	2.66			2.63				2.64		
Eu	0.87			0.86				0.84		
Gd	2.63			2.62				2.53		
Tb	0.36			0.36				0.36		
Dy	2.15			2.15				2.16		
Ho	0.44			0.43				0.43		
Er	1.31			1.3				1.31		
Tm	0.19			0.19				0.2		
Yb	1.35			1.33				1.36		
Lu	0.21			0.21				0.22		
Hf	3.31			3.28				3.39		
Ta	0.52			0.51				0.53		
Pb	5.25			5.52				5.27		
Th	4.74			4.75				4.81		
U	1.3			1.29				1.34		
Isotopes (MC-ICP-MS or TIMS)										
$^{87}Sr/^{86}Sr$	0.703296			0.703296				0.703383		
2SE	0.000013			0.000005				0.000019		
$^{143}Nd/^{144}Nd$	0.512923			0.512926				0.51292		
2SE	0.000012			0.000012				0.000011		
$^{206}Pb/^{204}Pb$		18.5444						18.5449	18.5443	
2SE		0.0005						0.0003	0.0006	
$^{207}Pb/^{204}Pb$		15.5595						15.5595	15.5591	
2SE		0.0005						0.0003	0.0005	
$^{208}Pb/^{204}Pb$		38.437						38.4368	38.4358	
2SE		0.0015						0.0009	0.0016	

*total Fe given as Fe2O3. Errors on isotope ratios are within-run 2 SE.

Table 4-1. Continued.

No.	11	12	13	14	15	16	17	18	19	20
Sample	OC-10	KT-21	KT-29	KT-30	OS-2	Af-5	Af-6	Or-9	Or-10	Y-1
Type	Dacite	Dacite	Dacite	Dacite	Dacite	Dacite	Dacite	Dacite	Dacite	Dacite
Latitude (°N)	45°11'51"	45°11'2"	45°11'0"	45°11'0"	45°10'46"	45°10'55.4"	45°10'58"	45°10'50"	45°10'50"	45°11'53"
Longitude (°E)	141°16'10"	141°13'23"	141°13'4"	141°13'4"	141°14'30"	141°16'47"	141°16'15"	141°14'29"	141°14'29"	141°16'13"
Laboratory	Hokkaido	Hokkaido	Hokkaido	Hokkaido	Hokkaido	Okayama	Okayama	Okayama	Okayama	Okayama
Major elements (wt. %)										
SiO_2	63.92	64	63.85	64.23	65.37	64.54	64.39	64.39	64.36	64.35
TiO_2	0.48	0.52	0.52	0.52	0.48	0.48	0.48	0.47	0.47	0.48
Al_2O_3	16.93	17.71	17.35	17.13	17.14	17.08	17.01	16.89	16.89	16.91
Fe_2O_3*	4.16	4.26	4.53	4.32	4.08	4.19	4.21	4.16	4	4.21
MnO	0.08	0.08	0.09	0.09	0.08	0.08	0.08	0.08	0.08	0.09
MgO	2.38	2.4	2.67	2.46	2.34	2.31	2.39	2.35	2.42	2.35
CaO	5.45	5.51	5.63	5.54	5.36	5.38	5.5	5.37	5.28	5.38
Na_2O	4.34	4.12	4.15	4.17	4.31	4.25	4.31	4.19	4.13	4.27
K_2O	1.24	1.1	1.11	1.17	1.26	1.24	1.22	1.24	1.2	1.25
P_2O_5	0.19	0.12	0.17	0.18	0.2	0.18	0.19	0.17	0.12	0.18
total	99.18	100.68	100.94	100.66	101.48	99.75	99.78	99.31	98.96	99.46
LOI	0.44	1.62	1.63	1.37	0.29	0.32	0.28	0.47	0.69	0.35
Trace elements (ppm)										
Sc (XRF)	9.75	11.3	11.8	12.8	11.1					
V (XRF)	73.1	79.7	83.5	82.7	78.4					
Cr (XRF)	33.1	31.2	32.7	30.7	33.4	25.6	27.5	26.9	27.5	26.9
Co (XRF)	15.2	15.7	15.7	15.9	13.9					
Ni (XRF)	26.3	27.5	29.6	27.5	27.1	25.5	25.6	25.7	24.6	25.7
Li						13.9	13.2	7.53	11.2	11
B						8.46	8.2	8.88	11.5	8.32
Be						1.2	1.17	1.21	1.21	1.19
Rb	30.9	22.5			30.4	32.5	31	31.8	30.5	32.5
Sr	581	532			569	588	604	573	577	588
Y	11.5	10.8			11.7	11.7	11.8	11.8	10.5	11.9
Zr	142	145			153	148	151	147	144	148
Nb	6.67	6.31			6.9	6.49	6.5	6.5	6.5	6.38
Cs	0.76	1.1			0.84	0.76	0.81	0.83	0.97	0.8
Ba	370	323			383	384	375	381	384	383
La	20.8	18.2			21.4	20.9	21.5	21.5	19.1	21.5
Ce	37.8	37.2			42.6	38.2	38.3	38.7	32.6	38.4
Pr	3.94	3.57			4.02	4.12	4.12	4.1	3.29	4.06
Nd	14.4	13.2			14.6	14.4	14.6	14.6	12	14.9
Sm	2.62	2.51			2.67	2.68	2.71	2.62	2.08	2.73
Eu	0.86	0.82			0.84	0.88	0.89	0.85	0.84	0.87
Gd	2.6	2.42			2.6	2.48	2.58	2.56	2.11	2.51
Tb	0.35	0.35			0.36	0.36	0.35	0.36	0.3	0.38
Dy	2.13	2.18			2.2	2.15	2.16	2.24	1.8	2.25
Ho	0.43	0.44			0.45	0.44	0.44	0.44	0.39	0.45
Er	1.31	1.32			1.33	1.34	1.34	1.29	1.12	1.37
Tm	0.19	0.2			0.2	0.2	0.2	0.2	0.18	0.21
Yb	1.34	1.38			1.39	1.41	1.36	1.38	1.25	1.4
Lu	0.21	0.21			0.22	0.22	0.21	0.22	0.21	0.22
Hf	3.32	3.35			3.37	3.31	3.3	3.2	3.21	3.27
Ta	0.52	0.52			0.55	0.55	0.53	0.53	0.56	0.53
Pb	5.46	5.54			5.34	5.27	5.59	5.68	6.95	5.47
Th	4.77	4.21			4.8	4.91	4.86	4.99	5.11	5.1
U	1.3	1.21			1.38	1.28	1.33	1.39	1.38	1.42
Isotopes (MC-ICP-MS or TIMS)										
$^{87}Sr/^{86}Sr$	0.703328	0.70332			0.703389					0.70337
2SE	0.000013	0.000017			0.000019					0.000007
$^{143}Nd/^{144}Nd$	0.512919	0.512917			0.51291					0.512929
2SE	0.000011	0.000008			0.000012					0.000006
$^{206}Pb/^{204}Pb$		18.5391			18.5469	18.5437	18.5416	18.5467	18.5416	18.5431
2SE		0.0008			0.0008					
$^{207}Pb/^{204}Pb$		15.5579			15.5591	15.5587	15.5573	15.559	15.5613	15.5582
2SE		0.0006			0.0007					
$^{208}Pb/^{204}Pb$		38.422			38.4377	38.4352	38.4319	38.4375	38.44	38.4334
2SE		0.002			0.0019					

*total Fe given as Fe_2O_3. Errors on isotope ratios are within-run 2 SE.

Table 4-1. Continued.

No.	21	22	23	24	25	26	27	28	29	30
Sample	Y-2A	Y-3	Y-8	Y-9	Y-19	Y-26	Af-1B	Af-4B	Af-7B	Af-9
Type	Dacite	Dacite	Dacite	Dacite	Dacite	Dacite	Andesite	Andesite	Andesite	Andesite
Latitude (°N)	45°11'52"	45°11'52"	45°11'53"	45°11'49"	45°11'53"	45°11'49"	45°10'44"	45°10'53"	45°10'55"	45°11'02"
Longitude (°E)	141°16'12"	141°16'12"	141°16'13"	141°16'07"	141°16'13"	141°16'07"	141°16'52"	141°16'21"	141°16'12"	141°15'58"
Laboratory	Okayama	Okayama	Okayama	Okayama	Okayama	Okayama	Okayama	Okayama	Okayama	Okayama
Major elements (wt. %)										
SiO_2	64.62	64.11	64.89	64.46	64.29	64.71	59.67	57.98	57.59	62.23
TiO_2	0.48	0.47	0.48	0.48	0.48	0.48	0.82	0.85	0.86	0.68
Al_2O_3	16.99	16.91	17.09	17.1	16.91	17.04	17.98	17.74	17.86	17.39
Fe_2O_3*	4.29	4.15	4.18	4.19	4.23	4.23	6.13	6.71	6.7	5.21
MnO	0.09	0.08	0.08	0.08	0.09	0.08	0.11	0.13	0.13	0.1
MgO	2.49	2.31	2.33	2.41	2.38	2.4	3.5	3.64	3.57	2.66
CaO	5.47	5.39	5.46	5.47	5.42	5.45	6.65	6.74	6.89	5.89
Na_2O	4.25	4.27	4.29	4.3	4.26	4.24	4.29	4.29	4.34	4.25
K_2O	1.22	1.25	1.25	1.24	1.24	1.23	1.23	1.18	1.16	1.35
P_2O_5	0.18	0.18	0.18	0.18	0.18	0.18	0.26	0.3	0.3	0.22
total	100.07	99.13	100.22	99.91	99.46	100.05	100.62	99.54	99.41	99.99
LOI	0.27	0.35	0.29	0.2	0.27	0.34	-0.06	0.19	0.81	0.13
Trace elements (ppm)										
Sc (XRF)										
V (XRF)										
Cr (XRF)	26.6	24.5	25.5	25.5	25.7	26.5	55.4	40.8	41.3	26
Co (XRF)										
Ni (XRF)	39.4	31.4	36.2	35	31.8	36.2	39.1	28.7	26	22
Li	13.9	12.2	13.6	12.1	15	13.3	13.4	8.97	10.6	11
B	8.41	8.06	8.44	7.38	10.2	8.67	8.72	6.11	7.73	9.09
Be	1.26	1.28	1.18	1.16	1.15	1.27	1.24	1.33	1.51	1.25
Rb	32.9	33.8	31.9	30.3	31.6	32.4	26.7	26.6	26.8	30.9
Sr	600	596	583	578	579	595	559	598	623	527
Y	12.1	12.1	12	11.3	12	11.7	18.1	19.8	20.7	17
Zr	145	149	150	148	151	145	155	154	163	168
Nb	6.36	6.36	6.41	6.43	6.53	6.36	6.43	6.32	6.5	6.99
Cs	0.8	0.74	0.83	0.71	1.11	0.77	1.86	0.61	1.29	0.82
Ba	377	384	376	369	380	379	309	310	314	351
La	21.3	21.6	21.6	20.5	20.9	21.5	19.5	18.9	19.6	21.1
Ce	38.9	39.1	38.4	37.6	38.2	38.8	39.9	39.2	41.3	40.3
Pr	4.04	4.09	4.05	3.91	3.91	4.02	4.46	4.73	4.97	4.41
Nd	14.9	15.3	14.5	14.4	14.2	15.4	18.8	19.1	20.4	17.3
Sm	2.78	2.7	2.71	2.62	2.59	2.74	3.86	4.21	4.27	3.45
Eu	0.89	0.89	0.87	0.84	0.87	0.85	1.19	1.29	1.33	1.06
Gd	2.77	2.83	2.47	2.5	2.39	2.71	4.03	4.28	4.26	3.44
Tb	0.4	0.37	0.37	0.35	0.36	0.36	0.57	0.61	0.64	0.52
Dy	2.22	2.23	2.19	2.1	2.15	2.15	3.45	3.65	4.08	3.14
Ho	0.45	0.45	0.43	0.43	0.43	0.46	0.72	0.78	0.8	0.66
Er	1.34	1.39	1.3	1.3	1.29	1.37	2.07	2.36	2.39	1.96
Tm	0.21	0.21	0.19	0.19	0.2	0.22	0.3	0.33	0.36	0.3
Yb	1.44	1.4	1.4	1.36	1.35	1.46	2.11	2.31	2.39	2
Lu	0.23	0.24	0.22	0.21	0.22	0.24	0.31	0.37	0.37	0.31
Hf	3.38	3.37	3.3	3.19	3.22	3.4	3.59	3.54	3.54	3.7
Ta	0.56	0.55	0.53	0.53	0.51	0.57	0.52	0.48	0.46	0.55
Pb	5.98	6.18	5.82	5.51	5.79	5.87	4.01	3.41	4.8	5.22
Th	5.14	5.09	4.97	4.79	4.89	5.13	3.47	3.11	3.2	4.4
U	1.37	1.41	1.35	1.32	1.35	1.38	0.89	0.83	0.89	1.21
Isotopes (MC-ICP-MS or TIMS)										
$^{87}Sr/^{86}Sr$		0.703397	0.703366	0.703346	0.703352	0.703387	0.703269	0.703266	0.703249	0.703353
2SE		0.000006	0.000008	0.000009	0.000008	0.000006	0.000007	0.000007	0.000007	0.000006
$^{143}Nd/^{144}Nd$		0.512927	0.512945	0.512941	0.512942	0.512931	0.512957	0.512969	0.512973	0.512945
2SE		0.000006	0.000003	0.000004	0.000004	0.000008	0.000007	0.000006	0.000003	0.000005
$^{206}Pb/^{204}Pb$	18.5439	18.5396	18.544	18.5435	18.5431	18.5441	18.4845	18.4643	18.4672	18.5339
2SE										
$^{207}Pb/^{204}Pb$	15.5601	15.5554	15.5587	15.5581	15.5578	15.56	15.5422	15.5435	15.5464	15.559
2SE										
$^{208}Pb/^{204}Pb$	38.4384	38.4212	38.4347	38.433	38.432	38.4384	38.3483	38.3484	38.3587	38.4255
2SE										

*total Fe given as Fe_2O_3. Errors on isotope ratios are within-run 2 SE.

Table 4-1. Continued.

No.	31	32	33	34	35
Sample	Ho-5	Kr-4	Kr-7	Kr-8	Kr-18
Type	Andesite	Andesite	Andesite	Andesite	Andesite
Latitude (°N)	45°09'46"	45°11'01"	45°11'03"	45°11'03"	45°10'59"
Longitude (°E)	141°15'57"	141°13'26"	141°13'07"	141°13'07"	141°11'38"
Laboratory	Okayama	Okayama	Okayama	Okayama	Okayama
Major elements (wt. %)					
SiO_2	59.58	59.5	59.89	61.25	60.4
TiO_2	0.79	0.8	0.76	0.7	0.77
Al_2O_3	17.51	17.56	17.66	16.87	17.77
Fe_2O_3*	6.04	6.23	5.8	5.44	5.75
MnO	0.11	0.12	0.11	0.1	0.11
MgO	3.47	3.58	3.22	2.9	3.1
CaO	6.45	6.67	6.27	5.52	6.26
Na_2O	4.23	4.23	4.25	4	4.23
K_2O	1.28	1.18	1.26	1.22	1.27
P_2O_5	0.27	0.25	0.26	0.27	0.27
total	99.73	100.13	99.48	98.29	99.93
LOI	0.18	0.21	0.43	1.76	0.76
Trace elements (ppm)					
Sc (XRF)					
V (XRF)					
Cr (XRF)	56	56.1	47.4	35.6	37.9
Co (XRF)					
Ni (XRF)	38	35	35.3	28.9	33.4
Li	8.46	8	10.1	11.9	11.5
B	7.37	7.69	9.22	9.32	9.85
Be	1.34	1.4	1.29	1.36	1.27
Rb	30	27.3	29.9	30.6	30.3
Sr	556	601	527	531	535
Y	19.1	18.8	17.3	18.7	17.6
Zr	166	162	169	168	173
Nb	6.43	6.34	6.88	6.69	6.82
Cs	0.62	0.63	1.23	1.42	1.48
Ba	310	306	311	338	317
La	19.2	18.8	19.4	21.2	20.2
Ce	39.5	39.7	39	42.3	40.2
Pr	4.5	4.45	4.62	4.63	4.61
Nd	18.2	18.7	18.2	18.5	18.4
Sm	3.67	3.96	3.71	3.8	3.72
Eu	1.19	1.31	1.17	1.14	1.19
Gd	3.69	3.89	3.75	3.87	3.75
Tb	0.56	0.58	0.57	0.56	0.56
Dy	3.57	3.7	3.43	3.38	3.37
Ho	0.71	0.77	0.7	0.71	0.7
Er	2.12	2.25	2.1	2.03	2.09
Tm	0.31	0.34	0.31	0.31	0.31
Yb	2.14	2.27	2.06	2.05	2.08
Lu	0.33	0.35	0.31	0.32	0.31
Hf	3.63	3.61	3.72	3.79	3.72
Ta	0.5	0.5	0.52	0.57	0.52
Pb	4.16	4.71	4.74	5.65	4.85
Th	3.5	3.3	3.75	4.22	3.78
U	0.97	0.98	1.02	1.13	1.01
Isotopes (MC-ICP-MS or TIMS)					
$^{87}Sr/^{86}Sr$	0.703293	0.703277	0.703291	0.703315	0.703285
2SE	0.000009	0.000007	0.000007	0.000007	0.000007
$^{143}Nd/^{144}Nd$	0.512968	0.512959	0.512941	0.512948	0.512962
2SE	0.000004	0.000007	0.000007	0.000006	0.000004
$^{206}Pb/^{204}Pb$	18.4908	18.482	18.4979	18.5042	18.5008
2SE					
$^{207}Pb/^{204}Pb$	15.5487	15.55	15.5494	15.554	15.552
2SE					
$^{208}Pb/^{204}Pb$	38.3756	38.3717	38.3834	38.3944	38.3911
2SE					

*total Fe given as Fe2O3. Errors on isotope ratios are within-run 2 SE.

Table 4-2. Th and U isotopic compositions and concentrations of the dacite and andesite lavas.

No.	Sample	Type	Th ppm	U ppm	(^{230}Th/^{232}Th)	(^{238}U/^{232}Th)	(^{234}U/^{238}U)	Age corrected (^{232}Th/^{230}Th)*
20	Y-1	Dacite	4.80	1.37	0.902	0.866	0.999	0.832
22	Y-3	Dacite	4.61	1.33	0.904	0.876	1.001	0.836
26	Y-26	Dacite	4.61	1.33	0.906	0.879	0.999	0.840
27	Af-1B	Andesite	3.27	0.93	0.938	0.863	1.002	0.876
28	Af-4B	Andesite	2.88	0.84	0.938	0.881	1.002	0.881
29	Af-7B	Andesite	2.99	0.85	0.932	0.857	1.002	0.867
30	Af-9	Andesite	4.22	1.19	0.907	0.859	0.998	0.838
31	Ho-5	Andesite	3.29	0.95	0.942	0.879	1.002	0.885
32	Kr-4	Andesite	3.00	0.88	0.937	0.888	1.002	0.882
33	Kr-7	Andesite	3.55	1.01	0.932	0.861	1.002	0.869
34	Kr-8	Andesite	3.82	1.09	0.941	0.866	1.003	0.880
35	Kr-18	Andesite	3.57	1.02	0.932	0.865	1.001	0.870

*Correcting ages for the dacite and the andesite lavas are 35.5 ka and 34.6 ka, respectively.
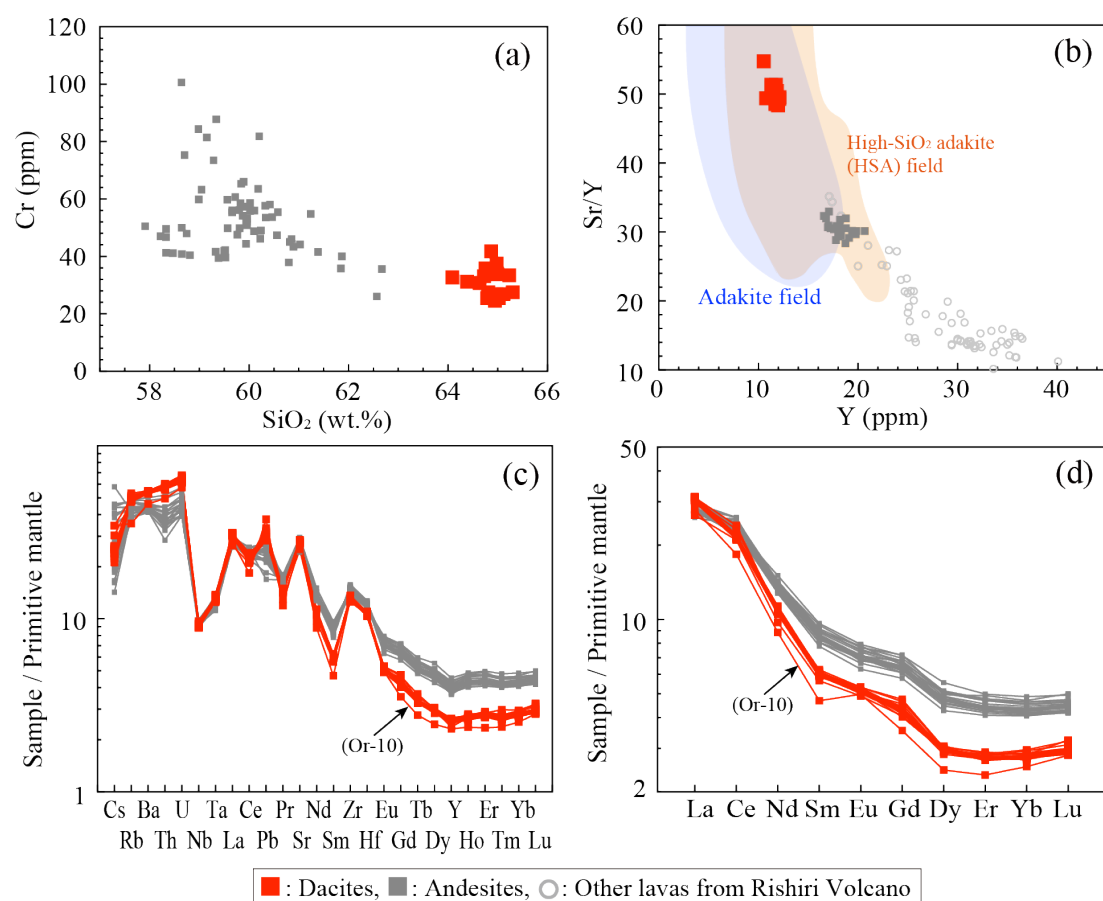
Figure 4-5 Composition of the dacite lavas from the Rishiri Volcano, shown in (a) Cr–SiO$_2$ diagram, (b) Sr/Y–Y diagrams, (c) primitive mantle-normalised diagram of trace element concentration, and (d) primitive mantle-normalised rare-earth element concentration. In (b), the compositional fields of the High-SiO$_2$ adakite (HSA) and adakite are taken from Martin et al. (2005) and Defant and Drummond (1990), respectively. In (a)–(d), the data of Ishizuka (2000) and Taniuchi (2020a) are also shown. In (c) and (d), the trace element concentrations of primitive mantle are from Sun and McDonough (1989).
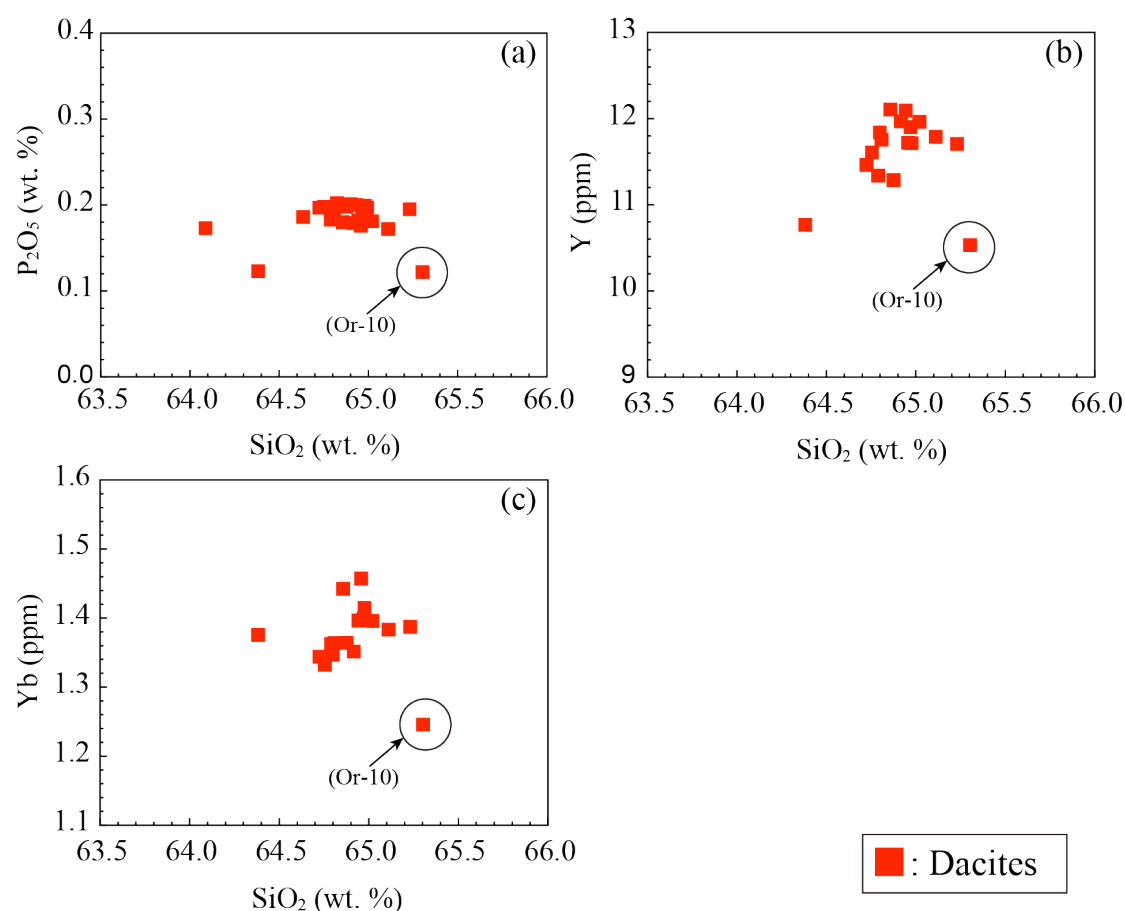
Figure 4-6 The whole-rock compositions of the dacite lavas from Rishiri Volcano, shown in (a) P_2O_5–SiO_2 diagram, (b) Y–SiO_2 diagram, and (c) Yb–SiO_2 diagram. The outlying dacite sample (Or-10) with a positive Eu anomaly in Fig. 4-5d has exceptionally low P_2O_5, Y, and Yb contents compared with those of other dacite samples. This magma may have undergone additional magmatic processes, such as plagioclase accumulation and apatite fractionation.

4-6. Discussion

4-6-1. Magmatic processes in crust

All phenocrysts in the dacite lavas are clear under a polarised light microscope, and essentially homogeneous in composition or slightly normally zoned with unimodal distributions in their core composition (Fig. 4-4). In addition, sieve-textured plagioclase is not found. These observations suggest that the dacitic magma did not undergo mixing after phenocryst crystallisation. The phenocryst phases occasionally form crystal aggregates, showing evidence of simultaneous growth, while no Eu anomaly is evident in whole-rock samples (Fig. 4-5d). In addition, the $^{87}Sr/^{86}Sr$ ratios of the plagioclase phenocrysts (Table 4-3) are identical to those of the host lavas (Fig. 4-7a). This indicates that all the phenocrysts were grown *in situ* in the dacitic magmas with no Eu anomaly.

54

Table 4-3. Results of Sr isotopic analyses for plagioclase phenocrysts in the dacitic lavas.

No.	1	2	3	4
Sample	OS-2 pl1	OS-2 pl2	OC-5 pl1	OC-5 pl2
Type	Dacite	Dacite	Dacite	Dacite
$^{87}Sr/^{86}Sr$	0.703353	0.703354	0.703342	0.703335
2SE	0.000009	0.000015	0.000012	0.000011
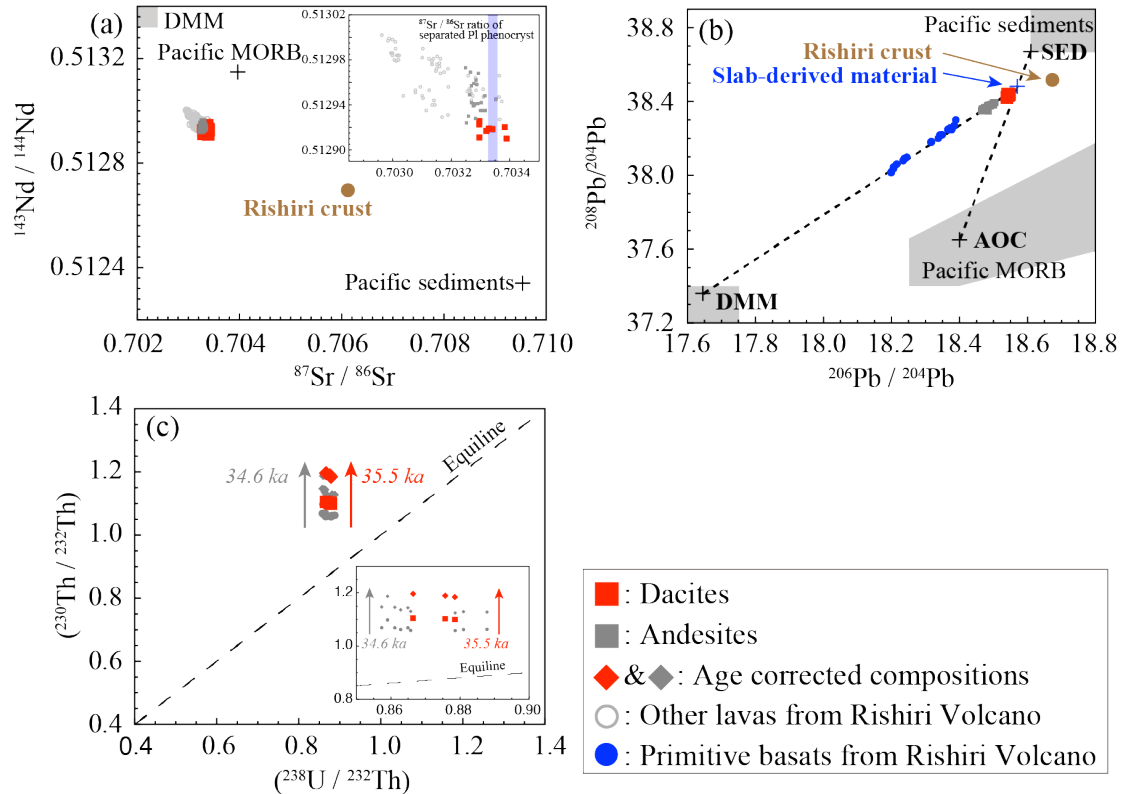
Figure 4-7 Composition of the dacite lavas from the Rishiri Volcano, shown in (a) the $^{143}Nd/^{144}Nd$–$^{87}Sr/^{86}Sr$ diagram, (b) the $^{208}Pb/^{204}Pb$–$^{206}Pb/^{204}Pb$ diagram, and (c) the U-Th equiline diagram. In (a) and (b), blown filled circles show the composition of crustal xenolith from the Rishiri Volcano (Kuritani et al., 2005). In (a), the $^{87}Sr/^{86}Sr$ ratios of the plagioclase phenocrysts are also shown. In (a) and (b), the compositional fields of the depleted MORB mantle (DMM) are taken from Zindler and Harf (1986), and those of the Pacific sediments and Pacific MORB are from Kimura and Yoshida (2006). The representative compositions of the Pacific sediments (SED), Pacific MORB (AOC), and DMM are taken from Hauff et al. (2003) and cousens and allan (1992). In (a) and (b), the data of Kuritani and Nakagawa (2016) and Kuritani et al. (2005, 2007, 2008) are also shown.

4-6-2. Water contents of the dacite

The water content of the dacitic magma is estimated using the plagioclase-melt hygrometer given in Putirka (2008). Plagioclase phenocrysts in the dacitic lavas are considered to have crystallised *in situ*, as it is observed that the lavas have no Eu anomaly (Fig. 4-5d), and because the $^{87}Sr/^{86}Sr$ ratios of the plagioclase phenocrysts are identical to those of the lavas (Fig. 4-7a). Therefore, it is assumed that the plagioclase phenocrysts with the highest An contents of 63.8 are in equilibrium with the melt that had a whole-rock composition of OS-2. The pressure condition is estimated using the compositions of the clinopyroxene and orthopyroxene phenocrysts, suggested to have grown simultaneously. By applying the two-pyroxene geobarometer given in Putirka (2008), I obtained a crystallisation pressure of 0.46 ± 0.4 GPa. The water content of the melt and the crystallisation temperature of plagioclase phenocrysts are then estimated by simultaneously solving Equations (25b) and (26) given in Putirka (2008) at a pressure of 0.46 GPa, to obtain a water content and a temperature of 5.3 ± 1.1 wt.% and 980 ºC, respectively. The water contents of the dacites are also estimated by the plagioclase-melt hygrometer given in Waters and Lange (2015), yielding 4.3 wt.%. This result is within the ranges of the estimates of 5.3 ± 1.1 wt.%, obtained by the hygrometer given in Putirka (2008).

4-6-3. Origin of the dacite

The dacitic lavas are characterised by high Sr/Y and [La/Yb]$_N$ ratios (Figs. 4-5b–d). One possible origin of dacitic melt with an adakitic signature is crystal fractionation, specifically of hornblende and garnet, from hydrous basaltic magmas (Prouteau and Scaillet, 2003) or from calc-alkaline andesite magmas (with relatively lower [La/Yb]$_N$ ratios; Fig. 4-5d) that erupted just before the dacite magmas. If this was the case, the dacitic melt would have been in equilibrium with hornblende or garnet at depth. The water content and temperature of the dacitic melt are estimated to be 5.3 ± 1.1 wt.% and 980 ºC, respectively, at 0.46 GPa, using plagioclase-melt equilibrium. Experimental studies (Prouteau and Scaillet, 2003) showed that, for a dacitic melt with major element composition similar to that of the Rishiri dacite, the melt with ~5.3 wt.% H_2O cannot be in equilibrium with hornblende unless the temperatures are lower than 930 ºC at 0.4 GPa and 900 ºC at 0.96 GPa. The melt cannot crystallize garnet at any temperatures at ≤ 0.96 GPa. Therefore, it is not likely that hornblende and/or garnet crystallised as a primary liquidus phase from the dacitic melt with ~980 ºC in the crust (< ~0.8 GPa; Niu et al., 2016) beneath Rishiri. This is supported by the absence of hornblende and garnet phenocrysts in the dacitic lavas, as well as in the calc-alkaline andesite lavas. Therefore, I conclude that the dacitic magmas were not derived from hydrous basaltic magmas or calc-alkaline andesite magmas through crystal fractionation.

It has also been recognised that felsic magmas with an adakitic signature can be produced by the partial melting of the lower part of the thick (> 30 km) crust, consisting of garnet-bearing mafic rocks (Atherton and Petford, 1993; Ma et al., 2015). However, the adakitic signature could not be

produced in the crust beneath the Rishiri Volcano, because the crust is too thin (~25 km; Niu et al., 2016) for the garnet to be stable (Rapp and Watson, 1995; Alonso-Perez et al., 2009). The isotopic composition of dacitic lavas are found to be significantly different from the crustal xenoliths at the volcano (Kuritani et al., 2005; Figs. 4-7a and 4-7b), also negating the potential for the dacite magma to have originated from partial melting of the crust.

4-6-4. The separation of slab-derived supercritical liquid

Based on these considerations, I conclude that the dacitic melt with adakitic signature could not have been derived from crustal magmatic processes but instead originated in the upper mantle. As it is unlikely that primary melt with dacitic composition was produced by the partial melting of mantle peridotite, the possible origin of the dacitic melt would be (1) partial melting of the subducting slab (Martin, 1986; Defant and Drummond, 1990; Martin et al., 2005), (2) partial melting of a pyroxenite mantle source with an influx of slab-derived fluid (Straub et al., 2005; Straub et al., 2008), or (3) separation of slab-derived supercritical liquid (Shen and Keppler, 1997; Bureau and Keppler, 1999; Kawamoto et al., 2012). These hypotheses are evaluated below.

If scenario (1) was the case, extremely high temperature would have been required to melt the slab, because the depth of the slab is ~300 km beneath Rishiri. Experimental studies have suggested that extremely high temperatures of >1300 ºC are required to induce hydrous partial melting of the slab at the depth of 300 km (Kessel et al., 2005; Mibe et al., 2011). However, the slab surface temperature are estimated to be ~1000 ºC at 300 km depth, based on the extrapolation of the subduction thermal model (D80; Syracuse et al., 2010). In addition, evidence for temperature elevation in the slab, such as a slab window or slab tear, has not been found beneath the Rishiri Volcano (Miller et al., 2006; Kennett et al., 2010), suggesting that this scenario (1) is unlikely.

In scenario (2), the generation of dacitic melt is explained by partial melting of silica-excess pyroxenites, formed by the reaction of a peridotite mantle with infiltrated silicic slab components, in the sub-arc mantle (Straub et al., 2008; Straub et al., 2011). In this case, it is expected that the primary dacitic melt would have high Ni contents (Straub et al., 2008; Straub et al., 2011). However, the Rishiri dacites have significantly lower Ni contents of 26–39 ppm than those of mantle-derived primary magma (>~200 ppm). High-Ni olivines, that characteristically occur in magmas generated by the melting of a pyroxenite mantle source (Straub et al., 2008; Straub et al., 2011), are also not observed in the dacite lavas. The Pb isotopic ratios of the dacite lavas can be explained by binary mixing between AOC component and SED component with little contribution of the depleted-MORB mantle (DMM) component (Fig. 4-7b); this observation also suggests that the mantle component was not significantly involved in the genesis of the dacites. For these reasons, I conclude that scenario (2) cannot explain the genesis of the dacitic magmas at Rishiri.

At the depth of the subducting slab of ~300 km at the Rishiri Volcano, supercritical liquid rather than aqueous fluid is expected to be released from the slab (Kessel et al., 2005; Mibe et al., 2011; Kawamoto et al., 2012). In fact, some primitive alkali basalt magmas at Rishiri are considered to have been generated by the melting of the source mantle with an influx of slab-derived supercritical liquid (Kuritani et al., 2008; Kuritani and Nakagawa, 2016). These alkali basalt lavas show ^{230}Th-excesses with respect to ^{238}U (Kuritani et al., 2008). This is contrary to the U-excess signatures of frontal-arc lavas, which reflect a much higher mobility of U in slab-derived aqueous fluids than Th. Slab-derived supercritical liquids produce a ^{230}Th-excess (Kuritani et al., 2008) because of a preferential partition of Th relative to U (Kessel et al., 2005; Portnyagin et al., 2007) during the dehydration of the subducting slab. The dacite lavas, as well as the preceding calc-alkaline andesitic lavas, show Th-excesses (Fig. 4-7c), which is consistent with the inference that slab-derived supercritical liquid was involved in the generation of both the dacite and andesite magmas. The eruption ages of the andesitic and dacitic lavas of 34.6 ± 3.0 and 35.5 ± 1.4 ka, respectively, and the stratigraphic relationship between the two indicate that the andesitic magmas erupted just before the dacitic magmas. In addition, the primitive basaltic magmas involved in the generation of the calc-alkaline andesitic magmas are considered to have been generated by the influx of slab-derived fluids into the source mantle as described in the Chapter 3. These observations suggest that, in the upper mantle directly under the volcano, slab-derived fluid was present alongside the dacitic melt. As aqueous fluid and hydrous silicate melt cannot be produced from a subducting slab at an identical temperature (Kessel et al., 2005; Mibe et al., 2011), these two components were most plausibly generated by the separation of ascending slab-derived supercritical liquid in the subarc mantle (i.e., scenario 3). The similarity of ^{238}U–^{230}Th disequilibria in the andesite and dacite lavas is also consistent with the derivation of andesites and dacites by essentially the same slab-derived supercritical liquid. The adakitic signature of the dacites (i.e., the silicate melt component in the slab-derived supercritical liquid) is considered to reflect the presence of residual garnet in the slab, because the basaltic oceanic crust is in the eclogite-facies field at a depth of ~300 km (Hucker et al., 2003).

From these considerations, this study concludes that the dacitic melt was most plausibly produced by the separation of slab-derived supercritical liquid (Shen and Keppler, 1997; Bureau and Keppler, 1999; Kawamoto et al., 2012), rather than by the partial melting of the subducting slab (Martin, 1985; Defant and Drummond, 1990; Martin et al., 2005) or the partial melting of the pyroxenite mantle (Straub et al., 2008; Straub et al., 2011). Slab-derived supercritical liquid ascending in the mantle wedge separated to produce hydrous melt and aqueous fluid beyond depths corresponding to the critical point. The former is represented by the dacitic melt and the latter induced generation of the primary basaltic magma involved in the generation of the calc-alkaline andesite magma (Fig. 4-8). It is difficult to estimate the depth at which the superciritical liquid was

separated into the aqueous fluid and hydrous felsic melt, because of the scarcity of experimental studies. However, the high-K/Na alkali basalt magmas (Nozuka lavas) at Rishiri are considered to have been generated at ~2.3 GPa through an influx of slab-derived supercritical liquid into the melting region (Kuritani and Nakagawa, 2016). This observation suggests that the depth of the critical point for the supercritical liquid would have been shallower than the depth corresponding to ~2.3 GPa. If so, the separation of the slab-derived supercritical liquid for the dacite magmas might have occurred at depths corresponding to < ~2.3 GPa.
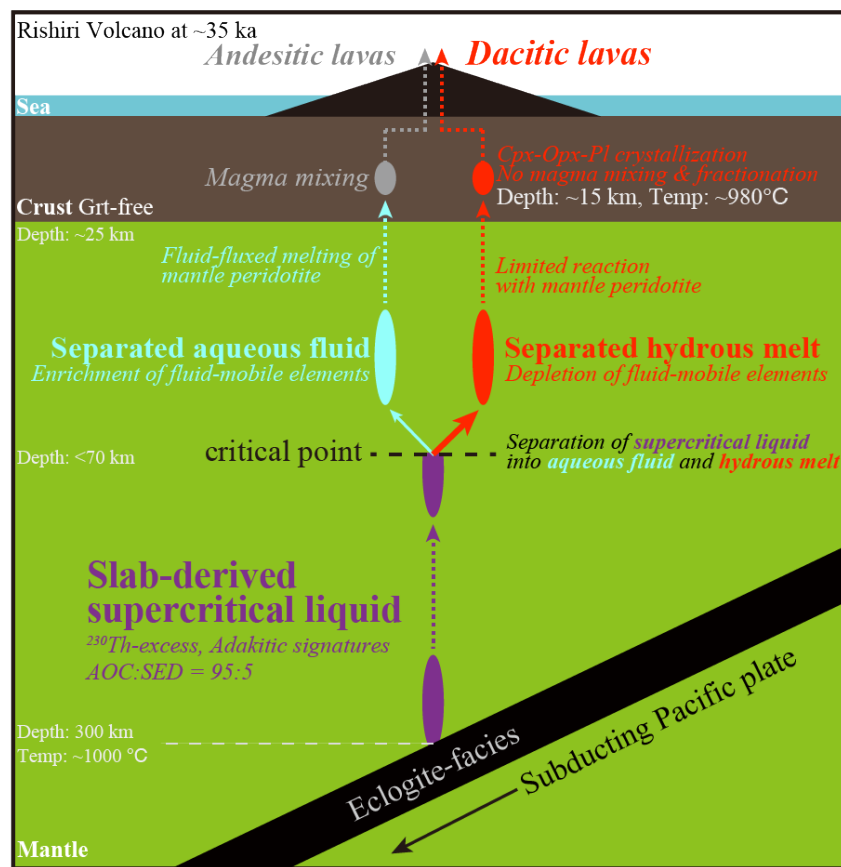
Figure 4-8 Schematic of the dacite magma generation at the Rishiri Volcano. See text for details.

The trace element compositions of slab-derived supercritical liquid are estimated using the compositions of the slab and the bulk partition coefficients of the elements between the slab and the supercritical liquid given in Kessel et al. (2005). The trace element compositions of the slab, at which the slab-derived materials (hydrous melt or supercritical liquid) are released, are obtained using the constraint of Pb isotopic ratios. The relative contribution of the sediment (SED) and the altered oceanic crust (AOC) components to the slab-derived materials can be estimated using the Pb concentration and the Pb isotopic ratio of the depleted MORB mantle (DMM) of Cousens and Allan (1992), those of SED and AOC component of Haff et al. (2003), and the Pb

isotopic ratios of the dacitic lavas, from which a mixing proportion of AOC and SED of 5:95 was obtained. The trace element contents of the slab are then calculated using the mixing ratio and the trace element contents of the AOC (Pearce and Parkinson, 1993) and SED (Taylor and McLennan, 1085). The trace element contents of the slab-derived materials are finally estimated using the compositions of the slab and the partition coefficients of the elements of Kessel et al. (2005), and are displayed in a primitive mantle-normalized trace element concentration diagram (Table 4-4 and Fig. 4-9). The concentrations of fluid-mobile elements, such as Rb, Sr, Ba, and Pb, are significantly depleted in the dacitic lavas compared with the estimated concentrations of possible slab-derived supercritical liquid (Fig. 4-9). For example, the Rb/Zr and Pb/Hf ratios of the dacitic lavas of ~0.2 and ~1.6, respectively, are much lower than those of the supercritical liquid at 1.5 and 5.3, respectively. These features are consistent with preferential partitioning of fluid-mobile elements into an aqueous fluid relative to the remaining hydrous silicate melt during the separation of supercritical liquid (Kawamoto et al., 2014), although these features may also be attributed to a low content of fluid-mobile elements in the slab-derived supercritical liquid, which would have resulted from depletion in the subducting slab by removal through dehydration processes before reaching ~300 km depth.

Based on experimental studies on the behavior of slab-derived supercritical liquid (Shen and Keppler, 1997; Bureau and Keppler, 1999), Kawamoto et al. (2012) suggested the generation of two different types of primary mafic magmas in the mantle wedge beyond depths corresponding to the critical points; mafic magma from melting of the mantle with an influx of separated aqueous fluid and mafic magma from a reaction of separated hydrous melt with mantle peridotite. The occurrence of mafic magmas of these origins was suggested at the Mariana arc (Tamura et al., 2014). As such, this study suggests for the first time that hydrous felsic melt generated through the separation of slab-derived supercritical liquid can erupt without significant interaction with the mantle wedge.

Table 4-4. Estimated composition of slab-derived supercritical liquid.

Elements	SCF (ppm)	Elements	SCF (ppm)	Elements	SCF (ppm)
Rb	435	Pr	-	Dy	1.35
Ba	6317	Sr	8538	Y	10.2
Th	42.0	Nd	162	Ho	-
U	4.82	Sm	10.2	Er	0.41
Nb	20.5	Zr	292	Tm	-
Ta	1.19	Hf	11.8	Yb	0.28
La	294	Eu	2.08	Lu	0.03
Ce	371	Gd	3.79		
Pb	62.7	Tb	-		
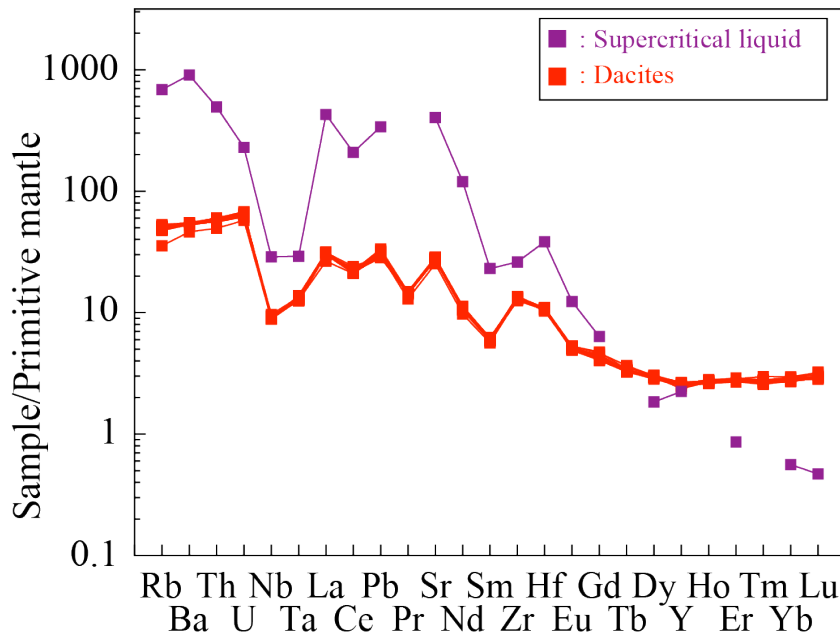
Figure 4-9 Primitive mantle-normalized trace element concentrations of possible slab-derived supercritical liquid and hydrous melt, along with those of the dacite. The trace element concentrations of the primitive mantle are taken from Sun and McDnough (1989).

4-6-5. Implications

Felsic magmas with high Sr/Y and [La/Yb]$_N$ ratios have occurred as adakites in modern hot subduction zones (Defant and Drummond, 1990). It has been experimentally suggested that the minimum depth at which a supercritical liquid can occur in subducting slabs tends to become shallower with increasing proportions of sediment components in the slab (Kawamoto et al., 2012). The proportion of sediment components in adakites, such as those from the Southwestern Japan arc above the Philippine Sea slab, are ~40 % (Pineda-Velasco et al., 2019), significantly higher than studied dacites of ~5 % above the Pacific slab. Moreover, the Philippine Sea slab is significantly hotter than the Pacific slab (Peacock and Wang, 1999). Thus, the supercritical liquid may have occurred at much shallower levels in the hot modern subducting slabs such as the Philippine Sea slab than the Pacific slab beneath the Rishiri Volcano. If so, some modern adakitic magmas may represent felsic magmas generated through the separation of slab-derived supercritical liquid.

Supercritical liquid may ascend in the mantle wedge more effectively than silicate melt, because of the reduced viscosity. The large ^{230}Th-excess (Fig. 4-7c) of dacites from the Rishiri Volcano is consistent with the rapid transport of slab materials as supercritical liquid, although the timescale of transport cannot be estimated due to the uncertainty of the U/Th ratio of the slab source materials. I propose that slab-derived supercritical liquid is an efficient transport medium for silicate-rich components from the subducting slab through the mantle wedge to the surface, and it may have contributed to the growth of the continental crust.

4-7. Conclusion

       To understand the nature and behavior of slab-derived supercritical liquid, I carried out a detailed petrological and geochemical study on the adakitic dacite from the volcano. I reached the following conclusions:

1. The dacitic lavas characterized by high-Sr/Y and La/Yb ratios (i.e. adakitic signature), no Eu anomaly, and no evidence of magma mixing. The petrography and absence of Eu anomaly negates a primary role of fractional crystallization and cumulation of phenocrysts in the magma genesis.

2. The adakitic signature cannot be produced by crustal melting, because the underlying crust is too thin for garnet to be stable. Moreover, the adakitic dacites cannot be produced by slab melting, because extremely high temperatures with > 1300 $^{\circ}$C is required to melt the slab at ~300 km depth.

3. The petrological and geochronological observations suggest that the slab-derived dacitic melt coexisted with slab-derived aqueous fluid, which produced the primitive end-member magma of the calc-alkaline andesite, in the upper mantle beneath Rishiri at ~35 ka. Therefore, the dacitic magma might represent hydrous melt, which was separated from the ascending slab-derived supercritical liquid above the depth corresponding to the critical point, leaving behind fluids that induced the generation of the primitive basaltic magma.

Chapter 5. Generation of primary magma in the mantle: Constrains from the basaltic magmas

Abstract

It has been known that primary basaltic magmas in subduction zones show chemical diversity even in an individual volcano. In this chapter, I aim to elucidate the dominant factors that determine the chemical composition, especially the Na/K ratio, of primary basaltic magmas by conducting a comparative petrological study of high-Na/K and low-Na/K basaltic lavas from Rishiri Volcano, southern Kuril Arc. The whole-rock SiO_2 content of the high-Na/K Horyosawa lava, the main target of this chapter, ranges from 51.9–53.4 wt.%. The petrological and geochemical features of the lava indicate that the effects of magma mixing and assimilation of crustal materials were limited and the low SiO_2 magmas were essentially derived through olivine fractionation from the primary magma. The primary magma is estimated to have been generated by 2.3% partial melting of the source mantle with 0.102 ± 0.033 wt.% H_2O at 1290 ± 26 °C and 2.30 ± 0.02 GPa. By comparing the results from the high-Na/K Horyosawa lavas to the published results from the low-Na/K Nozuka lava, I find that the slab-derived fluids involved in their formation were supercritical liquids with similar composition when released from the subducting slab, while their composition changed to different Na/K ratios before magma generation. The estimated magma generation conditions of both lavas show that the Horyosawa primary magma generated at shallower mantle than the Nozuka primary magma, which suggests that the separated aqueous fluid with lower-Na/K ratio and supercritical liquid with higher-Na/K ratio were involved in the generation of the former and latter, respectively. It is also demonstrated that elemental partitioning during the separation of slab-derived supercritical liquid into aqueous fluid and hydrous melt induced chemical diversity of primary basaltic magma in single volcanic system.

5-1. Introduction

Basaltic magmas in subduction zones have been known to be variable in terms of major elements, trace elements, and isotopic compositions. These features have been recognized as across-arc and along-arc compositional variations (e.g., Kuno, 1966; Gill, 1981: Ishikawa and Nakamura, 1994; Taylor and Nesbitt, 1998). It has been thought that the compositional variation of basaltic magma would be caused by multiple factors, such as crustal thickness (e.g., Condie and Potts, 1969; Miyashiro, 1974), degree of partial melting (e.g., Sakuyama and Nesbitt, 1986; Tatsumi et al., 1983), and temperature and pressure conditions of magma generation region (e.g., Taylor, 1976; Hirose and Kushiro, 1993). Furthermore, it has been also known that the differences in the nature and composition of slab-derived water-rich material contribute to the chemical diversity of primary basaltic magmas (e.g., Gill, 1981; Elliott, 2003; Kessel et al., 2005; Portnyagin

et al., 2007). In addition to the along-arc and across-arc compositional variation, chemical diversity has been also recognized even in a single volcanic system (Le Voyer et al., 2010; Tamura et al., 2014; Kuritani and Nakagawa, 2016). Le Voyer et al. (2010) investigated the high-Fo olivine-hosted primary melt inclusions in the basaltic andesites from Mount Shasta, Cascades Arc, and recognized the chemical diversity of their compositions. They pointed out the involvement of two contrasting H_2O-rich components with different mixing ratios of sediment melt and dehydration fluid as the cause of the chemical diversity. Tamura et al. (2014) clearly showed that two types of primary magma with different trace element patterns were produced beneath the Pagan Volcano, Mariana Arc, and it was suggested that the differences were induced by whether the slab-derived agents were dominated by hydrous fluid or sediment melt. Kuritani and Nakagawa (2016) found that the low-Na/K type basaltic magmas of the Rishiri Volcano can be classified into two groups based on systematic differences in isotopic ratios and Sr content, and they attributed the diversity to the compositional variation in the slab-derived fluids. Because of the paucity of case studies, however, it remains open to debate the factors responsible for the compositional diversity of primary magmas at a single volcano.

In this context, I conducted a petrological and geochemical study on alkali basaltic lavas from the Rishiri Volcano, northern Hokkaido, Japan. The volcano is characterized by the coexistence of calc-alkaline andesites to dacites, tholeiitic andesites to dacites, as well as basalts (Katsui, 1953; Kobayashi, 1989; Ishizuka and Nakagawa, 1999). The basaltic magmas are divided into the high-Na/K type and low-Na/K type based on the whole-rock composition (Ishizuka and Nakagawa, 1999). However, the factors that determine the Na/K ratio of the primary magma have not been clarified to date.

In this chapter, I focus on the Horyosawa lava (high-Na/K type basalt), which has not been studied for their petrogenesis, and conducted the petrological and geochemical analyses to clarify the magmatic process and magma generation conditions. Then, I compare the results of the Horyosawa lava with that of the Nozuka lava (low-Na/K type basalt) which has been analyzed in detail in the previous study (Kuritani and Nakagawa, 2016), to elucidate the controlling factors causing the Na/K variation.

5-2. Geological and petrological background

5-2-1. Horyosawa lava

Horyosawa lavas are exposed in valleys at the northeastern flank of the volcano (Fig. 5-1) and are classified into the Early-2 stage activity (~40–70 ka; Ishizuka and Nakagawa, 1999). In this chapter, 16 samples were collected from the lava flows. The whole-rock major elements, trace elements, and Sr-Nd-Pb isotopic ratios were analyzed for all of the samples.
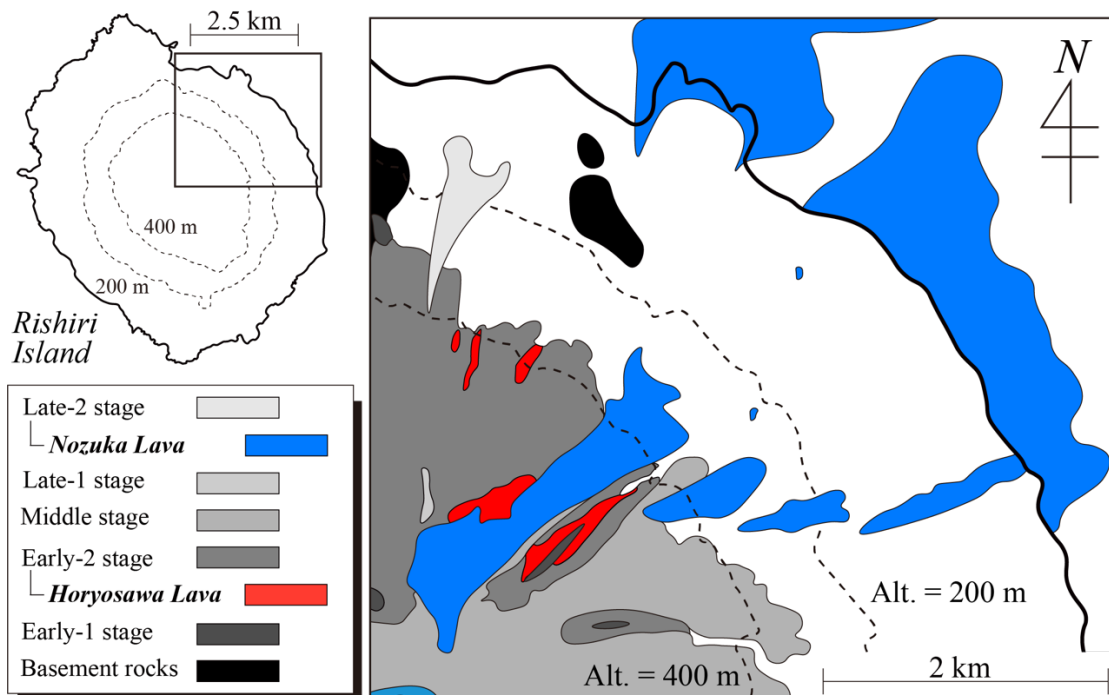
Figure 5-1. Geological map showing the Horyosawa lava (area in red) and Nozuka lava (area in blue) as given by Ishizuka (1999).

5-2-2. Nozuka lava

Nozuka lava, which is compared with the Horyosawa lava in this chapter, flowed from the summit to the northeast flank of the volcano during the Late-2 stage (Fig. 5-1; Ishizuka, 1999). The eruption age of the Nozuka lava flow has been determined to be 28,230 ± 1,020 y. BP (Miura and Takaoka, 1993) by radiocarbon dating of the wood that collected from directly under the lava flow.

Kuritani and Nakagawa (2016) conducted detailed petrological and geochemical studies on 24 samples to clarify the magmatic processes and to estimate the chemical composition and generation conditions of the primary magmas. They show that the Nozuka lava can be classified into two groups, high-Sr and low-Sr, and that primary magmas of the two groups were generated by almost identical temperature and pressure conditions. The differences in chemical and isotopic compositions between them were interpreted to the chemical diversity of slab-derived supercritical liquid involved in the primary magma generation (Kuritani and Nakagawa, 2016).

5-3. Petrography and mineral chemistry of the Horyosawa lava

The Horyosawa lava contains olivine, clinopyroxene, and plagioclase phenocrysts as shown in Fig. 5-2. The chemical compositions of each phase are shown in Fig. 5-3.
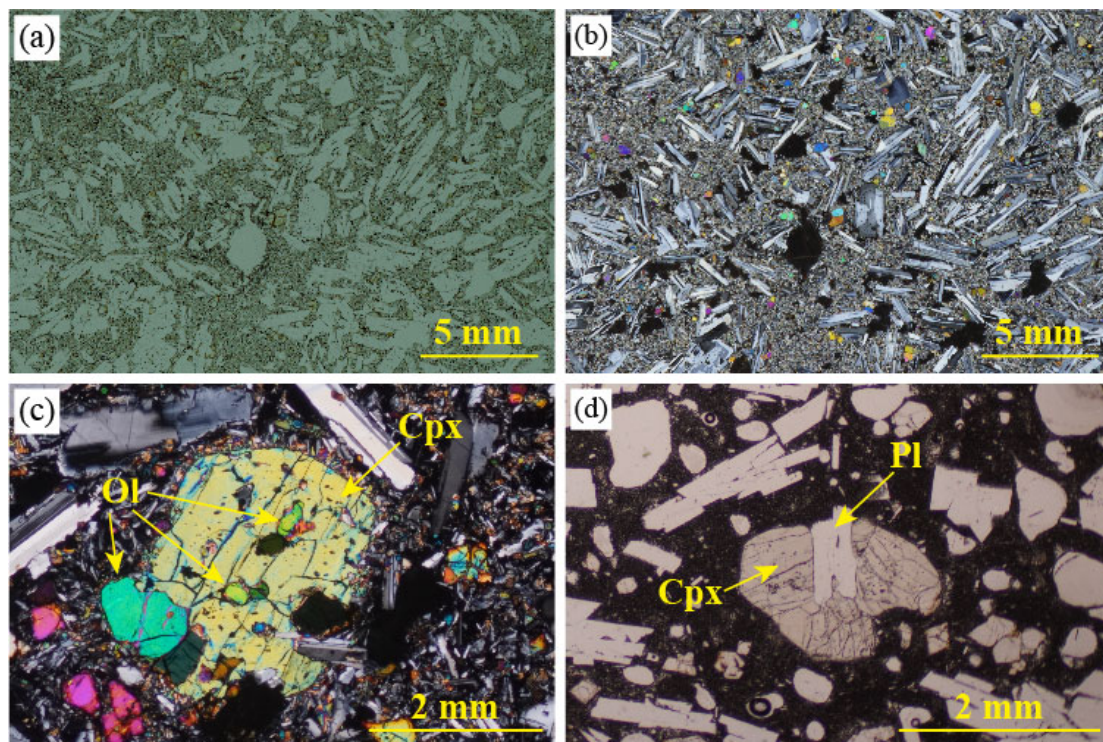
Figure 5-2. (a, b) Photomicrographs of representative samples of the Horyosawa lava, (a) parallel- and (b) cross-polarized light, respectively. (c, d) Photomicrographs of representative crystal aggregate composed of (c) olivine and clinopyroxene, and (d) clinopyroxene and plagioclase. In (c), clinopyroxene include some olivines.

5-3-1. Olivine phenocrysts

The olivine phenocrysts have euhedral outlines. The phenocrysts show normal zonation or are essentially homogeneous. The Fo (Fo = $100 \times$ Mg/(Mg + Fe)) content of the cores of the olivine phenocrysts ranges from 69–84 (Figs, 5-3a, 5-3d, and 5-3g). The distribution of the Fo content is variable with a peak at around Fo = 74–75 regardless of the whole-rock SiO_2 content, while the olivine with high-Fo (> ~80) is more common in the lower-SiO_2 samples (Figs, 5-3a, 5-3d, and 5-3g). The low-Fo (< ~75) olivine phenocrysts often form crystal aggregates with clinopyroxene and plagioclase phenocrysts. Additionally, the olivine included in the clinopyroxene phenocrysts is occasionally observed (Fig. 5-2c).

5-3-2. Clinopyroxene phenocrysts

The clinopyroxene phenocrysts show euhedral to subhedral outlines and almost all of them form crystal aggregate with plagioclase (Fig. 5-2d). Additionally, some clinopyroxenes include olivine (Fig. 5-2c). The Mg# (Mg# = $100 \times$ Mg/(Mg + Fe)) of the cores of the clinopyroxene phenocrysts ranges from 74–80 and there is no systematic variation with the whole-rock composition (Figs. 5-3b, 5-3e, and 5-3h).
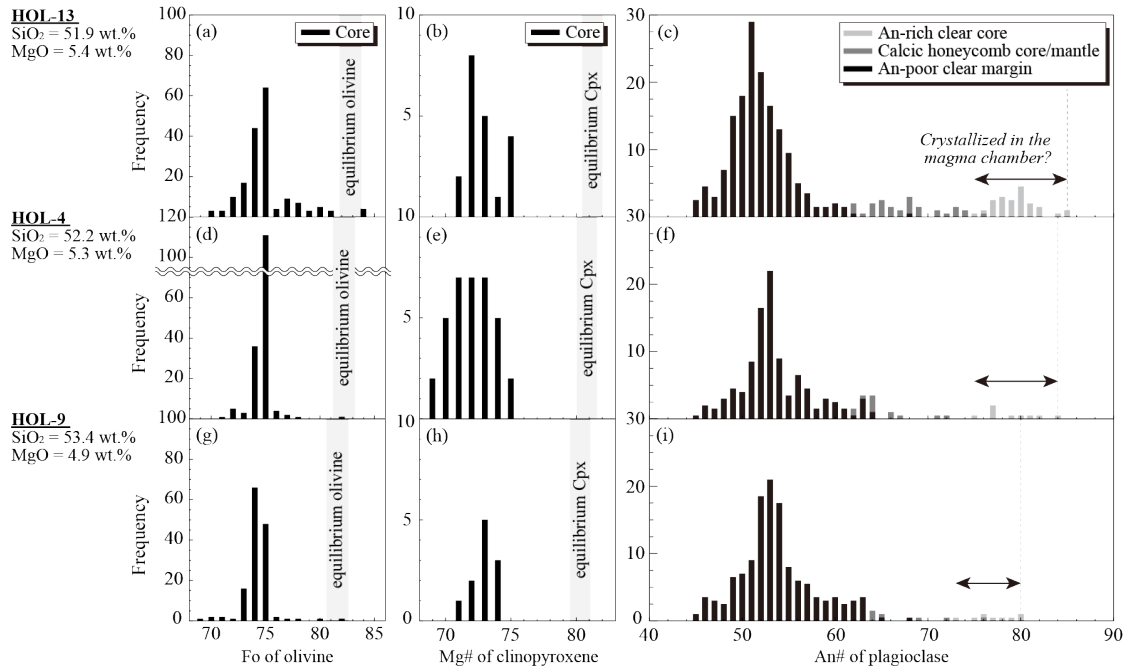
Figure 5-3. Histograms of (a, d, g) Fo contents of the cores of olivine phenocrysts, (b, e, h) Mg# of the cores of clinopyroxene phenocrysts, and (c, f, i) An# contents of the An-rich clear cores, calcic honeycomb core/mantle, and An-poor clear margin of plagioclase phenocrysts in (a–c) HOL-13, (d–f) HOL-4, and (g–i) HOL-9 of the Horyosawa lava. In (a, b, d, e, g, h), Fo contents and Mg# that is in equilibrium with whole-rick composition are also shown.

5-3-3. Plagioclase phenocrysts

Plagioclase is the dominant phase in the Horyosawa lava flows and its abundance reaches ~40 vol.% (Table 5-1). Based on the classification of the internal regions, plagioclase phenocrysts can be divided into the following four types (Fig. 5-4). Type-1 consists of An-rich clear core and An-poor clear margin (Figs. 5-4a and 5-4b). Type-2 is composed of An-rich clear core, calcic honeycomb mantle around the core, and outermost An-poor clear margin (Figs. 5-4c and 5-4d). Type-3 has a calcic honeycomb core in the center surrounded by An-poor clear margin (Figs. 5-4e and 5-4f). Type-4 does not show a distinct core and consists only of An-poor clear margin (Figs. 5-4g and 5-4h).

The characteristics of each internal region comprising the plagioclase are described below. An-rich clear core shows a euhedral outline and does not contain glass inclusions or mineral inclusions (Figs. 5-4a–5-4d). It is generally homogeneous in terms of chemical composition and show high An# content (An# = $100 \times Ca/(Ca + Na + K)$; > ~75; 4c, 4f, 4i). The calcic honeycomb core/mantle essentially has a euhedral shape, but some of the phenocrysts compose of crystal aggregate with olivine and clinopyroxene and show euhedral to subhedral outline. They typically have a honeycomb texture with glass inclusions (Figs. 5-4c–5-4f) and show middle An# contents

67

(a) Type-1

An-rich clear core (An# > ~75*)
*in the most mafic sample: >80)

An-poor clear margin (An# < ~65)

(b) BSE of Type-1

An56

An86

0.2 mm

(c) Type-2   Calcic honeycomb mantle (An# =62–76)

An-rich clear core (An# > ~75*)
*in the most mafic sample: >80)

An-poor clear margin (An# < ~65)

(d) BSE of Type-1

An67

An51

An79

0.1 mm

(e) Type-3

Calcic honeycomb core
(An# = ~62–76)

An-poor clear margin (An# < ~65)

(f) BSE of Type-2

An50

An69

0.2 mm

(g) Type-4

An-poor clear margin (An# < ~65)

(h) BSE of Type-3

An52   An52

An51   An53

An50

An52

0.5 mm

Figure 5-4. Schematic illustration and representative zoning in the plagioclase phenocrysts of (a, b) Type-1, (c, d) Type-2, (e, f) Type-3, and (g, h) Type-4. In (a, c, e, g), the shading roughly corresponding to colors in BEI's. The plagioclase numbers for each BEI are (a) Pl88-HOL-13, (b) Pl77-HOL-1, (c) Pl100-HOL-13, and (d) Pl15a–15f-HOL-13.

68

of ~62–76 (Figs. 5-3c, 5-3f, 5-3i). An-poor clear margin is homogeneous and shows the lowest An# contents (< ~65; Figs. 5-3c, 5-3f, 5-3i). This region has a basically euhedral and elongated shape, while that in the crystal aggregate with low-Fo olivine and clinopyroxene show euhedral to subhedral outline (Figs. 5-4a–5-4f).

All types of plagioclase phenocrysts form crystal aggregates with low-Fo olivine and clinopyroxene, but their contact with mafic minerals is limited to the calcic honeycomb core/mantle and An-poor clear margin. The compositional frequency diagram for each region of plagioclase is shown in Figs. 5-3e, 5-3f, and 5-3i. The frequency peak of the An# contents of the An-poor clear margin is recognized at An# = ~52–53, while the An-rich clear core and calcic honeycomb core/mantle do not show a distinct peak. Besides, An-rich clear core is relatively more abundant in low-SiO$_2$ samples, and their highest An# content tends to be lower with increasing whole-rock SiO$_2$ content (Figs. 5-3e, 5-3f, and 5-3i).

5-4. Whole-rock composition of the Horyosawa lava

The whole-rock major and trace element concentrations and Sr-Nd-Pb isotopic ratios of the Horyosawa lava are shown in Table 5-1. The selected variation diagrams are shown in Figs. 5-5–5-9.

5-4-1. Major elements

The SiO$_2$ variation diagrams for FeO*/MgO, Na$_2$O + K$_2$O, K$_2$O, Na$_2$O/K$_2$O, and Na$_2$O are shown in Figs. 6a–6e, respectively, with the chemical composition of other lavas from the Rishiri Volcano. The SiO$_2$, Na$_2$O + K$_2$O, and K$_2$O contents and FeO*/MgO ratio of the Horyosawa lava range 51.8–53.5, 5.0–5.3, and 0.7–0.9 wt.% and 1.6–1.8, respectively. The lavas are classified as a tholeiitic series on Miyashiro's diagram (Miyashiro, 1974; Fig. 5-5a), and alkaline and medium-K series on the classification scheme of Miyashiro (1978; Fig. 5-5b) and Peccerillo and Taylor (1976; Fig. 5-5c), respectively. The high-Na/K type basaltic lavas including the Horyosawa lava show relatively higher total alkali (Na$_2$O + K$_2$O) content and Na$_2$O/K$_2$O ratio than those of low-Na/K type basalts including the Nozuka lava (Figs. 5-5b and 5-5d). Additional SiO$_2$ variation diagrams for TiO$_2$, Al$_2$O$_3$, MgO, Na$_2$O, K$_2$O, and Na$_2$O/K$_2$O of the Horyosawa lava are also shown in Fig. 5-6 with the chemical composition of the Nozuka lava. The Al$_2$O$_3$ (Fig. 5-6b) and MgO (Fig. 5-6c) contents of the Horyosawa lava tend to decrease with increasing whole-rock SiO$_2$ content. On the other hand, with increasing SiO$_2$ content, the K$_2$O content tends to increase (Fig. 5-6e). The TiO$_2$ (Fig. 5-6a) and Na$_2$O (Fig. 5-6d) contents change little with SiO$_2$ content.

Table 5-1. Results of elemental and isotopic analyses for the Horyosawa lavas from the Rishiri.

No.	1	2	3	4	5	6	7	8
Sample	HOL-1	HOL-2	HOL-3	HOL-4	HOL-5	HOL-6	HOL-7	HOL-8
Major elements (wt.%)								
SiO_2	51.73	53.19	53.22	51.27	52.10	52.10	53.11	52.74
TiO_2	1.54	1.59	1.55	1.51	1.58	1.57	1.53	1.58
Al_2O_3	17.34	17.07	17.14	16.85	16.84	16.68	17.39	16.96
Fe_2O_3*	9.85	10.03	9.83	9.87	10.22	10.14	9.85	10.09
MnO	0.17	0.17	0.17	0.17	0.17	0.17	0.17	0.17
MgO	5.41	5.15	5.22	5.18	5.24	5.19	5.06	5.14
CaO	9.03	8.66	8.86	8.98	8.79	8.73	8.83	8.63
Na_2O	4.20	4.35	4.30	4.28	4.33	4.17	4.30	4.26
K_2O	0.72	0.85	0.83	0.81	0.85	0.85	0.81	0.83
P_2O_5	0.29	0.32	0.31	0.30	0.32	0.30	0.29	0.29
total	100.28	101.39	101.40	99.22	100.44	99.90	101.35	100.67
LOI	0.16	0.51	0.22	0.65	0.35	0.44	0.56	0.53
Trace elements (ppm)								
Sc (XRF)	28.3	30.0	31.5	30.3	30.0	26.3	29.0	28.0
V (XRF)	219	225	226	220	221	221	207	212
Cr (XRF)	82.4	64.2	77.0	69.1	68.5	65.1	67.6	63.7
Co (XRF)	33.2	35.8	35.6	35.7	35.5	36.5	34.8	36.2
Ni (XRF)	38.5	33.7	34.7	35.0	33.9	34.9	32.8	34.4
Cu (XRF)	39.5	41.5	40.2	44.8	51.7	39.3	51.5	43.4
Zn (XRF)	76.6	80.7	78.6	79.4	78.4	80.9	75.9	78.9
Li	8.23	8.16	12.64	9.50	9.04	6.97	8.97	7.06
Rb	11.0	17.2	17.1	17.0	18.1	19.6	15.6	16.2
Sr	437	428	438	434	428	424	435	428
Y	29.4	30.2	28.5	28.5	29.7	29.7	28.4	29.2
Zr	166	189	170	166	173	174	172	182
Nb	5.16	5.45	5.13	5.15	5.34	5.43	5.14	5.41
Cs	0.47	0.79	0.75	0.84	0.95	0.95	0.75	0.62
Ba	170	181	182	172	180	179	176	180
La	13.5	14.3	13.9	13.5	14.2	14.1	13.7	14.1
Ce	32.0	33.9	34.0	32.2	33.4	33.3	33.0	33.7
Pr	4.24	4.47	4.20	4.25	4.42	4.43	4.26	4.43
Nd	18.9	19.7	18.7	18.9	19.8	19.5	18.9	19.8
Sm	4.70	4.87	4.64	4.64	4.88	4.82	4.65	4.89
Eu	1.59	1.60	1.55	1.55	1.61	1.62	1.57	1.61
Gd	5.34	5.53	5.29	5.14	5.46	5.42	5.24	5.42
Tb	0.86	0.87	0.84	0.82	0.88	0.86	0.84	0.87
Dy	5.45	5.58	5.38	5.29	5.58	5.53	5.30	5.46
Ho	1.13	1.15	1.12	1.10	1.15	1.14	1.09	1.13
Er	3.35	3.43	3.28	3.26	3.37	3.40	3.26	3.38
Tm	0.48	0.50	0.47	0.47	0.49	0.49	0.48	0.49
Yb	3.18	3.28	3.10	3.07	3.26	3.21	3.14	3.19
Lu	0.48	0.49	0.46	0.47	0.49	0.49	0.48	0.48
Hf	3.64	3.86	3.67	3.70	3.87	3.86	3.69	3.88
Ta	0.36	0.39	0.37	0.36	0.38	0.39	0.37	0.40
Pb	4.45	2.88	3.04	2.76	3.26	3.35	3.13	2.91
Th	1.75	1.94	1.83	1.84	1.92	1.91	1.84	1.89
U	0.42	0.54	0.40	0.49	0.51	0.55	0.57	0.53
Isotopic ratios								
$^{87}Sr/^{86}Sr$	0.703077	0.703069	0.703076	0.703091	0.703073	0.703082	0.703068	0.703078
2se	0.000010	0.000010	0.000010	0.000011	0.000011	0.000013	0.000012	0.000010
$^{143}Nd/^{144}Nd$	0.512976	0.512982	0.512984	0.512981	0.512990	0.512982	0.512988	0.512985
2se	0.000008	0.000007	0.000008	0.000004	0.000009	0.000007	0.000007	0.000007
$^{206}Pb/^{204}Pb$	18.2871	18.2869	18.2860	18.2838	18.2846	18.2839	18.2852	18.2873
2se	0.0006	0.0007	0.0003	0.0007	0.0005	0.0005	0.0005	0.0007
$^{207}Pb/^{204}Pb$	15.5167	15.5182	15.5167	15.5167	15.5167	15.5173	15.5174	15.5168
2se	0.0005	0.0007	0.0003	0.0008	0.0004	0.0006	0.0005	0.0006
$^{208}Pb/^{204}Pb$	38.1525	38.1580	38.1545	38.1522	38.1536	38.1547	38.1558	38.1558
2se	0.0013	0.0018	0.0008	0.0027	0.0011	0.0016	0.0015	0.0016

*total Fe given as Fe_2O_3. Errors on isotope ratios are within-run 2 SE.

Table 5-1. Continued.

No.	9	10	11	12	13	14	15	16
Sample	HOL-9	HOL-10	HOL-11	HOL-12	HOL-13	HOL-14	HOL-15	HOL-16
Major elements (wt.%)								
SiO_2	53.63	53.51	51.74	51.92	51.51	52.62	51.79	51.73
TiO_2	1.56	1.54	1.48	1.39	1.50	1.52	1.54	1.51
Al_2O_3	17.24	17.16	17.47	17.65	17.41	17.50	17.28	16.88
Fe_2O_3*	9.80	9.66	9.77	9.48	9.79	10.02	10.00	10.03
MnO	0.17	0.17	0.17	0.16	0.17	0.17	0.17	0.17
MgO	4.92	5.09	5.13	5.47	5.32	5.44	5.35	5.21
CaO	8.51	8.63	9.14	9.22	9.10	8.99	9.00	8.90
Na_2O	4.32	4.31	4.26	4.35	4.34	4.25	4.29	4.43
K_2O	0.92	0.91	0.76	0.74	0.71	0.76	0.74	0.85
P_2O_5	0.33	0.32	0.30	0.28	0.30	0.31	0.30	0.32
total	101.38	101.30	100.20	100.66	100.14	101.56	100.46	100.02
LOI	0.30	0.29	0.60	0.61	1.00	0.86	1.15	0.36
Trace elements (ppm)								
Sc (XRF)	30.6	31.1	30.1	28.6	29.4	29.9	32.3	30.1
V (XRF)	220	230	216	201	213	212	215	216
Cr (XRF)	57.6	68.1	69.7	74.9	77.8	81.9	78.1	74.3
Co (XRF)	34.3	34.4	34.4	35.8	33.2	34.3	34.4	34.5
Ni (XRF)	32.3	34.4	35.0	40.4	35.8	37.0	36.0	34.9
Cu (XRF)	39.8	43.6	40.4	46.3	42.1	42.7	43.1	37.9
Zn (XRF)	78.0	80.5	72.1	70.4	74.0	76.9	76.7	76.4
Li	7.81	12.38	8.47	8.57	9.29	7.59	9.48	9.49
Rb	21.9	19.0	15.4	13.5	9.55	14.8	11.6	16.7
Sr	436	424	444	452	451	441	450	434
Y	30.3	30.2	27.8	26.2	27.8	28.9	29.3	27.8
Zr	184	173	163	148	158	163	166	171
Nb	5.64	5.44	4.85	4.58	4.96	5.09	5.27	5.23
Cs	0.98	0.51	0.83	0.68	0.49	0.79	0.66	0.41
Ba	191	199	175	163	179	179	179	176
La	14.8	14.9	13.1	12.4	13.4	13.6	14.0	13.5
Ce	34.7	34.3	31.3	29.2	31.6	32.4	32.6	32.7
Pr	4.58	4.61	4.17	3.90	4.28	4.32	4.37	4.32
Nd	20.0	20.3	18.4	17.5	19.1	19.2	19.4	19.3
Sm	4.91	4.92	4.56	4.28	4.66	4.71	4.75	4.72
Eu	1.59	1.60	1.53	1.47	1.58	1.59	1.61	1.57
Gd	5.44	5.49	5.05	4.86	5.28	5.27	5.38	5.23
Tb	0.86	0.88	0.82	0.78	0.84	0.84	0.85	0.84
Dy	5.52	5.63	5.22	4.99	5.34	5.38	5.48	5.31
Ho	1.15	1.15	1.08	1.01	1.12	1.12	1.14	1.09
Er	3.41	3.41	3.19	3.02	3.29	3.30	3.41	3.21
Tm	0.49	0.49	0.46	0.44	0.48	0.48	0.49	0.46
Yb	3.28	3.25	3.05	2.90	3.09	3.14	3.22	3.07
Lu	0.49	0.50	0.46	0.44	0.47	0.48	0.48	0.46
Hf	3.93	3.80	3.63	3.35	3.64	3.69	3.74	3.70
Ta	0.40	0.39	0.35	0.33	0.36	0.37	0.38	0.38
Pb	3.01	3.00	2.76	2.66	2.75	2.69	2.80	3.03
Th	2.05	1.97	1.77	1.67	1.80	1.81	1.83	1.82
U	0.59	0.52	0.48	0.43	0.39	0.49	0.46	0.36
Isotopic ratios								
$^{87}Sr/^{86}Sr$	0.703084	0.703083	0.703079	0.703101	0.703130	0.703106	0.703119	0.703081
2se	0.000011	0.000011	0.000010	0.000013	0.000014	0.000014	0.000010	0.000012
$^{143}Nd/^{144}Nd$	0.512981	0.512980	0.512988	0.512987	0.512991	0.512985	0.512979	0.512981
2se	0.000007	0.000008	0.000007	0.000009	0.000006	0.000011	0.000006	0.000006
$^{206}Pb/^{204}Pb$	18.3014	18.3015	18.2862	18.2915	18.2939	18.2963	18.2974	18.2987
2se	0.0004	0.0005	0.0006	0.0005	0.0016	0.0005	0.0021	0.0006
$^{207}Pb/^{204}Pb$	15.5204	15.5190	15.5168	15.5177	15.5146	15.5177	15.5189	15.5186
2se	0.0004	0.0005	0.0005	0.0005	0.0019	0.0005	0.0026	0.0005
$^{208}Pb/^{204}Pb$	38.1739	38.1710	38.1545	38.1599	38.1522	38.1632	38.1666	38.1665
2se	0.0010	0.0015	0.0015	0.0015	0.0060	0.0012	0.0084	0.0014

*total Fe given as Fe2O3. Errors on isotope ratios are within-run 2 SE.
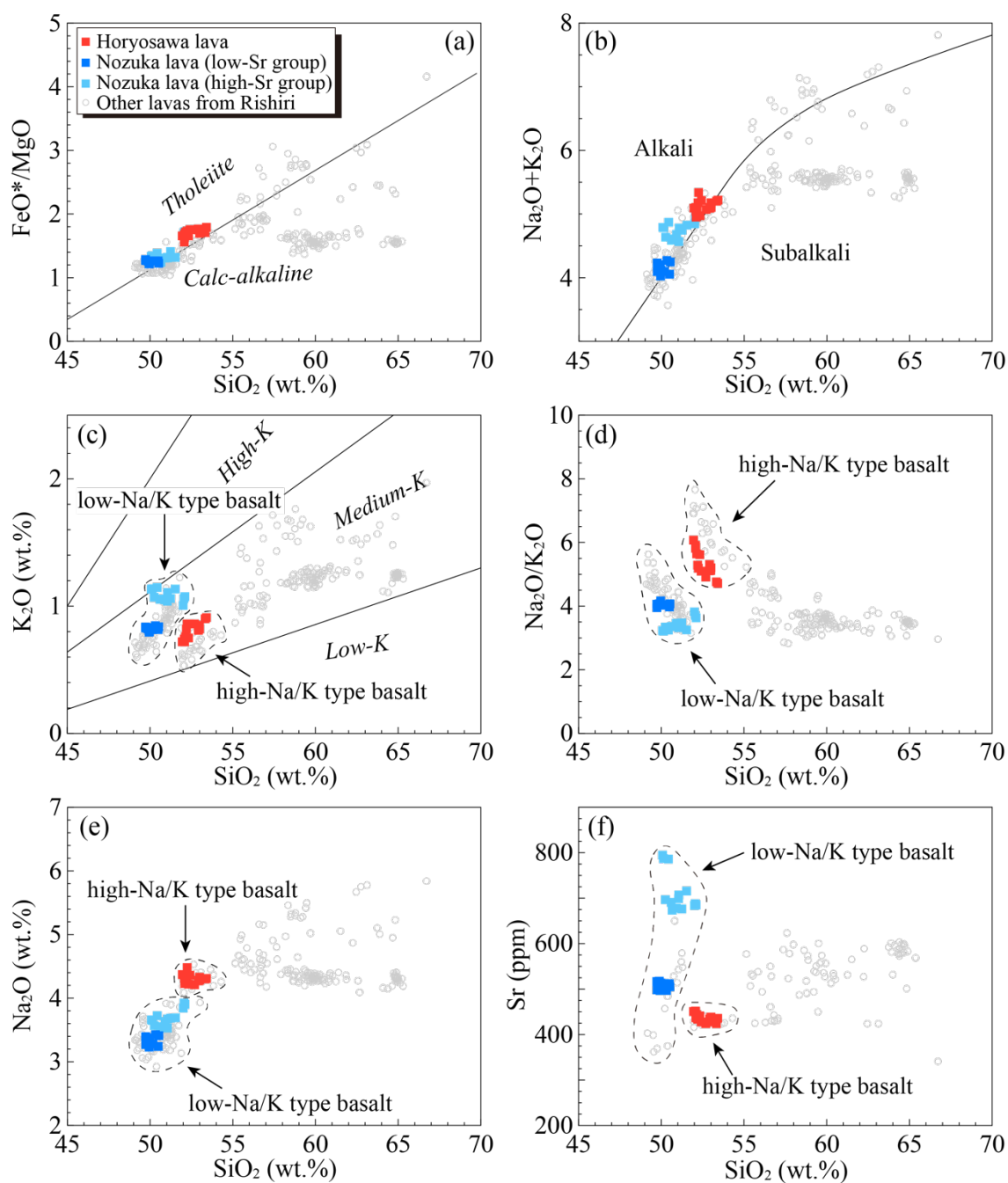
Figure 5-5. The whole-rock major and trace element compositions of the Horyosawa lava, Nozuka lava, and other lavas from the Rishiri Volcano, shown in (a) FeO*/MgO–SiO$_2$, (b) Na$_2$O + K$_2$O–SiO$_2$, (c) K$_2$O–SiO$_2$, (d) Na$_2$O/K$_2$O–SiO$_2$, (e) Na$_2$O–SiO$_2$, and (f) Sr–SiO$_2$ diagrams. In (a), (b), and (c), discrimination line between the calc-alkaline and tholeiite series, the alkali and subalkali series, and the high-K, medium-K, and low-K series, are taken from Miyashiro (1974), Miyashiro (1978), and Peccerillo and Taylor (1976), respectively. In (a)–(f), whole-rock compositions of the Nozuka lava are taken from Kuritani and Nakagawa (2016) and data of other lavas from the Rishiri of Ishizuka (2000) and Taniuchi et al. (2020a, 2020b) are also shown.
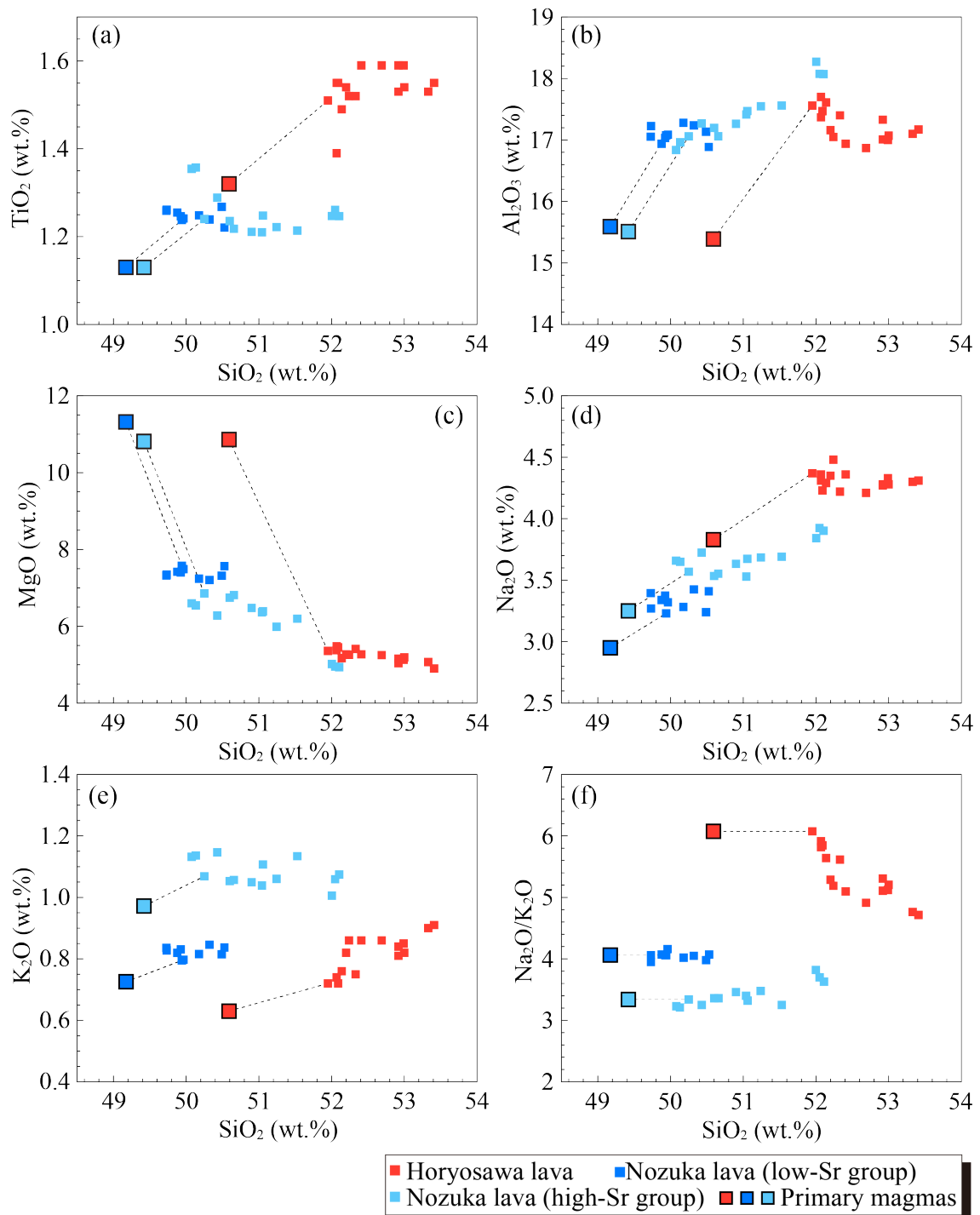
Figure 5-6. Whole-rock major element compositions of the Horyosawa lava and Nozuka lava from the Rishiri Volcano, shown in (a) TiO_2–SiO_2, (b) Al_2O_3–SiO_2, (c) MgO–SiO_2, (d) Na_2O–SiO_2, (e) K_2O–SiO_2, and (f) Na_2O/K_2O–SiO_2 diagrams. The squares with black edge represent the estimated primary magma compositions for the Horyosawa lava and Nozuka lava. The whole-rock compositions of the Nozuka lava are taken from Kuritani and Nakagawa (2016).

5-4-2. Trace elements

The SiO$_2$ variation diagram for Sr is shown in Fig. 5-5f with the chemical composition of other lavas from the Rishiri Volcano. The Sr concentration of the high-Na/K type basalts, including the Horyosawa lava, is 400–500 ppm and is less variable than those of low-Na/K type basalt, including the Nozuka lava. The spider diagrams for primitive mantle-normalized trace elements and rare-earth elements of the Horyosawa lava are presented in Figs. 5-7a and 5-7b, respectively, with the chemical composition of the Nozuka lava. The trace element spider diagram shows a typical island-arc pattern with positive spikes for Sr and Pb and negative spikes for Nb and Ta (Fig. 5-7a). Rare-earth elements of the Horyosawa lava show a relatively lower ratio of heavy-REEs to light-REEs than those of Nozuka lava (Fig. 5-7b). The Eu anomalies (= Eu$_N$/Eu*, where Eu* = (Sm$_N$ × Gd$_N$)$^{0.5}$) tend to decrease slightly with increasing whole-rock SiO$_2$ content (Fig. 5-7c), and the anomalies in the lower SiO$_2$ samples are less than the analytical uncertainty.

5-4-3. Radiogenic isotope

The SiO$_2$ variation diagrams for ^{87}Sr/^{86}Sr, ^{143}Nd/^{144}Nd, and ^{206}Pb/^{204}Pb of the Horyosawa lava are presented in Fig. 5-8. The ^{87}Sr/^{86}Sr ratios tend to decrease slightly with increasing whole-rock SiO$_2$ content (Fig. 5-8a). In contrast to the Sr isotopic variation, the ^{143}Nd/^{144}Nd (Fig. 5-8b) and ^{206}Pb/^{204}Pb (Fig. 5-8c) ratios are homogeneous. The ^{87}Sr/^{86}Sr, ^{206}Pb/^{204}Pb, and ^{208}Pb/^{204}Pb ratios of the Horyosawa lava are lower than those of the
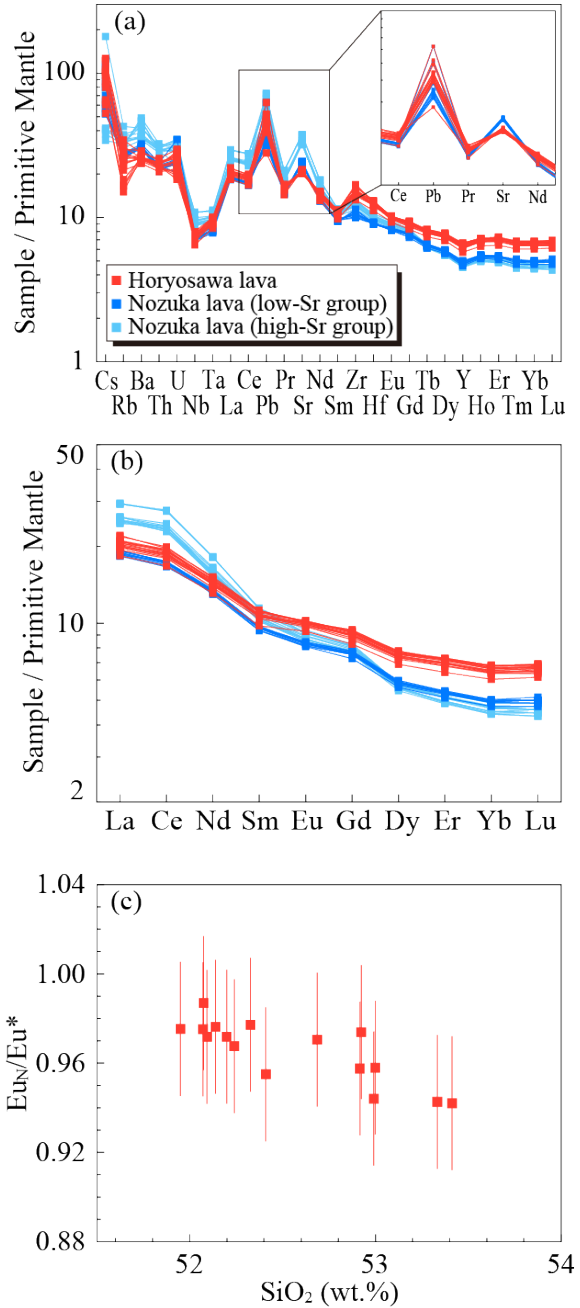
Figure 5-7. (a, b) Trace element compositions of the Horyosawa lava and Nozuka lava from the Rishiri Volcano, shown in (a) primitive mantle-normalized diagram of trace element concentration, (b) primitive mantle-normalized diagram of rare-earth element concentration, and (c) Eu$_N$/Eu*–SiO$_2$ diagram. In (a) and (b), the data of the Nozuka lavas are taken from Kuritani and Nakagawa (2016). In (a)–(c), trace element concentrations of the primitive mantle are taken from Sun and McDonough (1989).

Nozuka lava. On the other hand, the Horyosawa lava shows lower $^{143}Nd/^{144}Nd$ ratios than the Nozuka lava (Fig. 5-9).

5-5. Magmatic processes and phenocryst crystallization mechanism of the Horyosawa lava

In this section, I clarify the magmatic processes and origin of the phenocrysts as a preliminary step to estimate chemical composition and generation conditions of the Horyosawa primary magma.

5-5-1. Magmatic processes of the Horyosawa lava

The Horyosawa lavas do not show typical petrological features of magma mixing such as disequilibrium mineral assemblage, reverse zonation in the phenocrysts, and dusty zone in the plagioclase phenocrysts. These characteristics indicate that magma mixing was not an essential process for the formation of the whole-rock compositional variation of the Horyosawa lava. It is also recognized that the $^{87}Sr/^{86}Sr$ tends to slightly decrease with increasing SiO_2 content (Fig. 5-8a), but the variation is small and the $^{143}Nd/^{144}Nd$ (Fig. 5-8b) and $^{206}Pb/^{204}Pb$ (Fig. 5-8c) ratios are almost constant, suggesting that the effect of assimilation on the compositional change of the Horyosawa lava was also limited.

The Al_2O_3 (Fig. 5-6b), MgO (Fig. 5-6c), CaO, and Sr contents of the Horyosawa lava tend to decrease with increasing whole-rock SiO_2 content. These observations suggest that the compositional variation of the Horyosawa lava would be produced primarily by the fractional crystallization. This idea is supported by the Eu_N/Eu^* that tends to decrease with increasing SiO_2 content (Fig. 5-7c).
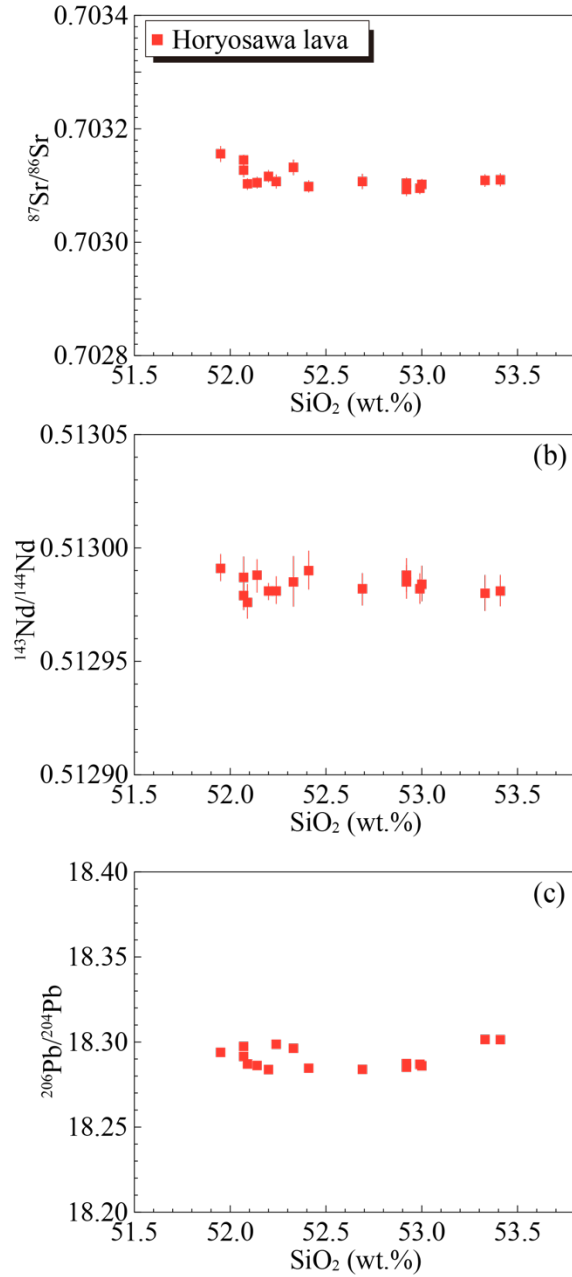
Figure 5-8. Radiogenic isotopic compositions of the Horyosawa lava from the Rishiri Volcano shown in (a) $^{87}Sr/^{86}Sr–SiO_2$, (b) $^{143}Nd/^{144}Nd–SiO_2$, and (c) $^{206}Pb/^{204}Pb–SiO_2$ diagrams.
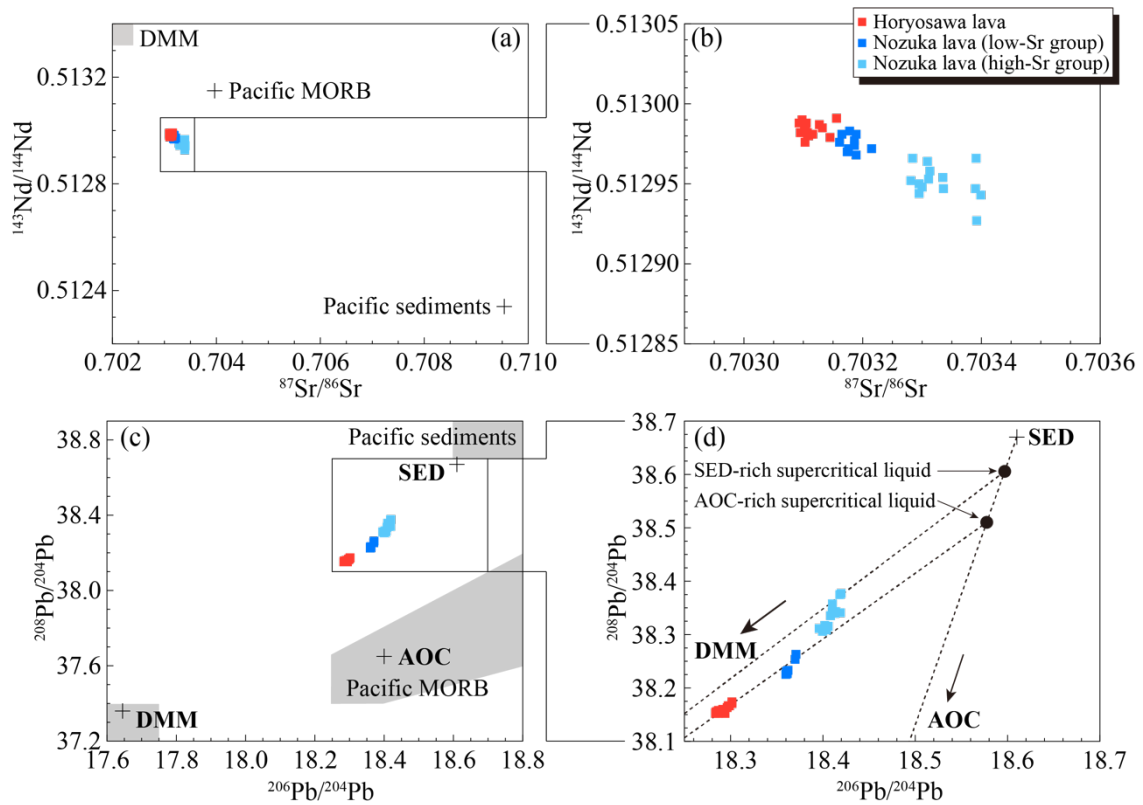
Figure 5-9. Radiogenic isotopic compositions of the Horyosawa lava and Nozuka lava from the Rishiri Volcano shown in (a, b) $^{143}Nd/^{144}Nd$–$^{87}Sr/^{86}Sr$ and (c, d) $^{208}Pb/^{204}Pb$–$^{206}Pb/^{204}Pb$ diagrams. In (a), (c), and (d), compositional fields of the depleted MORB mantle (DMM) are taken from Zindler and Hart (1986), while those of Pacific MORB and sediments are from Kimura and Yoshida (2006). The representative compositions of the Pacific sediments (SED), Pacific MORB (AOC), and DMM are taken from Cousens and Allan (1992) and Hauff et al. (2006). The data of the Nozuka lava are taken from Kuritani and Nakagawa (2016).

5-5-2. Crystallization phases in the magma chamber

As described above, the compositional variation of Horyosawa magma would be produced by the fractional crystallization, however, the phenocrysts show a wide range of chemical composition. Here, I clarify the crystallization phases in the magma chamber.

Although the phenocrysts show variable outline and internal structure, the high-Fo olivine and An-rich clear core of plagioclase show only euhedral outlines and are homogeneous in terms of chemical composition. The former is surrounded by the low-Fo olivine rim. The latter is surrounded by calcic honeycomb core or An-poor clear margin and compose Type-1 and Type-2 plagioclase phenocrysts. Additionally, they do not contain any mineral inclusions. These observations suggest that the high-Fo olivine and An-rich clear core of plagioclase are earliest crystallization phases and their growth proceeded under a static physical and chemical environment. On the other hand, the observation that all plagioclase phenocrysts are classified as Type-1 to Type-4 (Fig. 5-4) clearly indicates that crystallization of the calcic honeycomb core/mantle and An-

poor clear margin proceeded after the formation of An-rich clear core. Additionally, the low-Fo olivine and clinopyroxene form crystal aggregate with these regions of plagioclase, suggesting that they also grew after the formation of high-Fo olivine and An-rich clear core. The calcic honeycomb core and An-poor clear margin, that shows the elongated shape (Figs. 5-4f and 5-4h), suggests rapid growth due to supercooling (Kawamoto, 1992; Kuritani, 1999). These petrographycal observations suggest that only the high-Fo olivine and An-rich clear core crystallized under static physical and chemical environment such in the magma chamber followed by the formation of other phases.

To examine the hypothesis based on the petrography, I estimate the Fo content of olivine and Mg# of clinopyroxene that crystallize in equilibrium from the melt corresponding to the whole-rock composition. In this estimation, the $Fe^{3+}/\Sigma Fe$ is assumed to be 0.2–0.3. The $K_D(Fe/Mg)^{olivine/melt}$ and $K_D(Fe/Mg)^{clinopyroxene/melt}$ are also assumed to be 0.3 and 0.23, respectively (Roeder and Emslie, 1970; Sisson and Grove, 1993). As a result, Fo content of olivine and Mg# of clinopyroxene, which can coexist in equilibrium with melts corresponding to whole-rock composition, were obtained to be 80–84 and 79–82, respectively (Figs. 5-3a, 5-3b, 5-3d, 5-3e, 5-3g, and 5-3h). This result suggests that some high-Fo (> ~80) olivine crystallized from the melt with similar composition to the whole-rock composition, while the low-Fo olivine (< ~80) and all clinopyroxene formed from the melt with more differentiated composition and essentially support the hypothesis. Moreover, although the Fo contents of low-Fo olivine, Mg#'s of clinopyroxene, and An# contents of calcic honeycomb core/mantle and An-poor clear margin of plagioclase do not show systematic variation with whole-rock composition, the highest Fo content of high-Fo olivine and An# content of An-rich clear core of plagioclase decrease with increasing whole-rock SiO_2 content, suggesting their crystallization and fractionation in the magma chamber because the compositional variation of the Horyosawa magma mainly formed by the fractional crystallization. Therefore, I conclude that the high-Fo olivine and An-rich clear core of plagioclase would be crystallized *in situ* in the magma chamber before the formation of low-Fo olivine, clinopyroxene, and the calcic honeycomb core and An-poor clear margin of plagioclase.

5-5-3. Water content of the Horyosawa magma

The water content of the Horyosawa magma is estimated using the plagioclase-melt hygrometer given in Putirka (2008). In this estimation, I can assume that the plagioclase with the highest An# of 86.0 in the Horyosawa lava was in equilibrium with the melt that had the chemical composition corresponding to the HOL-13 because the highest An# plagioclase would be crystallized *in situ* in the magma chamber as discussed above. Although it is difficult to estimate the crystallization pressure using such as two pyroxene geobarometer because of the absence of orthopyroxene, I assume 0.3 GPa, which estimated as the depth for the basaltic magma chamber beneath the volcano in the previous study (Kuritani and Nakagawa, 2016). It is also worth noting

that the pressure dependence of the hygrometer is relatively small as shown in Fig. 5-10. The water content of the melt is estimated by simultaneously solving Equations (25b) and (26) given in Putirka (2008) at a pressure of 0.3 GPa and obtained to be 3.4 ± 1.1 wt.%. The water content is also estimated by the plagioclase-melt hygrometer given in Waters and Lange (2015), yielding 2.6 wt.%. This result is within the ranges of the estimates of 3.4 ± 1.1 wt.%, obtained by the hygrometer given in Putirka (2008).

5-5-4. Crystallization mechanism of the phenocrysts

As mentioned above, it is suggested that only the high-Fo olivine and An-rich clear core of plagioclase formed in the magma chamber. Here, I constrain the crystallization mechanism of the other phenocrysts or regions, i.e., low-Fo olivine, clinopyroxene, and calcic honeycomb core/mantle and An-poor clear margin of plagioclase.

The water content and pressure conditions under which the plagioclases of each An# contents can be crystallized by simultaneously solving Equations (25b) and (26) given in Putirka (2008). In this estimation, it is necessary to assume the melt composition from which the plagioclase crystallized. As described above, the calcic honeycomb core/mantle would be formed after the crystallization of high-Fo olivine and An-rich clear core of plagioclase. Additionally, since the calcic honeycomb core and the low-Fo olivine are coexisting in crystal aggregate, it could be assumed that they were formed at the almost same timing. On the other hand, the Type-4 plagioclase phenocrysts, which consist of only the An-poor clear margin, often form crystal aggregate with clinopyroxene, suggesting that they were crystallized simultaneously. Therefore, for the estimation of calcic honeycomb core/mantle of plagioclase, it is used that the melt composition calculated by subtracting the chemical composition of high-Fo olivine and An-rich clear core of plagioclase multiplied by their modal amounts from the whole-rock composition of the HOL-13 and named melt-1 (Fig. 5-10a). For the estimation of the An-poor clear margin of plagioclase, it is used that the melt composition calculated by subtracting the chemical composition of the high-Fo and low-Fo olivine and An-rich clear core and calcic honeycomb core of plagioclase multiplied by their modal amounts from the whole-rock composition of the HOL-13 and named melt-2 (Fig. 5-10a).

Fig. 5-10b shows the An# contents of the plagioclase that crystallize at each pressure and water content condition from the calculated melt-1 and melt-2. Based on the results, the calcic honeycomb core (An# < ~75) would be crystallized from a melt-1 with intermediate H_2O content (< ~2.0 wt.%), while those of An-poor clear margin (An# < ~65) would be formed from a melt-2 with significantly low H_2O content (< ~0.5 wt.%). These results indicate that it is necessary to reduce the water content in the melt to crystallize these regions of plagioclase because the water content of the melt in the Horyosawa magma chamber is obtained to be 3.4 wt.%, as described

78
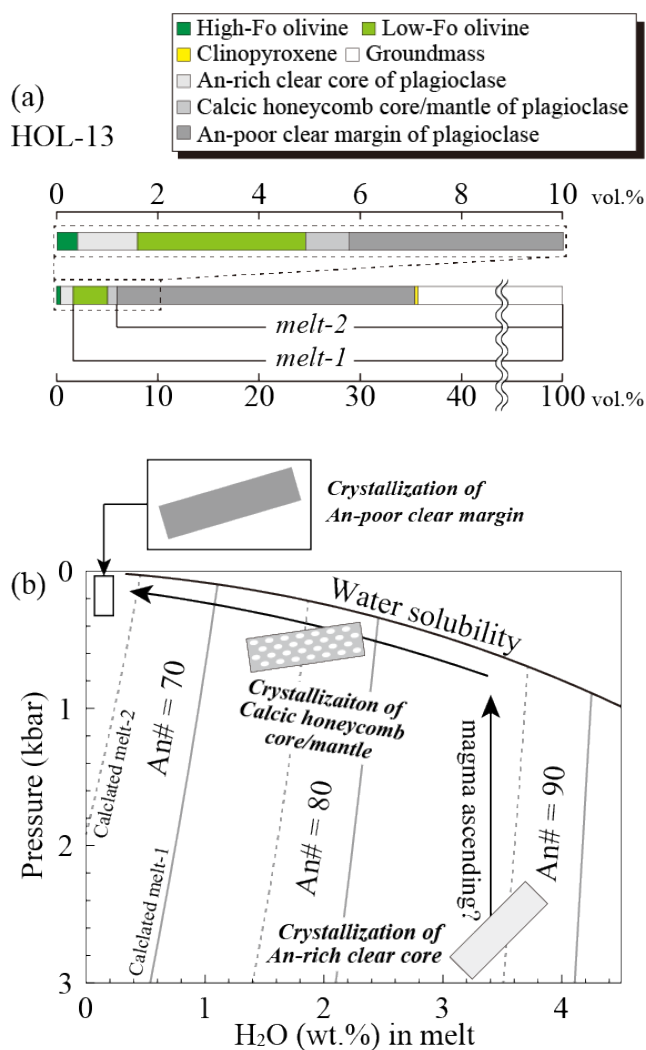
Figure 5-10. (a) The modal amounts of phenocrysts in HOL-13 of the Horyosawa lava. The conceptual compositions of melt-1 and melt-2 used to calculate the crystallization conditions of plagioclase are also shown. (b) The calculated An# contents of the plagioclase crystallize from the melt-1 and melt-2 shown in the pressure–H_2O diagram. The An# contents are obtained by plagioclase-melt hygrometer given in Putirka (2008). For the crystallization conditions of the calcic honeycomb core/mantle, melt-1, that calculated by subtracting the chemical composition of the high-Fo olivine and An-rich clear core of plagioclase multiplied by their modal amounts from the whole-rock composition of the HOL-13, is used, and the results are shown as gray continuous lines. For the crystallization conditions of the An-poor clear margin, melt-2, that calculated by subtracting the chemical composition of the high-Fo and low-Fo olivine and the An-rich clear core and honeycomb core/mantle of plagioclase multiplied by their modal amounts from the whole-rock composition of the HOL-13, is used, and the results are shown as gray dashed lines.

above. One of the ideas that reduce the water content of the melt is the crystallization of hydrous minerals. However, since the Horyosawa lava only contains anhydrous minerals such as olivine, clinopyroxene, and plagioclase, the water content of the melt has not been reduced by the crystallization of phenocrysts. Therefore, the decrease in water solubility of melt during the magma ascending would have played an important role in reducing the water content, resulting in the crystallization of the calcic honeycomb core/mantle, followed by the formation of An-poor clear margin (Fig. 5-10b). Since the low-Fo olivine and clinopyroxene compose crystal aggregate with the calcic honeycomb core/mantle and An-poor clear margin of plagioclase and their Fo contents and Mg#'s are lower than those crystallized in equilibrium from melts corresponding to the whole-rock composition as described above, they also have crystallized from differentiated melt after extensive crystallization during magma ascending.

Based on the constraints on the crystallization order and the formation conditions, the phenocrysts, which crystallized in the magma chamber, were limited to the high-Fo olivine and An-rich clear core of plagioclase with a modal abundance of at most a few vol.%. On the other

hand, the majority of the phenocrysts, such as the low-Fo olivine, clinopyroxene, and the calcic honeycomb core/mantle and An-poor clear margin of plagioclase, have formed under supersaturated conditions due to the increase of the liquidus temperature caused by the magma ascending and water reducing. These results show that the Horyosawa magma was aphyric in the magma chamber. A previous study has also found that a similar crystallization process occurred in the Kutsugata lava flows (Kuritani, 1999), which is another alkaline basalt from the Rishiri Volcano, and it may be a common process in this volcano.

5-6. Primary magma of the Horyosawa lava

5-6-1. Chemical composition of the primary magma

The MgO content (~5.4) and Mg# (~51.8) of the HOL-13 sample of the Horyosawa lava are quite lower than those of the melt that can coexist with mantle peridotite, suggesting significant differentiation from the primary magma. Because the Eu anomaly is not significant in the HOL-13 (i.e., less than the analytical uncertainty), it is suggested that plagioclase fractionation was not so significant to derive the HOL-13 magma from the primary magma. Besides, all the clinopyroxene phenocrysts are suggested to have crystallized during magma ascent, and clinopyroxene was not a crystallization phase in the magma chamber. Therefore, it can be assumed that the HOL-13 magma with the lowest SiO_2 content was essentially produced by the fractional crystallization of olivine from the primary magma. In this case, the chemical composition of the primary magma can be estimated using the olivine maximum fractionation model by Tatsumi et al. (1983), i.e., incremental addition of equilibrium olivine to the melt until the calculated melt composition reach equilibrium with the source mantle. In this estimation, the $Fe^{3+}/\Sigma Fe$ is assumed to be 0.23, using the estimated water content of the Horyosawa lava (3.4 wt.%) and the relationship between $Fe^{3+}/\Sigma Fe$ and H_2O content of basaltic magma by Kelley and Cottrell (2009). The $K_D(Fe/Mg)^{olivine/melt}$ is also assumed to be 0.3 (Roeder and Emslie, 1970). The incremental addition of 0.1% of equilibrium olivine to the melt is continued until the equilibrium olivine reaches Fo = 90.0. The Fo content of 90.0 was determined through iterative calculations so that this Fo content would be consistent with the prediction by the pMELTS model (e.g., Ghiorso et al., 2002) at a given degree of melting of the source mantle, as estimated below. As a result, the magma composition of SiO_2 = 50.6 wt.% and MgO = 10.9 wt.% is obtained as the primary magma composition by the 13.2% addition of equilibrium olivine (Table. 5-2; Fig. 5-6).

5-6-2. Magma generation conditions

In this section, I first obtain the degrees of partial melting and the modal content of garnet in the source mantle. Then the magma generation conditions (temperature, pressure, and H_2O content of the source mantle) of the primary magmas of the Horyosawa lava are estimated.
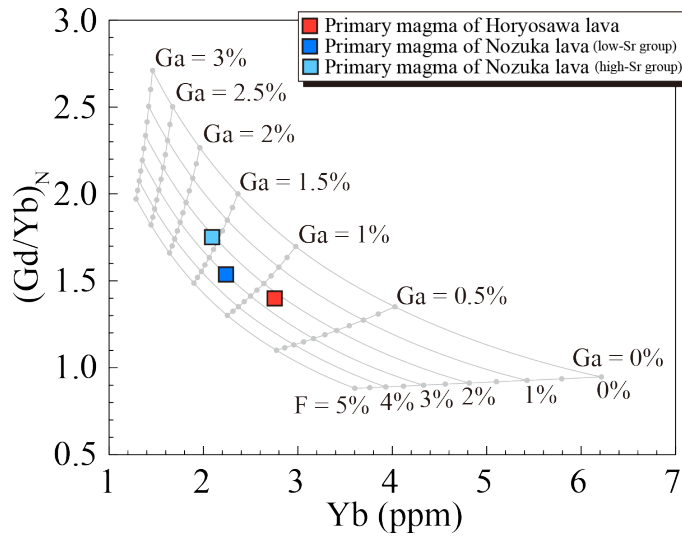
Figure 5-11. The primary magma composition of the Horyosawa lava and Nozuka lava shown in (Gd/Yb)$_N$–Yb diagram. In this figure, the Yb content and (Gd/Yb)$_N$ ratio of the melt generated by various degrees of partial melting of the DMM with different garnet content are also shown. The data of the primary magmas of the Nozuka lava are taken from Kuritani and Nakagawa (2016) and re-estimated (see Appendix).

The primitive mantle-normalized rare-earth element patterns of the Horyosawa lava show LREE-rich and HREE-poor characteristics (Fig. 5-7b), suggesting that the depth of the source mantle corresponds to the garnet stability field. Therefore, the degree of partial melting and the garnet content in the source mantle for the primary Horyosawa magma are estimated using the method of Kuritani and Nakagawa (2016) based on the Gd and Yb contents of the primary magma and DMM (Salters and Stracke, 2004), partition coefficients (Kelemen et al., 2003). Fig. 5-11 shows the Yb content and (Gd/Yb)$_N$ ratio of the melt generated by various degrees of partial melting of the DMM with different garnet content. The comparison of the model calculation with the estimated compositions of the primary magma suggests that the primary Horyosawa magma was generated by 2.3% partial melting of the source mantle with 0.7% garnet (Fig. 5-11).

Since the water content of the primary magma and the degree of partial melting are estimated to be 3.0 ± 1.0 wt.% and 2.3%, respectively, the water content of the source mantle could be calculated using the Equation (10) of Kelley et al. (2006) and is obtained to be 0.102 ± 0.033 wt.%. In this case, the temperature and pressure conditions that produce the primary magma can be determined using the parameterized hydrous mantle melting model of Katz et al. (2003) as a condition for 2.3% partial melting of the DMM with H_2O = 0.102 ± 0.033 wt.% (Fig. 5-12). In addition, magma generation conditions can also be constrained from the equilibrium between the primary melt and olivine in the source mantle. Therefore, I estimate the olivine liquidus temperature of the primary melt. In this estimation, the olivine liquidus temperatures of the primary magma are first calculated at variable pressure conditions using the pMELTS (Ghiorso et al., 2002) and then corrected by the water content of the primary magma (3.0 ± 1.0 wt.%) using Equation (17) of Médard and Grove (2008) as shown in Fig. 5-12. In this case, pressure and temperature of 2.30 ± 0.02 GPa and 1290 ± 26 ºC, respectively, are obtained as the magma generation conditions. The errors in pressure and temperature are caused by that in the water content

of the magma as estimated by the method of Putirka (2008). The estimated magma generation conditions correspond to the garnet stability field in the mantle (Fig. 5-12).

Table 2. Chemical compositions and magma generation conditions for the primary magmas of the Horyosawa lava and low-Sr and high-Sr groups of the Nozuka lava. The data of the primary magmas of the Nozuka lava are taken from Kuritani & Nakagawa (2016) and re-estimated (see Apendix).

Lava name	Horyosawa	Nozuka Low-Sr	Nozuka High-Sr
Group name			
Chemical composition of primary magma			
SiO_2 (wt.%)	50.09	48.68	48.95
TiO_2 (wt.%)	1.31	1.12	1.12
Al_2O_3 (wt.%)	15.23	15.43	15.36
Fe_2O_3* (wt.%)	9.82	10.06	9.60
MnO (wt.%)	0.15	0.15	0.15
MgO (wt.%)	10.76	11.20	10.70
CaO (wt.%)	7.96	9.45	9.59
Na_2O (wt.%)	3.79	2.92	3.21
K_2O (wt.%)	0.62	0.72	0.96
P_2O_5 (wt.%)	0.26	0.27	0.36
total	100	100	100
H_2O (wt.%)	3.0 ± 1.0	2.3 ± 1.0	2.1 ± 1.0
Olivine addition (wt.%)	13.2	9.1	9.5
Magma generation conditions			
Degree of partial melting (%)	2.3	3.0	2.1
H_2O in the source mantle (wt.%)	0.102 ± 0.033	0.095 ± 0.042	0.068 ± 0.033
Pressure (GPa)	2.30 ± 0.02	2.40 ± 0.03	2.35 ± 0.01
Temperature (ºC)	1290 ± 26	1322 ± 32	1316 ± 28

*total Fe given as Fe_2O_3.

5-7. Controlling factors for the Na/K ratio of the primary magmas

As described above, I conduct a petrological and geological study on the high-Na/K Horyosawa lava and show that the low SiO_2 magmas were essentially derived through olivine fractionation from the primary magma. The primary magma is estimated to have been generated by 2.3% partial melting of the source mantle with 0.102 ± 0.033 wt.% H_2O at 1290 ± 26 °C and 2.30 ± 0.02 GPa. In the following sections, by comparing the results from the Horyosawa lava with published results from the low-Na/K Nozuka lava, I clarify the controlling factors that cause Na/K variation of primary basaltic magmas.

5-7-1. Primary magmas at the Rishiri Volcano

In addition to the systematic differences of the whole-rock composition between the high-Na/K Horyosawa lava and low-Na/K Nozuka lava, the estimated primary magma composition of both lavas can also be distinguishable from each other (Fig. 5-6). The primary magma of

the Horyosawa lava shows higher SiO_2, TiO_2, and Na_2O contents and Na_2O/K_2O ratio, while lower K_2O content than those of the Nozuka lava (Table 5-2; Fig. 5-6).

Kuritani and Nakagawa (2016) pointed out that the Nozuka lava was divided into low-Sr group and high-Sr group, and they were derived from primary magmas with different compositions. In addition, there existed the primary Horyosawa magma with high-Na/K ratios. Therefore, at least three types of basaltic primary magmas (i.e., the high-Na/K type, the low-Sr group of low-Na/K type, and the high-Sr group of low-Na/K type) were present beneath the volcano.

5-7-2. Origin of the Na/K variation of primary magmas: degree of partial melting?

If the source mantle has the same chemical composition, one of the major factors that can change the chemical composition of primary magma is a degree of partial melting (e.g., Sakuyama and Nesbitt, 1986; Tatsumi et al., 1983). Since the partition coefficient of K between mantle peridotite and melt is much smaller than that of Na (e.g., Gaetani et al., 2003), the degree of partial melting could change the Na/K ratio of a primary magma. In this case, a primary magma produced by a higher degree of partial melting would show a higher Na/K ratio. However, the concentration of rare-earth elements indicates that the low-Sr Nozuka primary magma with low-Na/K ratio was produced by the higher degree of partial melting than the Horyosawa primary magma with high-Na/K ratio (Fig. 5-11), which is inconsistent with the Na/K ratio expected from the relationship between partition coefficient and degree of partial melting. Therefore, it is unlikely that the difference in the degree of partial melting of the same source mantle induced the variation of the Na/K ratio of primary magmas at the Rishiri Volcano.

5-7-3. Origin of the Na/K variation of primary magmas: Slab-derived water-rich materials with different Na/K ratio?

Another possibility is that the slab-derived water-rich materials involved in the magma generation have different Na/K ratios, resulting in the variation in the Na/K ratio of primary magmas. The Rishiri Volcano is located in the back-arc region with the depth of the subducting slab reaches ~300 km (e.g., Kita et al., 2010). It has been inferred that the slab-derived water-rich material would be released as a supercritical liquid from the subducting slab that reaches such depths (Kessel et al., 2005; Mibe et al., 2011; Kawamoto et al., 2012). This hypothesis is supported by the fact that some primitive alkali basaltic magmas from the volcano show [230]Th-excesses with respect to [238]U (Kuritani et al., 2008) because slab-derived supercritical liquids produce a [230]Th-excesses by preferential partition of Th relative to U during the dehydration of the subduction slab (Kessel et al., 2005; Portnyagin et al., 2007). A previous study mentioned that the primary Nozuka magmas with different Sr, Nd, and Pb isotopic ratios were generated by the involvement of slab-derived supercritical liquid with different chemical and isotopic compositions (Kuritani and Nakagawa, 2016). Therefore, supercritical liquids with different Na/K ratios might be involved in the magma generation, causing the Na/K variation of the primary magmas.

This scenario is verified from Na/K ratio and Pb isotopic ratios. It is considered that subducted slab composed of various layers such as mantle wedge-base peridotite, sediment (SED), altered oceanic crust (AOC), and underlying slab peridotite, the peridotite components would not contain a significant amount of alkali elements and Pb (e.g., Kimura, 2017). In this case, the Na/K ratio of the slab-derived supercritical liquid is essentially controlled by the mixing ratio of the AOC and SED components. Therefore, if this scenario was the case, it would be expected that slab-derived fluid for the high-Na/K Horyosawa lava and low-Na/K Nozuka lava have different Pb isotopic ratios. However, the Pb isotopic ratios of the Horyosawa lava and low-Sr group of the Nozuka lava suggest that slab-derived supercritical liquid, that is involved in their generation, have similar Pb isotopic composition (Fig. 5-9d). This observation indicates that the chemical diversity of slab-derived supercritical liquid, which is considered to be controlled by the mixing
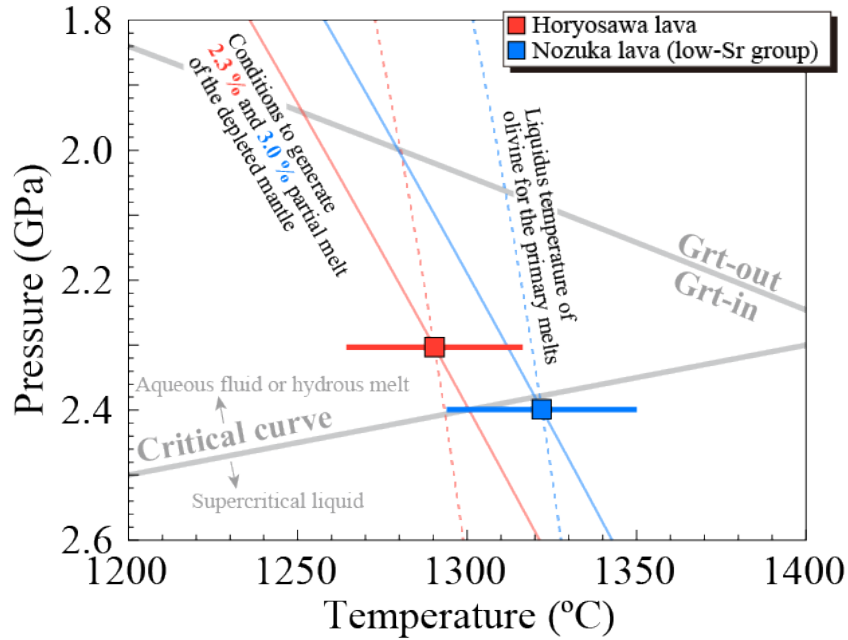
Figure 5-12. Estimated magma generation conditions of the Horyosawa lava (red) and low-Sr Nozuka lava (blue). For the Horyosawa lava, the P–T conditions of the source mantle required to generate 2.3% partial melt with a source water content of 0.102 wt.% and the liquidus temperature of olivine for a primary magma with a water content of 3.0 wt.% are shown as continuous red line and dashed red line, respectively. For the low-Sr Nozuka lava, the P–T conditions of the source mantle required to generate 3.0% partial melt with a source water content of 0.095 wt.% and the liquidus temperature of olivine for a primary magma with a water content of 2.3 wt.% are shown as continuous blue line and dashed blue line, respectively. The squares with black edge show the P–T conditions of the magma generations, which satisfy the following: (1) the degree of melting was 2.3% and 3.0% for the Horyosawa lava and low-Sr Nozuka lava, respectively, (2) the primary melt was in equilibrium with olivine. The errors in pressure and temperature caused by that in the water content of the magma as estimated by the method of Putirka (2008) are also shown. The garnet stability field calculated using the pMELTS model (Ghiorso *et al.,* 2002) and the extrapolation of the critical curve for the HMA–H_2O system estimated by Kawamoto *et al.* (2012) are also shown.

ratio of AOC and SED components, did not contribute to the production of Na/K variation of primary basaltic magma.

5-7-4. Origin of the Na/K variation of primary magmas: Separation of slab-derived supercritical liquid into aqueous fluid and hydrous melt?

It has been pointed out that the slab-derived supercritical liquid separates into aqueous fluid and hydrous melt beyond the depth corresponding to the critical point beneath the Rishiri Volcano (Taniuchi et al., 2020b). Since the separation of supercritical liquid should cause elemental partitioning (Keppler, 1996; Kawamoto et al., 2014), the Na/K ratio of the slab-derived materials might also be changed even if the chemical composition of slab-derived supercritical liquid was similar. Given that the distribution coefficient of Na and K between aqueous fluid and hydrous melt ($D^{melt/aqueous\ fluid}_{Na/K} = (C^{melt}_{Na}/C^{melt}_{K})/(C^{aqueous\ fluid}_{K}/C^{aqueous\ fluid}_{K})$) is 0.75 (Shinohara et al., 1989), the Na/K ratio of the separated aqueous fluid would be higher than that of the original slab-derived supercritical liquid. The Na_2O/K_2O ratio of the primary magmas of the Horyosawa lava and the low-Sr Nozuka lava is estimated to be 6.1 and 4.1, respectively. Therefore, the primary magma of the Horyosawa lava was formed by influx melting of aqueous fluid separated from the supercritical liquid beyond the depth corresponding to the critical point, while the low-Sr Nozuka lava was generated by the supercritical liquid-fluxed melting at deeper depths than the critical point. This hypothesis is essentially consistent with the consideration based on the Sr/Pb ratios. The Sr/Pb ratio of the Horyosawa lava and the low-Sr Nozuka lava are ~150 and ~200, respectively (Fig. 5-7a). Since the Pb is preferentially partitioned to the aqueous fluid, while Sr to the hydrous melt (Kawamoto et al., 2014), it is also suggested that the primary magma of the Horyosawa lava and the low-Sr Nozuka lava would be generated by the involvement of separated aqueous fluid and supercritical liquid, respectively.

The above model for the genesis of the primary magmas of the Horyosawa lava and the low-Sr Nozuka lava is consistent with the constraint that the former originated in a mantle with lower garnet abundant (i.e., shallower mantle) than the latter based on the REE concentrations (Fig. 5-11). This is supported by the estimation that the magma generation pressure of the Horyosawa lava and the low-Sr Nozuka lava are 2.30 and 2.40 GPa, respectively (Table 5-2; Fig. 5-12). The extrapolation of the experimentally estimated critical curve in the high-MgO andesite–H_2O system (Kawamoto et al., 2012) shows that the pressure condition corresponding to the critical end-point is ~2.4 GPa at ~1300 ºC. This is also suggesting that the primary magma of the Horyosawa lava would be produced beyond the depth corresponding to the critical point, while the low-Sr Nozuka lava would be generated at deeper part than the critical point (Fig. 5-12). From these considerations, I conclude that the primary magmas of the Horyosawa lava and the low-Sr group of the Nozuka lava were most plausibly produced by the partial melting of mantle peridotite with the influx of separated aqueous fluid and supercritical liquid, respectively (Fig. 5-13). I

propose that the separation of slab-derived supercritical liquid into aqueous fluid and hydrous melt is one of the controlling factors that cause the chemical diversity of primary basaltic magmas in subduction zone volcano.
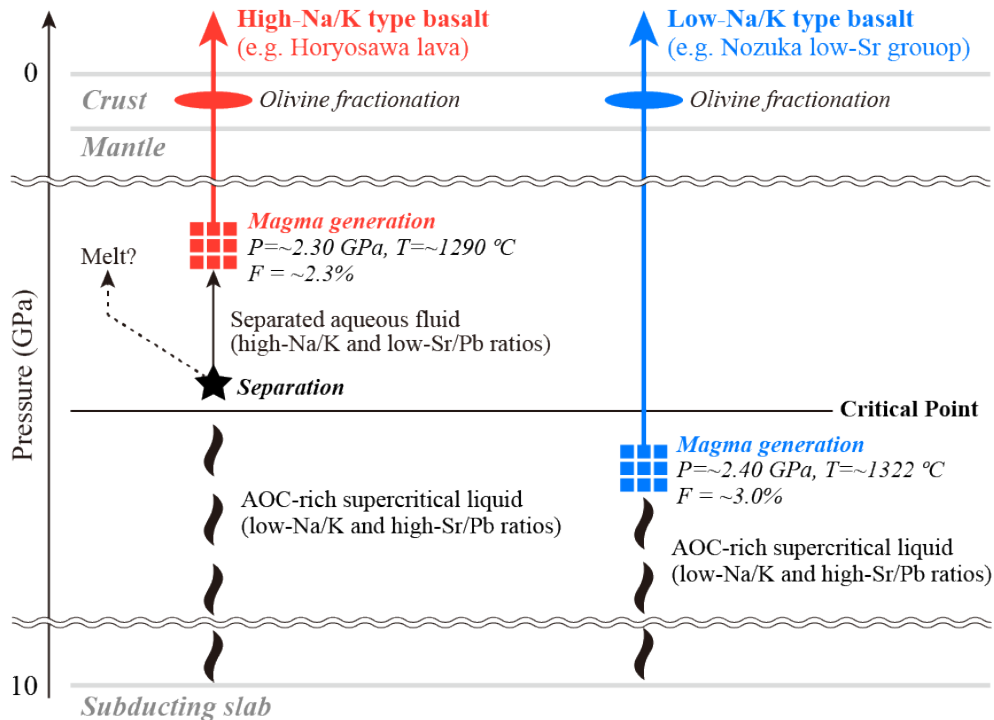

Figure 5-13. Schematic of the magma generation of the Horyosawa lava and low-Sr Nozuka lava. See text for detail.

5-8. Conclusions

To understand the controlling factors to produce Na/K variation of the primary magmas, we carried out a comparative petrological study on the high-Na/K basaltic lavas (Horyosawa lava) and low-Na/K basaltic lavas (Nozuka lava) from the Rishiri Volcano. I reached the following conclusions.

1. The crystallization phases in the magma chamber are limited to the high-Fo olivine and An-rich clear core of plagioclase and the water content of the Horyosawa magma is estimated to be 3.4 ± 1.1 wt.%. Most of the phenocrysts in the Horyosawa lava were crystallized under the supersaturated conditions from the melt with reduced water content due to the magma ascending.

2. The primary magma generation conditions are obtained to be 1290 ºC and 2.30 Gpa for the Horyosawa lava and 1322 ºC and 2.40 GPa for the low-Sr group of the Nozuka lava.

3. Based on the comparison of the high-Na/K Horyosawa lava and the low-Na/K Nozuka lava from the Rishiri Volcano, I show that the Na/K variation of primary basaltic magma can be

caused by the separation of slab-derived supercritical liquid into aqueous fluid and hydrous melt.

5-9. Appendix

Some of the methods for estimating the chemical composition and magma generation conditions of the primary magma of the Horyosawa lava differ from those of the Nozuka lava by Kuritani and Nakagawa (2016). In this appendix, I re-estimated the chemical composition and magma generation condition of the primary magma of the low-Sr group of the Nozuka lava using the same method of this chapter.

For the estimation of the chemical composition and magma generation conditions for the primary low-Sr Nozuka magma, the chemical composition of Rs#54 given in Kuritani and Nakagawa (2016) is used. The magma suggests that fractional crystallization except for olivine was not so significant to derive the Rs#54 magma from the primary magma (Kuritani and Nakagawa, 2016). Therefore, it could be estimated that the chemical composition of primary magma using the olivine maximum fractionation model by Tatsumi et al. (1983). In this estimation, the $Fe^{3+}/\Sigma Fe$ is assumed to be 0.20, using the water content of the magma (~2.5 wt.%; Kuritani and Nakagawa, 2016) and the relationship between $Fe^{3+}/\Sigma Fe$ and H_2O content of basaltic magma by Kelley and Cottrell (2009). The $K_D(Fe/Mg)^{olivine/melt}$ is also assumed to be 0.3 (Roeder and Emslie, 1970). The calculation in which the addition of 0.1% of equilibrium olivine to the melt is continued until the equilibrium olivine reaches Fo = 90.0. The Fo content of 90.0 was determined through iterative calculations so that this Fo content would be consistent with the prediction by the pMELTS model (e.g., Ghiorso et al., 2002) at a given degree of melting of the source mantle, as estimated below. As the result, the magma composition of SiO_2 = 49.2 wt.% and MgO = 11.3 wt.% is obtained by the 9.1% addition of equilibrium olivine as the primary magma compositions (Table. 5-2; Fig. 5-6).

The comparison of the model calculation (see section 6.5) with the estimated compositions of the primary magmas suggests that the primary low-Sr Nozuka magma was generated by 3.0% partial melting of the source mantle (Fig. 5-11). Since the H_2O content are estimated to be 2.5 ± 1.1 wt.% using the plagioclase-melt hygrometer given in Putirka (2008) (Kuritani and Nakagawa, 2016), the water content of the primary magma is obtained to be 2.3 ± 1.0 wt.%. Therefore, the water content of the source mantle is obtained to be 0.095 ± 0.042 wt.%, using the Equation (10) of Kelley et al. (2006).

The temperature and pressure conditions that produce the primary magma generated by estimated degree of partial melting can be determined using the parameterized hydrous mantle melting model of Katz et al. (2003). The olivine liquidus temperatures of the primary magma are first calculated at variable pressure conditions using the pMELTS (Ghiorso et al., 2002) and then

corrected by the water content of the primary magma using Equation (17) of Médard and Grove (2008). The P–T conditions of the source mantle required to generate 3.0% partial melt with a source water content of 0.095 ± 0.042 wt.% and the liquidus temperature of olivine for a primary magma with a water content of 2.3 ± 1.0 wt.% (Fig. 5-12). As a result, temperature and pressure conditions of the primary magma is estimated to be 1322 ± 32 ºC and 2.40 ± 0.03 GPa, respectively (Table 5-2; Fig. 5-12). The errors in pressure and temperature are caused by the error in the water content of the magma as estimated by the method of Putirka (2008).

Chapter 6. Discussion: Long-term evolution of the Rishiri Volcano

6-1. Long-term evolution of the Rishiri Volcano

The distribution of volcanic products, eruption rate, whole-rock compositions, and magmatic processes from the subducting slab to the surface of each stage at the Rishiri Volcano are shown in Fig. 6-1. Ishizuka (1999) and Ishizuka and Nakagawa (1999) classified the activity of the volcano into five stages based on the geological and petrological observations. In this study, I additionally showed a strong correlation between the eruption rate and the whole-rock composition of the volcanic products. In this chapter, I discuss dominant factors that controlling eruption rate and whole-rock composition based on the long-term changes of the magmatic process from the subducting slab to the surface.
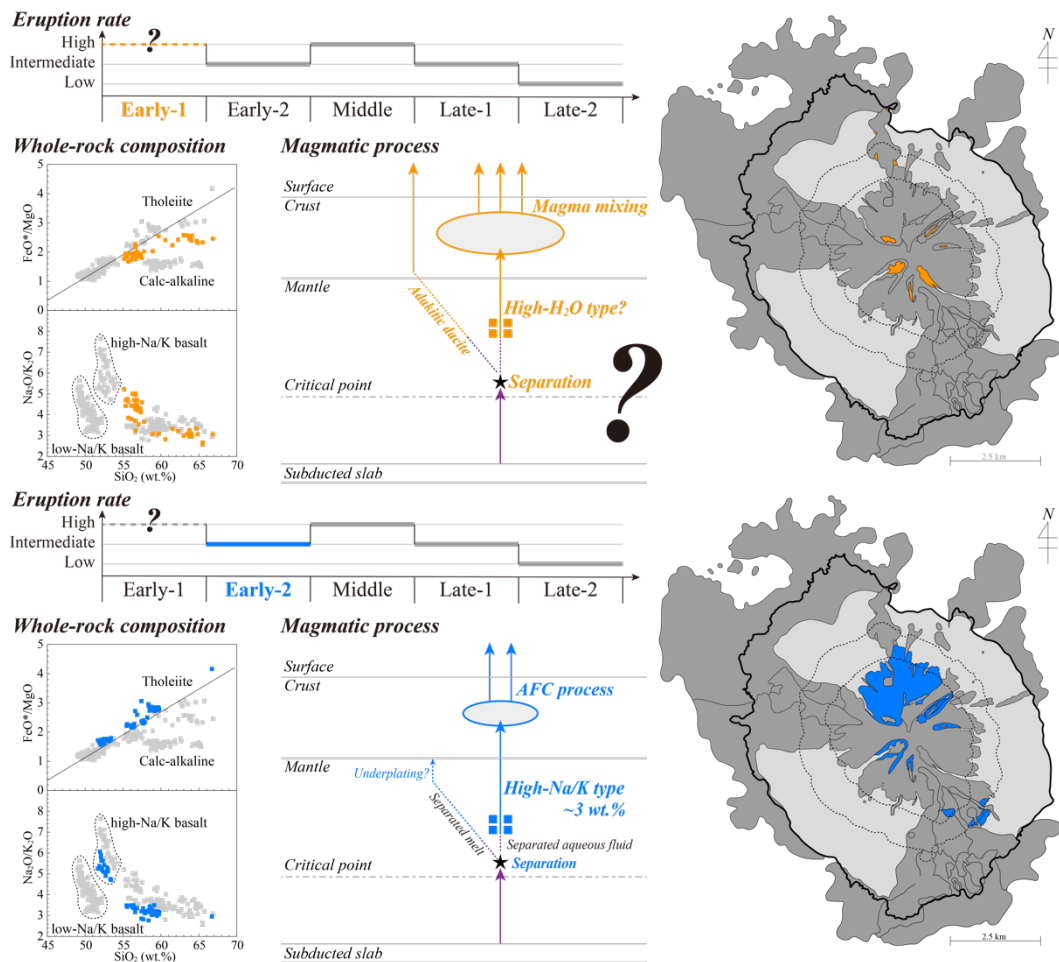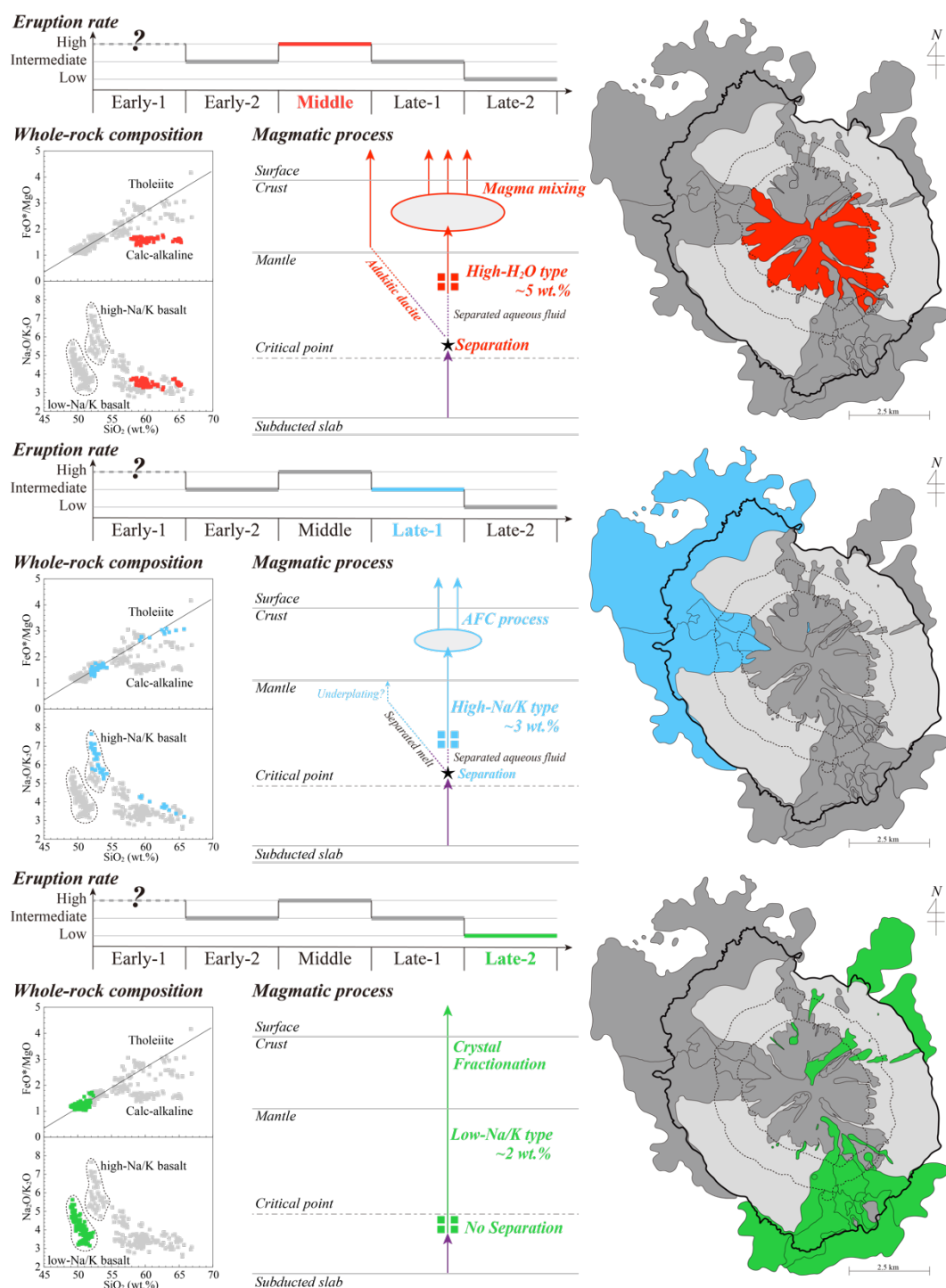
Figure 6-1 The distribution of volcanic products, eruption rate, whole-rock compositions, and magmatic processes from the subducting slab to the surface of each stage at the Rishiri Volcano. Although the eruption rate and magmatic processes in the Early-1 stage have not been fully determined, I present a plausible model at the moment. The distribution of volcanic products based on Ishizuka (1999). The discrimination line between the calc-alkaline and tholeiite series is taken from Miyashiro (1974). Whole-rock compositions are taken from Ishizuka (2000), Kuritani and Nakagawa (2016), and Taniuchi et al. (2020a, 2020b).

6-2. Factors on the change of the eruption rate

As shown in the results and discussion in Chapter 2, the eruption rate of the Rishiri Volcano varies from the beginning to the end of its activity. In this section, I aim to elucidate the factors controlling the change of the eruption rate.

The magma production rate in the mantle or crust is likely to have the greatest influence on changes of middle to long term eruption rate. Since the change in the magma production rate would be recognized as changes in the chemical composition of volcanic products, I compare the eruption rate with the chemical composition of the magmas. As described in Chapter 2 and shown in Fig. 2-4, I found that the calc-alkaline andesites to dacites erupted during the high eruption rate stages (the Early-1 and Middle stages), the tholeiite series andesites to dacites with high-Na/K type basalt erupted during intermediate eruption rate stages (the Early-2 and Late-1 stages), and only low-Na/K type basalts erupted during the low eruption rate stage (the Late-2 stage). This observation strongly suggests that the chemical composition of the magma, i.e., the genesis and differentiation process, is closely related to changes in the eruption rate. As shown in Chapter 3, the calc-alkaline andesites from the Rishiri Volcano, which erupted in the high eruption rate stages (e.g., the Middle stage), are concluded to have been essentially produced by the magma mixing between mantle-derived mafic magma and crust-derived felsic magma, and a high ratio of felsic end-member magma to mafic end-member magma is also suggested by the compositional trend of the magma mixing and estimated composition of the end-member magmas. On the other hand, the tholeiitic andesite to dacitic magmas in the intermediate eruption rate stages (e.g., the Late-1 stage) suggest that they were derived from the high-Na/K type basalt by assimilation and fractional crystallization in a crustal magma chamber with a low ratio of assimilated mass to fractionated mass (e.g., Kuritani, 1998, 1999, 2001; Kuritani et al., 2005, 2007). In addition, the low-Na/K type basalts in the low eruption rate stage (e.g., the Late-2 stage) differentiated mainly olivine fractionation with no assimilation of crustal materials (Kuritani et al., 2008; Kuritani and Nakagawa, 2016). Therefore, the differences in the chemical composition of volcanic products would be due to the amount of crust-derived magma that was involved in the mama differentiation process. These observations suggest that the change in the eruption rate of the Rishiri Volcano, rather than changes in the production rate of mantle-derived mafic magma, was due to those of crust-derived magma.

For the production of crust-derived felsic magma, the water content of the primary magma would play an important role as discussed in Chapter 3. The water content of the primary magma of the calc-alkaline andesites in the Middle stage, the high-Na/K type basalts in the Early-2 and Late-1 stages (Horyosawa lava and Kutsugata lava), and the low-Na/K type basalts in the Late-2 stage are estimated to be > 5 wt.% (this study; see detail in Chapter 3), ~3 wt.% (Kuritani, 1999; this study; see detail in Chapter 4), and ~2 wt.% (Kuritani and Nakagawa, 2016),

respectively. The solidus temperature of the crustal materials is greatly affected by the water content of the system, and the melting degree is much higher in a hydrous system than that in an anhydrous system (e.g., Lambert and Wyllie, 1974). A more hydrous magma, such as that of the primitive magma responsible for the generation of the calc-alkaline andesite magma, can supply a higher vapor flux from the solidifying magma chamber to the overlying crust (Fig. 3-8), resulting in more extensive melting of the crust. Therefore, the water content of the primary magma not only controls magmatic processes and chemical composition of the volcanic products but also determines the eruption rate. Based on these considerations, I propose that the water content of primary magma is one of the essentially controlling factors in the eruption rates.

6-3. Factors on the genesis of primary magmas

As noted above, the water content of the primary magma would control the magmatic processes in the crust and the long-term changes of the eruption rate. So why does the water content of primary magma change? What are the factors that contribute to change? To shed light on these issues, I discuss below the factors that contribute to the generation of primary magma, especially differences in water content.

At the Rishiri Volcano, the following three types of primary magma with different magma genesis are thought to have been active: a low-Na/K type primary magma, a high-Na/K type primary magma, and a high-H_2O type primary magma (Fig. 6-1). The low-Na/K type primary magma was active during the Late-2 stage and was formed by supercritical liquid-flux melting of mantle peridotite. The high-Na/K type primary magma was active during the Early-2 and Late-1 stages and would be formed by flux melting of aqueous fluid which separated from slab-derive supercritical liquid beyond the critical point. The high-H_2O type primary magma was generated by aqueous fluid-fluxed melting of mantle peridotite and active during the Middle stage (and maybe during the Early-1 stage) as a mafic end-member of calc-alkaline andesites. Notably, the adakitic dacite, derived from the separated hydrous melt, was also active at the same time with the high-H_2O type primary magma. The simultaneous activity of the high-H_2O primary magma with the adakitic dacite in the Middle stage (high eruption rate stage) indicates that the septation of slab-derived supercritical liquid into aqueous fluid and hydrous melt was more advanced than in the Early-2 and Late-1 stages (intermediate eruption rate stage), suggesting that the aqueous fluid involved in the generation of high-H_2O primary magma had a higher water content. These observations indicate that the water content of primary magma might vary depending on the fluid phase involved in its genesis. Experimental studies have shown that the more hydrous mantle produces more hydrous primary magma by partial melting (Hirose and Kawamoto, 1995; Hirose, 1997). Therefore, differences in fluid phases might play an important role to determine the chemical composition, especially water content, of primary magmas. In addition, the water content of

primary magma controlled the differentiation processes in the crust, resulting determine the chemical composition of volcanic products and eruption rate. Based on these observations and considerations, I propose that whether or not slab-derived supercritical liquid separated into aqueous fluid and hydrous melt is an important turning point in the overall volcanic system and determine the long-term evolution at the Rishiri Volcano (Fig. 6-2). The depth corresponding to the critical point would be equivalent to those in the mantle wedge beneath the volcanic front in the subduction zone (Kawamoto et al., 2012; Mibe et al., 2011), these processes would play an important role to determine the long-term evolution of the subduction zone volcano.
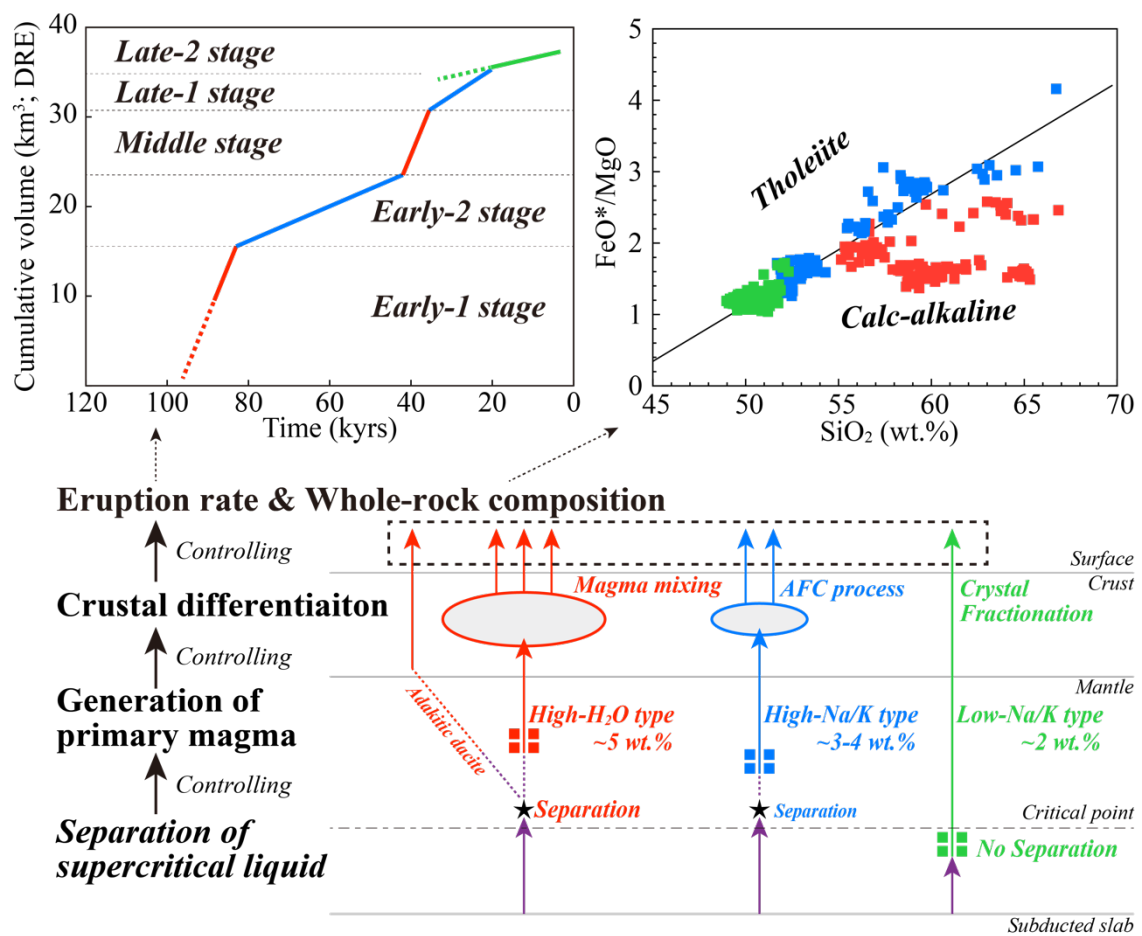
Figure 6-2 Schematic of the long-term evolution of the Rishiri Volcano. See text for details.

6-4. Future works: Factors on the separation of slab-derived supercritical liquid

As I concluded in this study, the slab-derive supercritical liquid do or do not separate into aqueous fluid and hydrous melt, controlling the evolution of magma and volcano. Therefore, it is important to identify the factors that determine the separation of supercritical liquid.

One of the simplest hypotheses of the controlling factor of the separation of slab-derived supercritical liquid is changing magma generation depth. In this case, if the magma generation region is deeper than the depth corresponding to the critical point, the slab-derived supercritical liquid can produce the primary magma. On the other hand, if the magma generation region is shallower than the depth corresponding to the critical point, the separated aqueous fluid or hydrous melt can produce the primary magma. Besides, it has been also suggested in previous studies that the depth corresponding to the critical point changes with the chemical composition of supercritical liquid, and the richer the silica content, the lower the pressure (personal conversation with Dr. T. Kawamoto; Kennedy et al., 1962; Stalder et al., 2000; Mibe et al., 2004; Mibe et al., 2007; Mibe et al., 2010; Kawamoto et al., 2012). Therefore, there are two factors that determine whether or not the supercritical liquid separates: (1) changes in the depth of the magma generation region and (2) changes in the chemical composition of the slab-derived supercritical liquid. These contributions and roles for the long-term evolution of the subduction zone volcanoes would be worth examining in the future.

Chapter 7. Conclusion

To understand the long-term evolution of a subduction zone volcano, I carried out geological, chronological, petrological, and geochemical studies on the Rishiri Volcano, southern Kuril Arc. I reached the following conclusions.

1. It was indicated that the calc-alkaline andesites to dacites erupted during the high eruption rate stages (Early-1 and Middle), the high-Na/K type basalts and tholeiitic andesites to dacites erupted during the intermediate eruption rate stages (Early-2 and Late-1), and the low-Na/K type basalts erupted during the low eruption rate stage (Late-2).

2. The calc-alkaline andesites that erupted in the Middle stage were formed through magma mixing by the three end-member magma, the primitive mafic magma, evolved mafic magma, and felsic magma. The primitive mafic end-member magma was generated by the partial melting of mantle peridotite and produced the evolved mafic end-member magma by olivine fractionation. The felsic end-member was generated by the partial melting of the crustal materials. The water content of the primitive end-member magma was obtained to be > 5 wt.%. It is suggested that the water content of the primary magma plays an important role in the genesis of calc-alkaline andesite as well as crust-derived felsic magma.

3. The adakitic dacitic magmas in the Middle stage do not show evidence of crystal fractionation, accumulation, assimilation, and magma mixing. The dacitic magma was derived from the separated hydrous melt produced by the separation of slab-derived supercritical liquid. The formation of silicic magma by the separation of slab-derived supercritical liquid has been predicted from experimental studies, I demonstrate its existence for the first time.

4. The primary magma generation conditions are obtained to be 1290 ºC and 2.30 Gpa for the Horyosawa lava (high-Na/K type basalt) and 1322 ºC and 2.40 GPa for the low-Sr Nozuka lava (low-Na/K type basalt). Based on the comparison of the high-Na/K Horyosawa lava and the low-Na/K Nozuka lava from the Rishiri Volcano, I show that the Na/K variation of primary basaltic magma can be caused by the separation of slab-derived supercritical liquid into aqueous fluid and hydrous melt.

5. In the case of the Rishiri Volcano, it is found that the processes from primary magma generation in the mantle to eruption at the surface were controlled by whether or not the slab-derived supercritical liquid separates into aqueous fluid and hydrous melt.

Acknowledgements

References

Abe, A., 1934. Geologic report of Rishiri Volcano, Kitami distinct, Hokkaido. *Graduated Thesis of Hokkaido University, Sapporo.* (in Japanese).

Adam, J., Green, T., 2006. Trace element partitioning between mica- and amphibole-bearing garnet lherzolite and hydrous basanitic melt: 1. Experimental results and the investigation of controls on partitioning behavior. *Contributions to Mineralogy and Petrology*, 152, 1–17.

Alonso-Perez, R., Müntener, O., Ulmer, P., 2009. Igneous garnet and amphibole fractionation in the roots of island arcs: experimental constraints on andesitic liquids. *Contributions to Mineralogy and Petrology* 157, 541–558.

Annen, C., Blundy, J. D., Sparks R. S. J., 2006. The genesis of intermediate and silicic magmas in deep crustal hot zones. *Journal of Petrology* 47, 505–539.

Arai, S., 1987. An estimation of the least depleted spinel peridotite on the basis of olivine-spinel mantle array. *Neues Jahrbuch für Mineralogie, Monatshefte* 8, 347–354.

Arndt, N. T., 2013. Formation and evolution of the continental crust. *Geochemical Perspectives* 2, 405–533.

Atherton, M. P., Petford, N., 1993. Generation of sodium-rich magmas from underplated basaltic crust. *Nature* 362, 144–146.

Baker, W. E., 1973. The role of humic acids from Tasmanian podzolic soils in mineral degradation and metal mobilization. *Geochimica et Cosmochimica Acta* 37, 269–281.

Baker, M. B., Grove, T. L., Price, R., 1994. Primitive basalts and andesites from the Mt. Shasta region, N. California: products of varying melt fraction and water content. *Contributions to Mineralogy and Petrology* 118, 111–129.

Bau, M., Knittel, U., 1993. Significance of slab-derived partial melts and aqueous fluids for the genesis of tholeiitic and calc-alkaline island-arc basalts; evidence from Mt. Arayat, Philippines. *Chemical Geology* 105, 233–251.

Bowen, N. L., 1928. *The evolution of Igneous Rocks*. Princeton University Press.

Bronk Ramsey, C., 2009. Bayesian analysis of radiocarbon dates. *Radiocarbon* 51, 337–360.

Bureau, H., Keppler, H., 1999. Complete miscibility between silicate melts and hydrous fluids in the upper mantle: experimental evidence and geochemical implications. *Earth and Planetary Science Letters* 165, 187–196.

Cheng, H., Edwards, R., L., Hoff, J., Gallup, C. D., Richards, D. A., Asmerom, Y., 2000. The half-lives of uranium-234 and thorium-230. *Chemical Geology* 169, 17–33.

Condie, K. C., Potts, M. J., 1969. Calc-alkaline volcanism and the thickness of the early Precambrian crust in North America. *Canadian Journal of Earth Science* 6, 1179–1184.

Conway, C. E., Townsend, D. B., Leonard, G. S., Wilson, C. J. N., Calvert, A. T., Gamble, J. A., 2015. Lava-ice interaction on a large composite volcano: a case study from Ruapehu, New Zealand. *Bulletin of Volcanology* 77, 21.

Cousens, B. L., Allan, J. F., 1992. A Pb, Sr, and Nd isotopic study of basaltic rocks from the Sea of Japan, LEGS 127/128, in: Tamaki, K., Suyehiro, K., Allan, J., McWilliams, M. (Eds.), *Proceedings of the Ocean Drilling Program, Scientific Results* 127–128. College Station, TX: Ocean Drilling Program, pp. 805–817.

Defant, M. J., Drummond, M. S, 1990. Derivation of some modern arc magmas by melting of young subducted lithosphere. *Nature* 347, 662–665.

DePaolo, D. J., 1981. Trace element and isotopic effects of combined wallrock assimilation and fractional crystallization. *Earth and Planetary Science Letters* 53, 189–202.

Eichelberger, J. C., 1975. Origin of andesite and dacite: evidence of mixing at Glass Mountain in California and at other Circum-Pacific volcanoes. *Bulletin of Geological Society of America* 86, 1381–1391.

Elliott, T., 2003. Tracers of the slab in Inside the Subduction Factory (ed. Eiler, J.) *Geophysical Monograph* 138, 23–45. (American Geoscience Union).

Frey, H. M., Lange, R. A., Hall, C. M., Delgado-Granados, H., 2004. Magma eruption rates constrained by $^{40}Ar/^{39}Ar$ chronology and GIS for the Ceboruco-San Pedro volcanic field, western Mexico. *Geological Society of America Bulletin* 116, 259–276.

Fujinawa, A., 1988. Tholeiitic and calc-alkaline magma series at Adatara volcano, northeast Japan: 1. Geochemical constraints on their origin. *Lithos* 22, 135–158.

Fujinawa, A., 1990. Tholeiitic and calc-alkaline magma series at Adatara volcano, Northeast Japan: 2. Mineralogy and phase relations. *Lithos* 24, 217–236.

Ghiorso, M. S., Hirschmann, M. M., Reiners, P. W., Kress, V. C., 2002. The pMELTS: A revision of MELTS for improved calculation of phase relations and major element partitioning related to partial melting of the mantle to 3 GPa. *Geochemistry, Geophysics, Geosystems* 3, 1030.

Gill, J. B, 1981. *Orogenic Andesites and Plate Tectonics*. Heidelberg, Springer.

Hacker, B. R., Peacock, S. M., Abers G. A., Holloway S. D., 2003. Subduction factory 2. Are intermediate-depth earthquakes in subducting slabs linked to metamorphic dehydration reactions?. *Journal of Geophysical Research: Solid Earth* 108, 2030.

Hauff, F., Hoernle, K., Schmidt, A., 2003. Sr–Nd–Pb composition of Mesozoic Pacific oceanic crust (Site 1149 and 801, ODP Leg 185): Implications for alteration of oceanic crust and the input into the Izu–Bonin–Mariana subduction system. *Geochemistry, Geophysics, Geosystems* 4, 8913.

Hayakawa, Y., 1985. Pyroclastic geology of Towada volcano. *Bulletin of Earthquake Research Institute* 60, 507–509.

Hirose, K., Kushiro, I., 1993. Partial melting of dry peridotites at high pressures: Determination of compositions of melts segregated from peridotite using aggregates of diamonds. *Earth and Planetary Science Letters* 114, 477–489.

Hirose, K., 1997. Melting experiments on lherzolite KLB-1 under hydrous conditions and generation of high-magnesian andesitic melts. *Geology* 25, 42–44.

Hildreth, W., Lanphere, M. A., 1994. Potassium-argon geochronology of a basalt-andesite-dacite arc system: The Mount Adams Volcanic Field, Cascade Range of southern Washington. *Geological Society of America Bulletin* 106, 1413–1429.

Hildreth, W., Fierstein, J., Lanphere, M. A., 2003. Eruptive history and geochronology of the Mount Baker volcanic field, Washington. *Geological Society of America Bulletin* 115, 729–764.

Hunter, A. G., Blake, S., 1995. Petrogenetic evolution of a transitional tholeiitic-calc-alkaline series: Towada volcano, Japan. *Journal of Petrology* 36, 1579–1605.

Hunter, A. G., 1998. Intracrustal controls on the coexistence of tholeiitic and calc-alkaline magma series at Aso Volcano, SW Japan. *Journal of Petrology* 39, 1255–1284.

Huppert, H. E., Sparks, R. S. J., 1988. The generation of granitic magmas by intrusion of basalt into continental crust. *Journal of Petrology* 29, 599–624.

Ida, Y., 1983. Convection in the mantle wedge above the slab and tectonic processes in subduction zones. *Journal of Geophysical Research: Solid Earth* 88, 7749–7456.

Igarashi, Y., 2006. Late Holocene vegetation history in Minamihama wetland and Numaura wetland, Rishiri island, Hokkaido. *Rishiri Research* 25, 71–82 (in Japanese with English abstract).

Ishikawa, T., Nakamura E., 1994. Origin of the slab component in arc lavas from across-arc variation of B and Pb isotopes. *Nature*, 370, 205–208.

Ishizuka, Y., Nakagawa, M., 1994. K-Ar ages of dacitic lava domes of Rishiri volcano, northern Hokkaido. *Journal of Mineralogy, Petrology and Economic Geology* 89, 360–364 (in Japanese with English abstract).

Ishizuka, Y., 1999. Eruptive history of Rishiri Volcano, northern Hokkaido, Japan (in Japanese with English abstract). Bulletin of the Volcanological Society of Japan 44, 23–40.

Ishizuka, Y., Nakagawa, M., 1999. Petrological evolution of Rishiri volcano, northern Hokkaido, Japan (in Japanese with English abstract). *Journal of Mineralogy, Petrology and Economic Geology* 94, 279–294.

Ishizuka, Y, 2000. Mantle diaper model for polygenetic volcanoes: Geological and petrological study of Rishiri Volcano, northern Hokkaido, Japan. *PhD thesis, Graduate School of Science, Hokkaido University, Sapporo.*

Itaya, T., Nagao, K., Nishido, H., Ogata, K., 1984. K-Ar age determination of Late Pleistocene volcanic rocks. *The Journal of the Geological Society of Japan* 90, 899–909.

Jaffey, A. H., Flynn, K. F., Glendenin, L. E., Bentley, W. C., Essling, A. M., 1971. Precision measurement of half-lives and specific activities of ^{235}U and ^{238}U. *Physical Review Journals* C4, 1889–1906.

Katsui, Y., 1953. Petro-chemical study on the lavas from volcano Rishiri, Hokkaido, Japan. *Journal of the Faculty of Science, Hokkaido University*, Series. 4 8, 245–258.

Katz, R. F., Spiegelman, M., Langmuir, C. H., 2003. A new parameterization of hydrous mantle melting. Geochemistry, Geophysics, Geosystems 4,1073.

Kay, R. W., 1978. Aleutian magnesian andesites: melts from sub-ducted Pacific Ocean crust. *Journal of Volcanology and Geothermal Research* 4, 117–132.

Kay, S. M., Kay, R. W., Citron, G. P., 1982. Tectonic controls on tholeiitic and calc-alkaline magmatism in the Aleutian arc. *Journal of Geophysical Research: Solid Earth* 87, 4051–4072.

Kay, S. M., Kay, R. W., 1985. Aleutian tholeiitic and calc-alkaline magma series I: The mafic phenocrysts. *Contributions to Mineralogy and Petrology* 90, 276–290.

Kawamoto, T., Kanzaki, M., Mibe, K., Matsukage, N., Ono, S., 2012. Separation of supercritical slab-fluids to form aqueous fluid and melt components in subduction zone magmatism. *Proceedings of the National Academy of Sciences of the United States of America* 109, 18695–700.

Kawamoto, T., Mibe, K., Bureau, H., Reguer, S., Mocuta, C., Kubsky, S., Thiaudière, D., Ono, S., Kogiso, T., 2014. Large-ion lithophile elements delivered by saline fluids to the sub-arc mantle. *Earth Planets and Space* 66, 61.

Kelemen, P. B., Hart, S. R., Bernstein, S., 1998. Silica enrichment in the continental upper mantle via melt/rock reaction. *Earth and Planetary Science Letters* 164, 387–406.

Kelemen, P. B., Yogodzinski , G. M., Scholl, D. W., 2003. Along-strike variation in the Aleutian island arc: Genesis of high Mg# andesite and implications for continental crust, in *Inside the Subduction Factory*, Eiler, J. (Ed.), Geophysical Monograph, 138, 223–276, American Geoscience Union, Washington, D. C.

Kelley, K. A., Plank, T., Grove, T. L., Stolper, E. M., Newman, S., Hauri, E., 2006, Mantle melting as a function of water content beneath back-arc basins, *Journal of Geophysical Research* 111, B09208.

Kelley, K., Cottrell, E., 2009. Water and the oxidation state of subduction zone magmas. *Science* 325, 605–607.

Kennedy, G. C., Wasserburg, G. J. Heard, H. C., Newton, R. C., 1962. The upper three-phase region in the system SiO_2–H_2O. *American Journal of Science* 260, 501–521.

Kennett, B. L. N., Furumura, T., 2010. Tears or thinning? Subduction structures in the Pacific plate beneath the Japanese Islands. *Physics on the Earth and Planetary Interiors*180, 52–58.

Kessel, R., Schmidt, M. W., Ulmer, P., Pettke, T., 2005. Trace element signature of subduction-zone fluids, melts and supercritical liquids at 120–180 km depth. *Nature* 437, 724–727.

Kessel, R., Ulmer, P., Pettke, T., Schmidt, M. W., Thompson, A. B., 2005. The water-basalt system at 4 to 6 GPa: Phase relations and second critical endpoint in a K-free eclogite at 700 to 1400 ℃. *Earth and Planetary Science Letters* 237, 873–892.

Kepezhinskas, P., Defant, M. J., Drummond, M. S., 1996. Progressive enrichment of island arc mantle by melt-peridotite interaction inferred from Kamchatka xenoliths. *Geochimica et Cosmochimica Acta* 60, 1217–1229.

Kimura, J.-I., Yoshida T., 2006. Contributions of slab fluid, mantle wedge and crust to the origin of Quaternary lavas in the NE Japan Arc. *Journal of Petrology* 47, 2185–2232.

Kimura, J.-I., Nagahashi, Y., Satoguchi, Y., Chang, Q., 2015. Origins of felsic magmas in Japanese subduction zone: Geochemical characterizations of tephra from caldera-forming eruptions <5 Ma. *Geochemistry, Geophysics, Geosystems* 16, 2147–2174.

Kimura, J.-I., 2017. Modeling chemical geodynamics of subduction zones using the Arc Basalt Simulator version 5. *Geosphere* 13, 992–1025.

Kinzler, R. J., Grove, T. L., Recca, S. I., 1990. An experimental study on the effect of temperature and melt composition on the partitioning of nickel between olivine and silicate melt. *Geochimica et Cosmochimica Acta* 54, 1255–1265.

Kita, S., Okada, T., Hasegawa, A., Nakajima, J., Matsuzawa, T., 2010. Anomalous deepening of a seismic belt in the upper-plane of the double seismic zone in the Pacific slab beneath the Hokkaido corner: Possible evidence for thermal shielding caused by subducted fore-arc crust materials. *Earth and Planetary Science Letters* 290, 415–426.

Kobayashi, T., 1987. Geology of Rishiri Volcano (in Japanese with English abstract). *The Journal of the Geological Society of Japan* 93, 749–760.

Kobayashi, T., 1989. Geology and Petrology of Rishiri Volcano, Hokkaido, Japan. *PhD thesis, Graduate School of Science, Hokkaido University, Sapporo.*

Kondo, R., Tsukamoto, S., Tachibana, H., Miyairi, Y., Yokoyama, Y., 2007. Age of glacial and periglacial landforms in northern Hokkaido, Japan, using OSL dating of fine grain quartz. *Quaternary Geochronology* 2, 260–265.

Kondo, R., Tsukamoto, S., 2009. Age of volcanic fan around the western part of Rishiri volcano, northern Hokkaido, Japan, using OSL dating. *The Quaternary Research* 48, 243–254 (in Japanese with English abstract).

Kondo, R., 2015. Age of flank eruptions of Rishiri Volcano, northern Hokkaido, Japan, using OSL dating. *Sundai Historical Review* 153, 17–36 (in Japanese with English abstract).

Kondo, R., Sato, M., Miyairi, Y., Matsuzaki, H., 2015. AMS14C dating at Giboshi-numa eruptive fissure, Rishiri Island. *Rishiri Research*, 34, 61–66.

Kuno, H., 1966. Lateral variation of basalt magma type across continental margins and island arcs. *Bulletin of Volcanology* 195–222.

Kuritani, T., 1998. Boundary layer crystallization in a basaltic magma chamber: Evidence from Rishiri Volcano, northern Japan. *Journal of Petrology*, 39(9), 1619–1640.

Kuritani, T., 1999. Boundary layer fractionation constrained by differential information from the Kutsugata lava flow, Rishiri Volcano, Japan. *Journal of Geophysical Research: Solid Earth* 104, 401–417.

Kuritani, T., 2001. Replenishment of a mafic magma in a zoned felsic magma chamber beneath Rishiri Volcano, Japan. *Bulletin of Volcanology* 62, 533–548.

Kuritani, T., Nakamura, E., 2002. Precise isotope analysis of nanogram-level Pb for natural rock samples without use of double spikes. *Chemical Geology* 186, 31–43.

Kuritani, T., Nakamura, E., 2003. Highly precise and accurate isotopic analysis of small amounts of Pb using ^{205}Pb–^{204}Pb and ^{207}Pb–^{204}Pb, two double spikes. *Journal of Analytical Atomic Spectrometry* 18, 1464–1470.

Kuritani, T., Kitagawa, H., Nakamura, E., 2005. Assimilation and fractional crystallization controlled by transport process of crustal melt: Implications from an alkali basalt-dacite suite from Rishiri Volcano, Japan. *Journal of Petrology* 46, 1421–1442.

Kuritani, T., Yokoyama, T., Nakamura, E., 2007. Rates of thermal and chemical evolution of magmas in a cooling magma chamber: A chronological and theoretical study on basaltic and andesitic lavas from Rishiri Volcano, Japan. *Journal of Petrology* 48, 1295–1319.

Kuritani, T., Yokoyama, T., Nakamura, E., 2008. Generation of rear-arc magma induced by influx of slab-derived supercritical liquids: Implications from alkali basalt lavas from Rishiri Volcano, Kurile arc. *Journal of Petrology* 49, 1319–1342.

Kuritani, T., Nakagawa, M., 2016. Origin of ultra rear-arc magmatism at Rishiri Volcano, Kuril Arc. *Geochemistry, Geophysics, Geosystems* 17, 4032–4050.

Kuritani, T., Tanaka, M., Yokoyama, T., Nakagawa, M., Matsumoto, A, 2016. Intensive hydration of the wedge mantle at the Kuril arc–NE Japan arc junction: Implications from mafic lavas from Usu Volcano, northern Japan. *Journal of Petrology* 57, 1223–1240.

Kuritani, T., Sakuyama, T., Kamada, N., Yokoyama, T., Nakagawa, M., 2017. Fluid-fluxed melting of mantle versus decompression melting of hydrous mantle plume as the cause of intraplate magmatism over a stagnant slab: implications from Fukue Volcano Group, SW Japan. *Lithos* 282–283, 98–110.

Kushiro, I., 1969. The system forsterite-diopside-silica with and without water at high pressures. *American Journal of Science* 267(A), 269–294.

Lambert, I. B., Wyllie, P. J., 1974. Melting of Tonalite and Crystallization of Andesite Liquid with Excess Water to 30 Kilobars. *The Journal of Geology* 82, 88–97.

Le Roux, L. J., Glendenin, L. E., 1963. Half-life of ^{232}Th in *Proceedings of the National Meeting on Nuclear Energy, Pretoria, South Africa* 83–94.

Le Voyer, M., Rose-Koga, E. F., Shimizu, N., Grove, T. L., Schiano, P., 2010. Two contrasting H_2O-rich components in primary melt inclusions from Mount Shasta. *Journal of Petrology* 51, 1571–1595.

Ma, Q. Zheng, J-P, Xu, Y-G, Griffin, W. L., Zhang, R-S., 2015. Are continental "adakites" derived from thickened or foundered lower crust?. *Earth and Planetary Science Letters* 419, 125–133.

Martin, H., 1986. Effect of steeper Archean geothermal gradient on geochemistry of subduction-zone magmatism. *Geology* 14, 753–756.

Martin, H., Smithies, R. H., Rapp, R., Moyen, J. -F., Champion, D., 2005. An overview of adakite, tonalite-trondhjemite-granodiorite (TTG), and sanukitoid: relationships and some implications for crustal evolution. *Lithos* 79, 1–24.

Matsui, K., Issiki, N., Hata, M., Yamaguchi, S., Yoshii, M., Ono, K., Satoh, H., Sawamura, K., 1967. *Explanatory text of the geological map of Japan, Rishirito*, scale 1:50,000. Hokkaido development agency (in Japanese with English abstract).

Médard, E., Grove, T. L., 2008. The effect of H_2O on the olivine liquidus of basaltic melts: Experiments and thermodynamic models. *Contributions to Mineralogy and Petrology* 155, 417–432.

McKenzie, D., 1984. The generation and composition of partially molten rock. *Journal of Petrology* 25, 713–765

Mibe, K., Kanzaki, M., Kawamoto, T., Matsukage, K. N., Fei, Y., Ono, S., 2004. Determination of the second critical end point in silicate-H_2O systems using high-pressure and high-temperature X-ray radiography. *Geochimica et Cosmochimica Acta* 68, 5189–5195.

Mibe, K., Kanzaki, M., Kawamoto, T., Matsukage, K. N., Fei, Y., Ono, S., 2007. Second critical endpoint in the peridotite-H_2O system. *Journal of Geophysical Research: Solid Earth* 112, B03201.

Mibe, K., Kawamoto, T., Matsukage, N. K., Fei, Y., Ono, S., 2011. Slab melting versus slab dehydration in subduction-zone magmatism. *Proceedings of the National Academy of Sciences of the United States of America 108*, 8177–8182.

Miller, M. S., Kennett, B. L. N., Gorbatov, A., 2006. Morphology of the distorted subducted Pacific slab beneath the Hokkaido corner. *Physics on the Earth and Planetary Interiors* 156, 1–11.

Min, K., Mundil, R., Penne, P. R., Ludwing, R., 2000. A test for systematic errors in ^{40}Ar/^{39}Ar geochronology through comparison with U/Pb analysis of a 1.1-Ga rhyolite. *Geochimica et Cosmochimica Acta* 64, 73–98.

Miura, H., Takaoka, S., 1993. Significance of the radiocarbon age and the identification of the fossil wood under lava flows erupted from Rishiri Volcano, Hokkaido, Japan. *The Quaternary Research* 32, 107–114 (in Japanese with English abstract).

Miura, H., 1995. A proposal for the source vent of the Rishiri-wankonosawa tephra (Ws-Wn), the late Pleistocene marker tephra in northern Hokkaido. *Geographical reports of Tokyo Metropolitan University* 30, 133–145.

Miura, H., 1995. Quaternary geological and geomorphological study on consolidated fine-grained soil occurring in northern Hokkaido. *Ph. D. thesis, Tokyo Metropolitan University* 160 pp.

Miyashiro, A., 1974. Volcanic rock series in island arcs and active continental margins. *American Journal of Science* 274, 321–355.

Miyashiro, A., 1978. Nature of alkalic volcanic rock series, *Contributions to Mineralogy and Petrology* 66, 91–104.

Moriya, I., 1983. *Volcanic Landform of Japan*. The University of Tokyo Press, 135p (in Japanese).

Nagao, L., Ogata, A., Miura, Y. N., Yamaguchi, K., 1996. Ar isotope analysis for K-Ar dating using two modified-VG-5400 mass spectrometers-I: Isotope dilution method. *Journal of Mass Spectrometry Society of Japan* 44, 39–61.

Nakamura, E., Makishima, A., Moriguchi, T., Kobayashi, K., Sakaguchi, C., Yokoyama, T., Tanaka, R., Kuritani, T., Takei, H., 2003. Comprehensive geochemical analyses of small amounts (<100 mg) of extraterrestrial samples for the analytical competition related to the sample return mission MUSES-C. *Institute of Space Astronautical Science Report SP* 16, 49–101.

Nakamura, K., 1964. Volcano-stratigraphic study of Oshima volcano, Izu. *Bulletin of Earthquake Research Institute* 42, 649–782.

Narvaez, D. F., Rose-Koga, E. F., Samaniego, P., Koga, K. T., Hidalgo, S., 2018. Constraining magma sources using primitive olivine-hosted melt inclusions from Puñalica and Sangay volcanoes (Ecuador). *Contributions to Mineralogy and Petrology* 173: 80.

Ni, H., Zhang, L., Xiong, X., Mao, Z., Wang, J., 2017. Supercritical fluids at subduction zones: Evidence, formation condition, and physicochemical properties. *Earth-Science Reviews* 167, 62–71.

Nishiki, K., Takahashi, K. Matsumoto, A., Miyake, Y., 2011. Quaternary volcanism and tectonic history of the Suwa-Yatsugatake Volcanic Province, central Japan. *Journal of Volcanology and Geothermal Research* 203, 158–167.

Niu, X., Zhao, D., Li, J., Ruan, A., 2016. P wave azimuthal and radial anisotropy of the Hokkaido subduction zone. *Journal of Geophysical Research: Solid Earth* 121, 2636– 2660.

Noguchi, T., Shinjo, R., Ito, M., Takada, J., Oomori, T., 2011. Barite geochemistry from hydrothermal chimneys of the Okinawa Trough: Insight into chimney formation and fluid/sediment interaction. *Journal of Mineralogical and Petrological Sciences* 106, 26–35.

Otofuji, Y., Matsuda, T., Nohda, S., 1985. Paleomagnetic evidence for the Miocene counter-clockwise rotation of Northeast Japan -rifting process of the Japan Arc. *Earth and Planetary Science Letters* 75, 265–277.

Paillat, O., Elphick, S. C., Brown, W. L., 1992. Solubility of water in $NaAlSi_3O_8$ melts: a re examination of Ab-H_2O phase relationships and critical behavior at high pressures. *Contribution to Mineralogy and Petrology* 112, 490–500.

Papale, P., Moretti, R., Barbato, D., 2006. The compositional dependence of the saturation surface of $H_2O + CO_2$ fluids in silicate melt. *Chemical Geology* 229, 78–95.

Peacock, S. M., Wang, K., 1999. Seismic consequences of warm versus cool subduction metamorphism: Examples from southwest and northeast Japan. *Science* 286, 937–939.

Peccerillo, A., Taylor, S. R., 1976. Geochemistry of Eocene calc-alkaline volcanic rocks from the Kastamonu Area, northern Turkey. *Contributions to Mineralogy and Petrology* 58, 63– 81.

Petford, N., Atherton, M., 1996. Na-rich partial melts from newly underplated basaltic crust: the Cordillera Blanca Batholith, Peru. *Journal of Petrology* 37, 1491–1521.

Pin, C., Briot, D., Bassin, C., Poitrasson, F., 1994. Concomitant separation of strontium and samarium-neodymium for isotopic analysis in silicate samples, based on specific extraction chromatography. *Analytica Chimica Acta* 298, 209–217.

Pin, C., Zalduegui, J. F. S., 1997. Sequential separation of light rare-earth elements, thorium and uranium by miniaturized extraction chromatography: Application to isotopic analyses of silicate rocks. *Analytica Chimica Acta* 339, 79–89.

Pineda-Velasco, I., Kitagawa, H., Nguyen, T. -T., Kobayashi, K., Nakamura, E., 2019. Production of High-Sr Andesite and Dacite Magmas by Melting of Subducting Oceanic Lithosphere at Propagating Slab Tears. *Journal of Geophysical Research: Solid Earth* 123, 3698– 3728.

Portnyagin, M., Hoernle, K., Plechov, P., Mironov, N., Khubunaya, S., 2007. Constraints on mantle melting and composition and nature of slab components in volcanic arcs from volatiles (H2O, S, Cl, F) and trace elements in melt inclusions from Kamchatka Arc. *Earth and Planetary Science Letters* 255, 53–69.

Prouteau, G., Scaillet, B., 2003. Experimental constraints on the origin of the 1991 Pinatubo dacite. *Journal of Petrology* 44, 2203–2241.

Putirka, K. D., 2008. Thermometers and barometers for volcanic systems. *Reviews in Mineralogy and Geochemistry* 69, 61–120.

Rapp, R. P., Watson, E. B., 1995. Dehydration melting of metabasalt at 8-32 kbar: Implications for continental growth and crust-mantle recycling. Journal of Petrology 36, 891–931.

Reimer, P. J., Bard, E., Bayliss, A., Beck, J. W., Blackwell, P. G., Ramsey, C. B., Buck, C. E., Cheng, H., Edwards, R. L., Friedrich, M., Grootes, P. M., Guilderson, T. P., Haflidason, H., Hajdas, I., Hatté, C., Heaton, T. J., Hoffmann, D. L., Hogg, A. G., Hughen, K. A., Kaiser, K. F., Kromer, B., Manning, S. W., Niu, M., Reimer, R. W., Richards, D. A., Scott, E. M., Southon, J. R., Staff, R. A., Turney, C. S. M., and Plicht, J., 2013. IntCal13 and Marine13 Radiocarbon Age Calibration Curves 0–50,000 Years cal BP. *Radiocarbon* 55, 1869–1887.

Ringwood, A. E., 1974. The petrological evolution of island arc system. *Journal of the Geological Society* 130, 183–204.

Roeder, P. L., Emslie, R. F., 1970. Olivine-liquid equilibrium. *Contributions to Mineralogy and Petrology* 29, 275–289.

Rooney, T. O., Deering, C. D., 2014. Conditions of melt generation beneath the Taupo Volcanic Zone: The influence of heterogeneous mantle inputs on large-volume silicic systems. *Geology* 42, 3–6.

Rudnick, R. L., Gao, S., 2003. Composition of the Continental Crust, in: Rudnick, R. (Eds.), *The Crust*. Treatise on Geochemistry 3, Oxford, Elsevier-Pergamon, pp. 1–64.

Sakuyama, M., 1981. Petrological study of the Myoko and Kurohime volcanoes, Japan: crystallization sequence and evidence for magma mixing. *Journal of Petrology* 22, 553–583.

Sakuyama, M., Nesbitt, R. W., 1986. Geochemistry of the quaternary volcanic rocks of the northeast Japan arc. *Journal of Volcanology and Geothermal Research* 29, 413–450.

Salters, V. J. M., Stracke, A., 2004. Composition of the depleted mantle, *Geochemistry, Geophysics, Geosystems* 5, Q05B07.

Sato, M., Kondo, R., Momohara, A., Nishiuchi, R., Konno, M., Shigeno, K., Nagai, M., Kosugi, K., Endo, K., Irino, T., Study of environmental and vegetational history in Rishiri Island for the wetland-ecosystem conservation and natural history education –Natural history

of Minamihama marsh by borehole cores investigation–. *Report of Pro Natura Foundation*, Japan 21, 101–116 (in Japanese with English abstract).

Schiano, P., Clocchiatti, R., Ottolini, L., Busà, T., 2001. Transition of Mount Etna lavas from a mantle-plume to an island-arc magmatic source. *Nature* 412, 990–904.

Schiavi, F., Kobayashi, K., Nakamura, E., Massimo, T, Vannucci, R., 2012. Trace element and Pb–B–Li isotope systematics of olivine-hosted melt inclusions: insights into source metasomatism beneath Stromboli (southern Italy). *Contributions to Mineralogy and Petrology* 163, 1011–1031.

Shen, A. H., Keppler, H., 1997. Direct observation of complete miscibility in the albite-H_2O system. *Nature* 385, 710–712.

Sisson, T. W., Grove, T. L., 1993. Experimental investigations of the role of H_2O in calc-alkaline differentiation and subduction zone magmatism. *Contributions to Mineralogy and Petrology* 113, 143–166.

Smith, P. M., Asimow, P. D., 2005. Adiabat_1ph: A new public front-end to the MELTS, pMELTS, and pHMELTS models. *Geochemistry, Geophysics, Geosystems* 6, Q02004.

Stalder, R., Ulmer, P., Thompson, A. B., Günther, D., 2000. Experimental approach to constrain second critical end points in fluid/silicate system: Near-solidus fluids and melts in the system albite-H_2O. *Americal Mineralogist* 85, 68-77.

Straub, S. M., LaGatta, A. B. Martin-Del Pozzo, A. L., Langmuir, C. H., 2008. Evidence from high-Ni olivines for a hybridized peridotite/pyroxenite source for orogenic andesites from the central Mexican volcanic belt. *Geochemistry, Geophysics, Geosystems* 9, Q03007.

Straub, S. M., Gomez-Tuena, A., Stuart, F. M., Zellmer, G. F., Esinasa-Perena, R., Cai, Y., Iizuka, Y., 2011. Formation of hybrid arc andesites beneath thick continental crust. *Earth and Planetary Science Letters* 303, 337–347.

Streck, M. J., Leeman, W. P., Chesley, J. T., 2007. High-magnesian andesite from Mount Shasta; a product of magma mixing and contamination, not a primitive mantle melt. *Geology* 35, 351–354.

Stuiver, M., Polach, H. A., 1977. Discussion: Reporting of ^{14}C data. Radiocarbon 19, 355–363.

Sun, S.-S., McDonough, M. F., 1989. Chemical and isotopic systematics of oceanic basalts: Implications for mantle composition and processes, in: Saunders, A. D., Norry, M. J. (Eds.), *Magmatism in the Ocean Basins*. Geological Society of London, Special Publications, 42, pp. 313–345.

Syracuse, E. M., van Keken P. E., Abers, G. A., 2010. The global range of subduction zone thermal models. *Physics of the Earth and Planetary Interiors* 183, 73–90.

Tait, S. R., Jaupart, C., 1996. The production of chemically stratified and adcumulate plutonic igneous rocks. *Mineralogical Magazine* 60, 99–114.

Takahashi, E., 1986. Genesis of calc-alkali andesite magma in a hydrous mantle-crust boundary: petrology of lherzolite xenoliths from the Ichinomegata Crater, Oga Peninsula, Northeast Japan; Part II. *Journal of Volcanology and Geothermal Research* 29, 355–395.

Takahashi, E., 1986. Origin of basaltic magmas – Implication from peridotite melting experiments and an olivine fractionation model-. *Bulletin of Volcanology Society of Japan* 2, S17–S40 (in Japanese with English abstract).

Tamura, Y., Ishizuka, O., Stern, R. J., Nichols, A. R. L. Kawabata, H., Hirahara, Y., Chang, Q., Miyazaki, T., Kimura, J-I., Embley, R. W., Tatsumi, Y., 2014. Mission immiscible: Distinct subduction component generate two primary magmas at Pagan Volcano, Mariana arc. *Journal of Petrology* 55, 63–101.

Tamura, Y. Sato, T., Fujiwara, T., Kodaira, S., Alexander, N., 2016. Advent of continents: A new hypothesis. *Scientific Reports* 6, 33517.

Taniuchi, H., Kuritani, T., Nakagawa, M., 2020a. Generation of calc-alkaline andesite magma through crustal melting induced by emplacement of mantle-derived water-rich primary magma: Evidence from Rishiri Volcano, southern Kuril Arc. *Lithos* 354–355, 105362.

Taniuchi, H., Kuritani, T., Yokoyama, T., Nakamura, E., Nakagawa, M., 2020b. A new concept for the genesis of felsic magma: the separation of slab-derived supercritical liquid. *Scientific Reports* 10, 8698.

Tatsumi, Y., 1982. Origin of high-magnesian andesites in the Setouchi Volcanic Belt, Southwest Japan, 2. Melting phase-relations at high pressures. *Earth and Planetary Science Letters* 60, 305–317.

Tatsumi, Y., 1983. High magnesian andesites in the Setouchi volcanic belt, southwest Japan and their possible relation to the evolutionary history of the Shikoku inter-arc basin. In *Geodynamics of the Western Pacific-Indonesian Regions*, Hilde, T. W. C., Uyeda, S. (eds.), American Geophysical Union, Geodynamics Series, 11, 331–341 (Washington, DC).

Tatsumi, Y., Sakuyama, M., Fukuyama, H., Kushiro, I., 1983. Generation of arc basalt magmas and thermal structure of the mantle wedge in subduction zones. *Journal of Geophysical Research* 88, 5815–5825.

Taylor, S. R., White, A. J. R., 1965 Geochemistry of andesites and the growth of continents. *Nature* 208, 271–273.

Taylor, S. R., 1976. Melting relation in the system MgO-Al$_2$O$_3$-SiO$_2$ at 15 Kb. *Geological Society of America Bulletin* 84, 1335–1348

Taylor, R. N., Nesbitt, R. W., 1998. Isotopic characteristics of subduction fluids in an intra-oceanic setting, Izu-Bonin Arc, Japan. *Earth and Planetary Science Letters* 164, 79–98.

Tomiya, A., 1991. Volume of mantle diapir compatible with life span of a typical island-arc volcano (in Japanese with English abstract). *Bulletin of the Volcanological Society of Japan* 36, 211–221.

Tsukui, M., Nishido, H., Nagao, K., 1985. K-Ar ages of the Hiruzen Volcano Group and the Daisen Volcano. *Journal of Geological Society of Japan* 91, 279–288.

Ueki, T., Kondo, R., 2008. Eruption age of the Kutsugata lava flow, Rishiri Volcano, off northern Hokkaido, Japan, based on AMS ^{14}C dating of charred fossil wood immediately beneath the lava flow. *The Quaternary Research* 47, 349–353 (in Japanese with English abstract).

Ueki, T., Kondo, R., 2010. K-Ar ages of Middle and Late Pleistocene lavas from the Rishiri Volcano, off northern Hokkaido, Japan. *Journal of Geological Society of Japan* 116, 686–689 (in Japanese with English abstract).

Wager, L. R., Deer, W. A., 1939. *Geological investigations in East Greenland, Part. III. Meddelelser om Grønland* 105.

Waters, L. E., Lange, R. A., 2015. An updated calibration of the plagioclase-liquid hygrometer-thermometer applicable to basalts through rhyolites. *American Mineralogist* 100, 2171–2184.

Yamamoto, T., Kudo, T., Ishizuka, O., 2018. Temporal variations in volumetric magma eruption rates of Quaternary volcanoes in Japan. *Earth, Planets and Space* 70, 65.

Yoder, H. S., Tilley, C. E., 1962. Origin of Basalt Magmas: An Experimental Study of Natural and Synthetic Rock Systems. *Journal of Petrology* 3, 342–532.

Yokoyama, T., Makishima, A., Nakamura, E., 1999. Evaluation of the coprecipitation of incompatible trace elements with fluoride during silicate rock dissolution by acid digestion. *Chemical Geology* 157, 175–187.

Yokoyama, T., Kobayashi, K., Kuritani, T., Nakamura, E., 2003. Mantle metasomatism and rapid ascent of slab-components beneath island arc: Evidence from 238U-230Th-226Ra disequilibria of Miyakejima volcano, Izu arc, Japan. *Journal of Geophysical Research: Solid Earth* 108, 2329.

Yokoyama, T., Nagai, Y., Hinohara, Y., Mori, T., 2016. Investigating the influence of non-spectral matrix effects in the determination of twenty-two trace elements in rock samples by ICP–QMS. *Geostandards and Geoanalytical Research* 41, 221–242.

Zindler, A., Hart, S., 1986. Chemical geodynamics. *Annual Review of Earth and Planetary Sciences* 14, 493–571.

Zou, H., 2007. *Quantitative Geochemistry*, 287pp, Imperial collage Press, London, U. K.